UNIVERSITY OF CALIFORNIA,
IRVINE

An Analysis of the Behavior and Intensity of Extreme Atmospheric Moisture Transport Events over the North Pacific Basin

DISSERTATION

submitted in partial satisfaction of the requirements
for the degree of

DOCTOR OF PHILOSOPHY

in Earth System Science

by

Ashley Elizabeth Payne

Dissertation Committee:
Professor Gudrun Magnusdottir, Chair
Professor Amir AghaKouchak
Professor Jin-Yi Yu

2016

DEDICATION

"The most difficult thing is the decision to act. The rest is merely tenacity"
- *Amelia Earhart* -

To Josh and my family for their support and infinite patience.

TABLE OF CONTENTS

LIST OF FIGURES

LIST OF TABLES

LIST OF ACRONYMS

A summary of acronyms used throughout the dissertation.

Acronym	**Full name**
AR	atmospheric river
AO	Arctic Oscillation
CMIP5	Coupled Model Inter-comparison Project, Phase 5
ENSO	El Niño – Southern Oscillation
EOF	Empirical Orthogonal Function
ITCZ	Inter-tropical Convergence Zone
IWV	integrated water vapor
MERRA	Modern Era Retrospective-Analysis for Research and Applications
MEI	Multivariate ENSO Index
MIMIC-TPW	Morphed Integrated Microwave Imagery at CIMSS - Total Precipitable Water
MF	the magnitude of integrated moisture flux
MJO	Madden-Julian Oscillation
NOAA	National Oceanic and Atmospheric Administration
PE	'Pineapple Express'
PDF	probability density function
PDO	Pacific Decadal Oscillation
PNA	Pacific/North American teleconnection pattern
PW	integrated precipitable water
PV	potential vorticity
PVU	Potential Vorticity Unit
RCP	Representative Concentration Pathway
RMM	Real-time Multivariate MJO
RW	Rossby wave
RWB	Rossby wave breaking
SLP	sea level pressure
TME	Tropical Moisture Exports
TPW	total column precipitable water
UTC	Coordinated Universal Time
WCB	Warm Conveyor Belt
WRF	Weather Research and Forecasting model

ACKNOWLEDGMENTS

Foremost, I would like to thank my advisor, Professor Gudrun Magusdottir, for her guidance over the years. While she was always available to offer support, she gave me the freedom to pursue my own research interests. She has been an incredible mentor and has given me an excellent start as an atmospheric scientist. I would also like thank my committee members, Professor Jin-Yi Yu and Professor Amir AghaKouchak, and members of my advancement committee, Professor Padhraic Smyth and Professor Isabella Velicogna, for their guidance and input on my research project and their willingness to write last minute recommendation letters.

I would like to thank Professor Jay Banner and Professor Dan Breecker at the University of Texas for first introducing me to the world of academia as an undergraduate and to Professor Kerry Cook for her advice and mentorship in finding a program in the atmospheric sciences. I would also like to thank the Geophysical Fluid Dynamics Program, and especially Professor Malte Jansen and Professor Tim Cronin, for being excellent mentors and giving me the opportunity to work on an interesting project outside of my field.

I would like to acknowledge the incredible support of both past and current members of the Magnusdottir research group throughout the years. I thank Dr. Joss Matthewman for his help in getting me started on my research after my first year, Dr. Yannick Peings for his support and input when when I was first learning how to use CDO and batch scripts, Dr. Wenchang Yang for his always cheerful and helpful personality and Dr. Graham Simpkins for our wonderful conversations and input on the art of making a scientific figure. I also thank my fellow graduate students in the group, Dr. Yi-Hui Wang and Dr. Colene Haffke, for their friendship over the years we shared an office, and Zack Labe, for his patience over the last year as I finished my graduate work.

Most of all, I would like to thank my first-year cohort (Dr. Xin Li, Dr. Gergana Mouteva, Dr. Tyler Sutterley, Dr. Hongying Yang, Dr. Yuhao Zhu and (soon to be Dr.) Mackenzie Grieman) for their constant support throughout the years. We arrived at the University of California Irvine in September 2010 with completely different backgrounds and throughout the years have learned so much from each other. I also thank all of my friends in the department for making graduate school a fun and unforgettable experience. I will miss you all!

Funding for this research was provided partially by a National Science Foundation Graduate Research Fellowship (DGE-1321846). Travel to AMS's 20th Conference on Atmospheric and Oceanic Fluid Dynamics and to AGU's Annual Fall Meeting 2015 was supported by a Faculty Endowed Fellowship from the School of Physical Sciences. I would like to thank the American Meteorological Society and the American Geophysical Union for their permission to include work published in Journal of Climate and Journal of Geophysical Research: Atmospheres in Chapters 3 and 5, respectively.

CURRICULUM VITAE

Ashley Elizabeth Payne

Research Interests

Climate variability and change, dynamical interactions behind extreme precipitation and weather events, climate system modeling, science communication

Education

Ph.D. Earth System Science, *March 2016*
The University of California, Irvine (09/12 - 03/16)

- Advisor: Gudrun Magnusdottir
- Thesis: An Analysis of the Behavior and Intensity of Extreme Atmospheric Moisture Transport Events over the North Pacific Basin

M.Sc. Earth System Science, *September 2012*
The University of California, Irvine (09/10 - 09/12)

B.Sc. Geological Sciences, *May 2010*
The University of Texas, Austin (08/05 - 05/10)

- Advisor: Jay Banner
- Thesis: Carbon Isotope Analysis of the Sources and Mechanisms of CO_2 Input and Removal from Central Texas Cave Systems

Publications

Payne, A. E., M. F. Jansen, and T. W. Cronin (2015), Conceptual model analysis of the influence of temperature feedbacks on polar amplification, *Geophysical Research Letters*, **42**, 95619570, doi: 10.1002/2015GL065889.

Payne, A. E. and G. Magnusdottir (2015), An evaluation of atmospheric rivers over the North Pacific in CMIP5 and their response to warming under RCP 8.5, *Journal of Geophysical Research Atmospheres*, **120**, 11,173 - 11,190, doi: 10.1002/2015JD023586.

Payne, A. E. and G. Magnusdottir (2014), Dynamics of landfalling atmospheric rivers over the North Pacific in thirty years of MERRA reanalysis. *Journal of Climate*, **27**(18), 7133 - 7150, doi: 10.1175/JCLI-D-14-00034.1.

Breecker, D. O., **A. E. Payne**, J. Quade, J. L. Banner, C. E. Ball, K. W. Meyer, and B. D. Cowan (2012), The sources and sinks of CO_2 in caves under mixed woodland and grassland vegetation. *Geochimica et Cosmochimica Acta*, **96**, 230 - 246, doi: 10.1016/j.gca.2012.08.023.

Non-refereed Publications

Payne, A.E. (2014), Conceptual model analysis of the influence of longwave temperature feedbacks on polar amplification. Woods Hole Oceanographic Institute, Geophysical Fluid Dynamics Program, Proceedings Volume 2014.

Quinn, A.E. (2010), Carbon isotope analysis of the sources and mechanisms of CO_2 input and removal from Central Texas cave systems. Senior honors thesis, Jackson School of Geosciences, University of Texas at Austin.

Poster Presentations

Payne, A. E. and G. Magnusdottir (2015), A dynamical analysis of present and future atmospheric river behavior over the North Pacific in MERRA reanalysis and CMIP5. *An Afternoon of Data Science: A Data Science Initiative Year-End Event*, University of California Irvine Data Science Initiative, Irvine, CA (29 May 2015).

Payne, A. E. and G. Magnsdottir (2014), A dynamical analysis of present and future atmospheric river behavior over the North Pacific in MERRA reanalysis and CMIP5

RCP 8.5 Projections. *2014 Fall Meeting*, American Geophysical Union, San Francisco, CA.

Payne, A. E. and G. Magnsdottir (2013), Atmospheric river formation and behavior over the North Pacific Basin. *19th Conference on Atmospheric and Oceanic Fluid Dynamics*, American Meteorological Society, Newport, RI.

Quinn, A. E., D. O. Breecker, J. L. Banner, and B. D. Cowan (2009), Investigating cave ventilation in Central Texas using seasonal variations in the $\delta^{13}C$ value and concentration of cave-air CO_2. *2009 Annual Meeting*, Geological Society of America, Portland, OR.

Oral Presentations

Payne, A. E. and G. Magnsdottir (2015), An analysis of the dynamical coupling in the development of persistent landfalling atmospheric rivers over the eastern North Pacific. *2015 Fall Meeting*, American Geophysical Union, San Francisco, CA.

Payne, A. E. and E. Swiedler (2015), Student Engagement with the University of California Carbon Neutrality Initiative, *California Higher Education Sustainability Conf.*, San Francisco State University, San Francisco (20 July 2015).

Payne, A. E. and G. Magnusdottir (2015), A dynamical analysis of atmospheric river behavior in two different climates. *20th Conference on Atmospheric and Oceanic Fluid Dynamics*, American Meteorological Society, Minneapolis, MI (19 June 2015).

Payne, A. E. (2014), The role of the lapse rate feedback in Arctic amplification, *Fellowship presentation*, Woods Hole Oceanographic Institute Geophysical Fluid Dynamics Program, Woods Hole, MA (19 August 2014).

Honors, Scholarships, & Fellowships

- University of Michigan's President's Postdoctoral Fellowship (2016)
- Faculty Endowed Fellowship, School of Physical Sciences, University of California Irvine (2015)
- Woods Hole Oceanographic Institution (WHOI) Geophysical Fluid Dynamics Program Fellowship (2014)
- Outstanding Contributions to the Department, Department of Earth System Science, University of California Irvine (2014)
- National Science Foundation Graduate Research Fellowship (2011)
- Highest honors, University of Texas - *top 4% university-wide* (May 2010)
- Valedictorian, Departmental honors, Jackson School of Geosciences, University of Texas (May 2010)
- Phi Kappa Phi, University of Texas chapter scholarship (Spring 2010)
- East Texas Geological Society Scholarship (2009, 2010)
- Endowed Presidential Scholarship, University of Texas (2007, 2008, 2009, 2010)
- Valedictorian Scholarship, State of Texas (2005)

Leadership Experience

- Graduate student representative to the University of California Sustainability Steering Committee (2014 - 2015)
- Graduate student representative to the Global Climate Leadership Council for the University of California system (2014 - 2015)
- Graduate student representative to the Department of Earth System Science, University of California Irvine (2013 - 2014)

ABSTRACT OF THE DISSERTATION

An Analysis of the Behavior and Intensity of Extreme Atmospheric Moisture Transport Events over the North Pacific Basin

By

Ashley Elizabeth Payne

Doctor of Philosophy in Earth System Science

University of California, Irvine, 2016

Professor Gudrun Magnusdottir, Chair

Atmospheric rivers (ARs) are filamentary features that play a leading role in the poleward transport of atmospheric moisture and in the global redistribution of heat from the tropics. When they cross over land (so-called landfall), they are a major source of wintertime precipitation, particularly over the western coastline of North America. The extreme precipitation and flooding that sometimes accompany landfalling ARs can have severe socio-economic consequences. Despite advances in observational networks on land, the large-scale mechanisms influencing AR behavior and landfalling intensity are poorly understood. This dissertation aims to better characterize their present-day behavior and projected response to climate change over the North Pacific basin so as to improve forecasts of their impact at landfall.

Composites of dynamical fields using thirty years of the Modern-Era Retrospective Analysis for Research and Applications (MERRA) reanalysis are made following the eastward progression of ARs. A close relationship exists between the extratropical upper tropospheric dynamics, particularly anticyclonic Rossby wave breaking, and lower tropospheric moisture transport. Comparison between the strongest and the weakest ARs show consistent differences in both the intensity of moisture transport and the scale and rate of development of anticyclonic Rossby wave breaking. The strong relationship of landfalling ARs to anticyclonic Rossby wave breaking persists in a case study analysis of long-duration landfalling

events.

Landfalling ARs are evaluated in historical (1980 - 2004) simulations from 28 models participating in fifth phase of the Coupled Model Intercomparison Project (CMIP5) and compared to the MERRA and ERA-Interim reanalyses. Few models correctly resolve the frequency distribution, interannual variability in number and amplitude of moisture flux, and median landfalling latitude. The response of a subset of high performing models to projected warming is investigated using Representative Concentration Pathway (RCP) 8.5 (2070 - 2099) projections. Selected models show a broadening of the frequency distribution, with the largest increase in frequency occurring equatorward of peak historical frequency. The equatorward increase in peak historical frequency is co-located with increases in the 850- and 250-hPa zonal winds. The moisture flux response to warming is mostly thermodynamic, but equatorward of its peak distribution, it is dominated by a dynamic response.

Chapter 1

Introduction

Cool-season extremes in precipitation along the western coastline of North America rival those experienced along the Gulf and Atlantic coasts during hurricane season (*Ralph and Dettinger*, 2012). Precipitation in this region is notable for its large intra-seasonal and inter-annual variability which make effective water management on seasonal and longer timescales challenging (*Mitchell and Blier*, 1997; *Dettinger et al.*, 2011). To add to this, precipitation extremes are expected to increase under climate change scenarios (*Berg and Hall*, 2015; *Williams et al.*, 2015; *O'Gorman*, 2015), and evidence exists to suggest changes are already seen at the regional and local scale (*Russo et al.*, 2013). Therefore, progress on our understanding of precipitation variability over this agriculturally-significant region is of essential importance.

Features known as atmospheric rivers (ARs) play a vital role in the regional hydrological cycle of the West Coast, contributing a large portion of the water resources to the region. ARs are filamentary features with high water vapor transport in the lower troposphere (Fig. 1.1). Their formation in the northern Pacific basin is of particular interest due to their well-documented effects on land. ARs have been connected to heavy precipitation (*Dettinger*, 2004; *Ralph et al.*, 2011; *Reeves et al.*, 2008; *Neiman et al.*, 2008a,b, 2011; *Dettinger*, 2011; *Ralph and Dettinger*, 2012), flooding (*Dettinger*, 2004; *Ralph et al.*, 2003, 2006, 2011; *Dettinger*, 2011; *Neiman et al.*, 2011) and snow pack variability (*Neiman et al.*, 2008b; *Guan et al.*, 2012) when they cross over land (so called landfall). Their landfall is important to water resources, where they have been shown to contribute between 30% and 50% of wet season precipitation in the region (*Guan et al.*, 2010; *Dettinger et al.*, 2011). Up to three

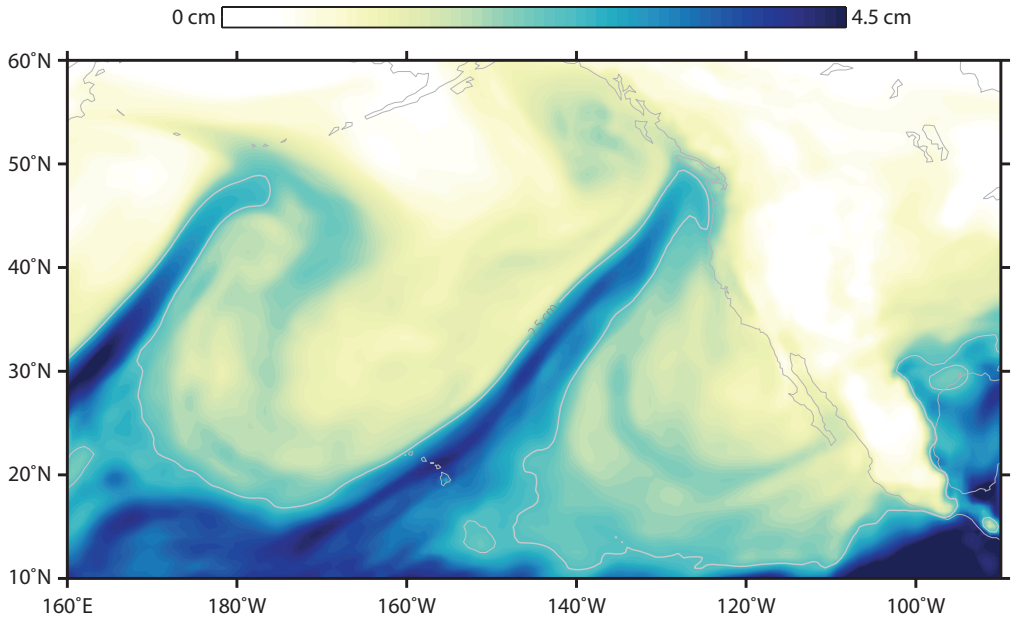

Figure 1.1: An example of a characteristic atmospheric river making landfall along the Pacific Northwest (10:00 UTC 26 March 2005), illustrated as total precipitable water (shading) above 2.5 cm (grey contour) in MERRA reanalysis.

quarters of persistent droughts along the West Coast have been ended by a landfalling AR storm (*Dettinger*, 2013). Although they operate on rather short timescales, depending on their intensity and synoptic characteristics upon landfall, a relatively small number of these storms can be the difference between dry and wet years (*Dettinger et al.*, 2011; *Dettinger*, 2013).

Despite well documented hydrological impacts and meteorological characteristics of landfalling ARs, the large-scale flow influencing ARs prior to landfall is still an area of active research and has received much attention recently (*Ralph et al.*, 2011; *Guan et al.*, 2010, 2012, 2013; *Lavers et al.*, 2012). In animations and in snapshots of moisture transport over the world's ocean basins, the nearly constant presence of ARs in both hemispheres is striking and this was commented on in early studies (e.g. *Newell et al.*, 1992; *Zhu and Newell*, 1998). Those ARs that intersect the West Coast and make landfall vary in moisture source region, trajectory and intensity (*Neiman et al.*, 2008a). Knowledge of modulating factors at subseasonal timescales is needed to address current challenges in AR forecasting (*Ralph et al.*,

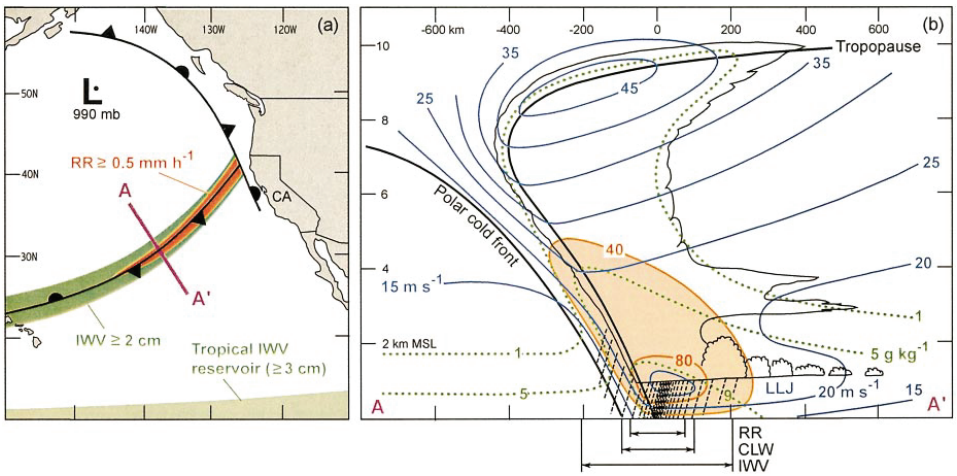

Figure 1.2: (a) Schematic of an AR approaching the West Coast of North America. (b) Along the cross-section in (a), the vertical structure of alongfront moisture flux (shading, units of $\times$ 10^5 kg s^{-1}) and wind speed (dark blue contours, units of m s^{-1}). Below (b), the label IWV indicates the width scale of the 75% cumulative fraction of the perturbation field. Figure is from *Ralph et al.* (2004).

2010; *Wick et al.*, 2013a; *Nayak et al.*, 2014) and projections of their distribution, intensity and frequency with future climate change (*Pierce et al.*, 2013).

The following sections in this chapter provide background on the state of research on ARs. This chapter is concluded with a summary of the scope and organization of the dissertation.

1.1 Synoptic overview

ARs develop on synoptic timescales, generally in association with low-level moisture convergence within extratropical cyclones. Observational work in *Ralph et al.* (2004) and *Ralph et al.* (2005) investigated the vertical structure of landfalling ARs along the West Coast. They found that, for the seasons investigated, landfalling ARs were characterized by high concentrations of water vapor ($\geq$ 2 cm) and wind speeds ($\geq$ 12.5 m s^{-1}) below approximately 850 hPa. The tight gradient in lower level moisture and winds can be seen in a schematic of a cross-sectional view through a representative landfalling AR (Fig. 1.2; *Ralph et al.*, 2004). The high moisture within ARs is concentrated into narrow ($\leq$ 500 km, Fig. 1.2b width scale

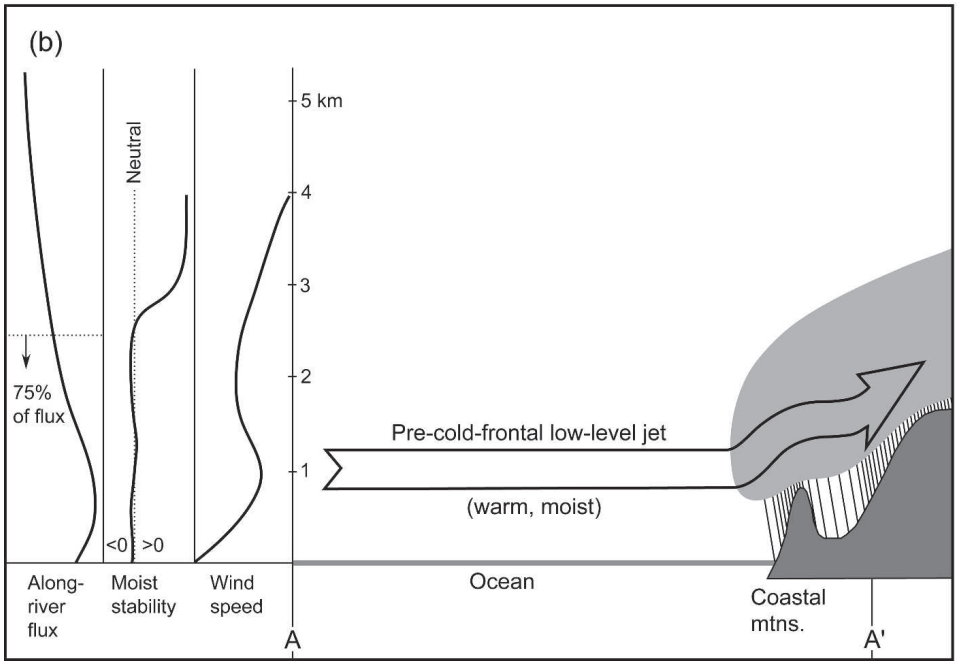

Figure 1.3: Schematic of the low-level jet structure as it makes landfall. The vertical characteristics of the jet are on the left showing the concentration of water vapor in the lowest 2 km in combination with highest wind speeds. Figure is from *Ralph et al.* (2005).

below figure) and long ($\geq$ 2000 km) filamentary structures (*Newell et al.*, 1992; *Zhu and Newell*, 1998; *Ralph et al.*, 2004, 2005). Figure 1.2a shows this characteristic geometry as concentrated integrated moisture in green shading.

Landfalling ARs have a significant effect on precipitation upon landfall. The combination of high moisture and large wind speeds with neutral stability to moist ascent can result in heavy precipitation when ARs interact with the considerably rougher topography of coastal mountains (Fig. 1.3; *Ralph et al.*, 2005). In a modeling study of the orographic effects on a landfalling AR, *Smith et al.* (2010) found that moisture flux was diminished up to 40% through interactions with topography. However, recent work has shown that ARs may have precipitation impacts in-land as well. Work in *Rutz and Steenburgh* (2012) showed that ARs making landfall along the coastline of Baja California play an important role in precipitation in the semi-arid Southwest United States. Additional work in *Neiman et al.* (2013) and *Rivera et al.* (2014) provide synoptic and climatological insights into in-land pen-

etrating ARs affecting the Arizona region. In an overview of in-land penetrating ARs over western North America, *Rutz et al.* (2014) found that these ARs are characterized by larger moisture transport and southwesterly flow.

1.2 What does an 'atmospheric river' describe?

For a number of years, the expression 'atmospheric river' has been used to broadly define distinguishable thin bands of high moisture content in the lower troposphere (*Newell et al.*, 1992; *Newell and Zhu*, 1994). *Newell et al.* (1992) found that approximately four or five ARs are in existence at any one time over major basins globally. These structures have been shown to be responsible for as much as 90% of transport in less than 10% of the Earth's circumference at the mid-latitudes, at a flow rate greater than that in the Amazon or Mississippi Rivers (*Zhu and Newell*, 1998; *Ralph and Dettinger*, 2011). They seemingly connect the high concentrations of water vapor in the tropics to the extratropics in the lower troposphere (*Newell et al.*, 1992; *Zhu and Newell*, 1998; *Dettinger*, 2004; *Ralph et al.*, 2005). However, the arbitrariness of this term has lead to some disagreement about its use (e.g. *Knippertz and Wernli*, 2010; *Sodemann and Stohl*, 2013). In this section, I outline the relationship of ARs to two features known to be associated in their own right to the large-scale transport of atmospheric moisture and clarify the subject of this dissertation.

AR development has often been tied to classical extratropical cyclone development (e.g. *Zhu and Newell*, 1998). *Ralph et al.* (2004) showed that ARs preferentially form within convergence zones associated with eastward propagating extratropical cyclones. Extratropical cyclones have a characteristic 'comma' shape, made up of a leading warm front along the foremost boundary and a trailing cold front (*Carlson*, 1991). Within this cyclone model, the warm conveyor belt (WCB) transports moisture northwards ahead of the trailing cold front (*Carlson*, 1991). WCBs are characterized by the transport poleward and vertical ascent of high latent and sensible heat and the generation of precipitation (*Browning*, 1990; *Eckhardt et al.*, 2004; *Madonna et al.*, 2014; *Pfahl et al.*, 2014). Despite the close relationship between ARs and WCBs, *Newell et al.* (1992) found that some ARs are found far from

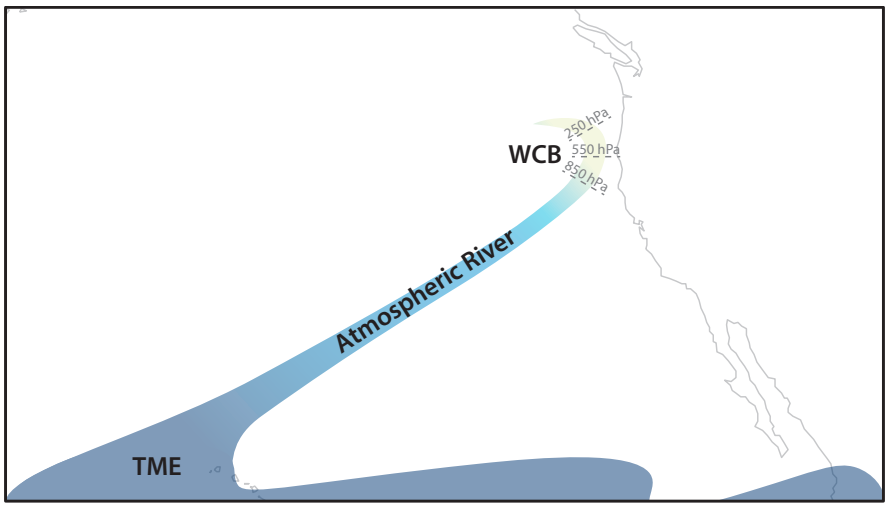

Figure 1.4: Schematic showing an example of the relationship between TMEs, ARs and WCBs. Shading shows the pressure level below which moisture transport is occurring and vertical changes are indicated by text. Figure is adapted from an example in *Dettinger et al.* (2015).

extratropical cyclones, sometimes as far as several thousand kilometers from the center. Furthermore, work in *Sodemann and Stohl* (2013) found that the development of an AR is not necessarily uniquely associated with a single cyclone, but rather may span the lifetimes of multiple cyclones.

As has been pointed out by previous researchers (e.g. *Bao et al.*, 2006; *Newman et al.*, 2012), ARs do not represent trajectories of moisture as their name might suggest, but are rather constantly evolving pathways for moisture transport, recycling moisture between the atmosphere and the underlying ocean as they move over basins. However, work in *Bao et al.* (2006) showed that the moisture within some particularly intense ARs may be tropical in origin. A well-known type of AR with links to the tropics are 'Pineapple Express' events, which are characterized by particularly strong fluxes of water vapor from the sub-tropics near Hawaii and heavy precipitation along the West Coast (*Higgins et al.*, 2000). Work in *Knippertz and Wernli* (2010) and in *Knippertz et al.* (2013) distinguished these features transporting tropical moisture as tropical moisture exports (TMEs), which form only a subset of all ARs (*Dettinger et al.*, 2011; *Ryoo et al.*, 2015).

For the purposes of this research, we follow the guidelines outlined in *Dettinger et al.* (2015). The term 'atmospheric river' describes the intense poleward flux of moisture in the lower troposphere (below 850 hPa) within thin, filamentary structures. These ARs may directly 'tap' tropical moisture sources through their interaction with TMEs, but moisture is not necessarily tropically-sourced. They are distinguished from WCBs by horizontal, rather than ascending, moisture flux. Following the example in *Dettinger et al.* (2015), Fig. 1.4 shows a schematic representation of the interactive relationship between ARs, TMEs and WCBs.

1.3 Scope and organization of dissertation

This study takes a new approach to an investigation of landfalling ARs by exploring changes in their behavior and development within a large-scale context. The association of ARs with extratropical cyclones and with the development of low-level jets motivate an investigation of their relationship with upper-atmospheric flow. An understanding of the relationship of upper-level features such as Rossby waves with ARs may increase our understanding of their behavior and intensity at landfall and potentially aid in their forecast. Specifically, the goals of this study are to investigate the climatological characteristics of atmospheric rivers and their connection to large-scale dynamics and to assess the nature of their response to climate change. The results of this dissertation have implications for both the present day forecast of the intensity and behavior of landfalling AR events and for our understanding of the vulnerabilities of the western coastline of North America to changes in precipitation and extremes in a changing climate.

In Chapter 2, I summarize two main approaches used in the literature for the identification of ARs and conclude with a discussion of the method used in this dissertation.

In Chapter 3, I present a climatological overview of North Pacific atmospheric rivers and investigate their behavior within the context of large-scale atmospheric dynamics. While atmospheric rivers are well-observed along the coastline and their contribution to extreme precipitation is known, few focus on their characteristics prior to landfall and the mechanisms

modifying their behavior. This research is one of the first to take this approach. For this undertaking, a method to identify landfalling atmospheric river conditions was developed based on the magnitude of integrated moisture transport along the coastline in Modern-Era Retrospective Analysis for Research and Applications (MERRA) reanalysis. Characteristic upper- and lower-level features were assessed using composite analysis. In order to investigate the connection between Rossby wave breaking and the intensity of moisture transport within atmospheric rivers, the development of a subset of intense events were investigated. I address the following questions:

- How do large-scale teleconnection patterns, such as the El Niño - Southern Oscillation (ENSO) and the Madden-Julian Oscillation (MJO), modify the characteristics of landfalling events?
- Is knowledge of upper-level dynamical fields useful in an investigation of atmospheric river behavior?
- What is the relationship between atmospheric river intensity of anticyclonic and cyclonic Rossby wave breaking?

This work is published in *Journal of Climate* as:

> **Payne, A. E.** and G. Magnusdottir (2014), Dynamics of landfalling atmospheric rivers over the North Pacific in thirty years of MERRA reanalysis. *Journal of Climate*, **27**(18), 7133 - 7150, doi: 10.1175/JCLI-D-14-00034.1.

Building on the results of Chapter 3, in Chapter 4, long-duration landfalling AR events are isolated. The characteristics of these persistent events are then compared to the climatology of all AR events. In order to investigate whether the large scale characteristics of persistent events are unique to their development, a K-means weather regime analysis is used to investigate moisture transport anomalies associated with three different regimes. I address the following questions:

- Are long-duration ARs different from the climatology of all ARs?
- Are persistent circulation anomalies associated with long-duration ARs unique?

This work is in preparation for submission to *Monthly Weather Review* as:

> **Payne, A.E.** and G. Magnusdottir (2016), Development of persistent landfalling atmospheric rivers over the eastern North Pacific, to be submitted to *Monthly Weather Review*.

Finally, in Chapter 5, we address the question of how will atmospheric river behavior change within a warming climate system. I evaluate the representation of landfalling ARs in 28 different models, participating in the fifth phase of the Coupled Model Intercomparison Project (CMIP5), by comparing their historical simulations to two different reanalysis datasets (MERRA and ERA-Interim). I then investigate the response of landfalling ARs to warming using Representative Concentration Pathway (RCP) 8.5 projections in a subset of high-performing models. This work is the first to comprehensively evaluate the performance of CMIP5 in their representation of atmospheric rivers over the North Pacific. I address the following questions:

- Are CMIP5 models able to capture the spatial and temporal characteristics of North Pacific atmospheric rivers?
- What is the response of atmospheric river intensity, frequency and location to climate change?
- If there is a change in atmospheric rivers with warming, what can it be attributed to?

This work is published in *Journal of Geophysical Research: Atmospheres* as:

> **Payne, A. E.** and G. Magnusdottir (2015), An evaluation of atmospheric rivers over the North Pacific in CMIP5 and their response to warming under RCP 8.5. *Journal of Geophysical Research Atmospheres*, **120**, 11,173 - 11,190, doi: 10.1002/2015JD023586.

In Chapter 6, I summarize the conclusions from this work and discuss current and future work. Work in Chapters 3 and 5 are slightly modified versions of previously published journal articles.

Chapter 2

An Overview of Approaches to Atmospheric River Identification

Abstract

The transient nature of atmospheric rivers (ARs) as they propagate eastwards makes their identification in moisture fields a challenging task. Common identification approaches available in the literature are reviewed and contrasted using satellite-derived total precipitable water in Morphed Integrated Microwave Imagery at CIMSS (MIMIC-TPW) and integrated precipitable water (PW) and the magnitude of moisture flux from MERRA reanalysis.

2.1 Introduction

The propagation of atmospheric rivers (ARs) over the world's ocean basins is striking. ARs are easily identifiable as transient features with extended geometry in instantaneous snapshots of daily and hourly moisture fields. However, while it is simple to visually separate ARs from background moisture, an automated method of identification becomes important for an understanding of their behavior over climatological time-scales.

The purpose of this chapter is to provide a brief overview of the many AR identification methods existing in the literature and to shed some light on the identification approach used in the following chapters. The approaches summarized here do not consider the event-based definitions used to characterize ARs, such as precipitation and the magnitude of upslope winds (e.g. *Neiman et al.*, 2009; *Ralph and Dettinger*, 2012; *Ralph et al.*, 2013). While useful in hydrological studies, these approaches do not consider the geometry of ARs over the basin and so are not applicable to the type of investigation pursued in this dissertation. As our focus is on the characteristics of ARs impacting western North America, this raises the

question of how to quantify their landfall. Throughout this dissertation, landfall will refer to AR-features (high moisture or moisture flux) that make contact with predefined transect following the coastline. This method of defining landfall is consistent with approaches in the literature (e.g. *Neiman et al.*, 2008a; *Dettinger et al.*, 2011; *Lavers et al.*, 2012).

This chapter is organized as follows. In section 2.2, I start with a comparison of satellite-derived total precipitable water to integrated moisture fields in reanalysis. In sections 2.3 and 2.4, I describe integrated precipitable water and moisture flux-based methods of identification. I finish with a brief analysis of the robustness of the approach used in the following chapters.

2.2 Event description and comparison between datasets

For the purposes of comparison, I focus on a single instantaneous snapshot of an AR that formed over the North Pacific basin on 07 Jan 2009 (*Neiman et al.*, 2011). This landfalling event resulted in heavy precipitation over Western Washington. While the amount of resulting rainfall was not overly excessive, the warm temperatures associated with this AR storm melted existing snow and resulted in widespread flooding in several river basins in the region (*OWSC*; *Neiman et al.*, 2011).

The clear filamentary geometry of this AR over the North Pacific is evident in Fig. 2.1a, which shows satellite-derived total precipitable water in Morphed Integrated Microwave Imagery at CIMSS (MIMIC-TPW). Use of satellite-derived integrated moisture as a proxy for the high moisture transport found in ARs was established in a series of extensive case-studies (e.g. *Ralph et al.*, 2004; *Neiman et al.*, 2008a). For operational use, an automated method of AR identification using observations was developed in *Wick et al.* (2013b). These methods identify features with high moisture features ($\geq$ 2 cm) and extended geometry ($\leq$ 1000 km width, $\geq$ 2000 km length) as ARs. These characteristics are specific to ARs falling along the western coastline of the contiguous United States. The lack of horizontal wind data and spatially and temporally consistent observations basin place limitations on the scale of investigations on the characteristics of landfalling events.

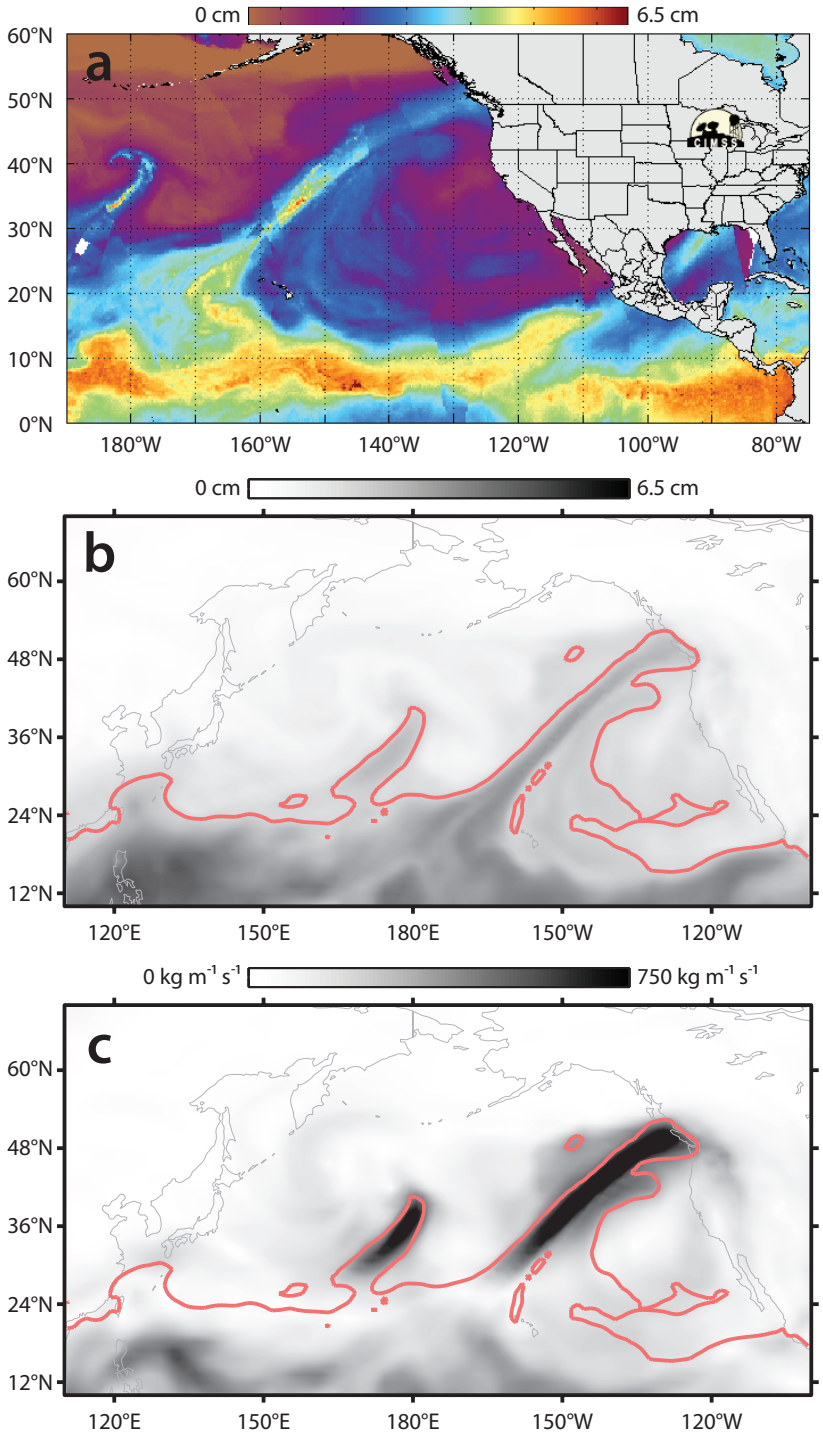

Figure 2.1: For 00:00 UTC 07 January 2009, (a) satellite-derived total precipitable water in MIMIC-TPW, (b) integrated precipitable water in MERRA reanalysis and (c) the magnitude of moisture flux in MERRA reanalysis. In (b) and (c), for reference, the 2 cm precipitable water contour is shown in pink.

Use of reanalysis data addresses the limitations found in observations. For the purposes of illustration, identification methods are compared in Modern-Era Retrospective-analysis for Research and Applications (MERRA; *Rienecker et al.*, 2011) reanalysis. Details on this reanalysis dataset can be found in Chapter 3. Calculated moisture fields include column integrated precipitable water (PW),

$$PW(\lambda, \phi, t) = (g\rho_w)^{-1} \int_{p_s}^{p_t} q(\lambda, \phi, p, t) \mathrm{d}p, \tag{2.1}$$

and the magnitude of column integrated moisture flux (MF),

$$MF(\lambda, \phi, t) = g^{-1} \left| \int_{p_s}^{p_t} q(\lambda, \phi, p, t) \mathbf{V}(\lambda, \phi, p, t) \mathrm{d}p \right|, \tag{2.2}$$

where ρ_w is 1000 kg m^{-3}, g is 9.81 m s^{-2}, p_s is 1000 hPa, $\mathbf{V}$ is the horizontal velocity and q is specific humidity (both in SI units). While the value of p_t varies in the literature from 700 hPa to 100 hPa (e.g. *Zhu and Newell*, 1998; *Lavers et al.*, 2012; *Payne and Magnusdottir*, 2014; *Rutz et al.*, 2014), for consistency with our definition in Chapter 1, we use 500 hPa.

Comparison of PW to observations shows good agreement in both the magnitude and location of the AR (comparison of Figs. 2.1a to 2.1b). The availability of horizontal wind data at high vertical resolution mean that the moisture transport within ARs can be directly investigated (Fig. 2.1c), where the narrow geometry of the AR in the East Pacific becomes even more apparent. For reference, the 2 cm PW contour, commonly used to indicate high atmospheric moisture (*Ralph et al.*, 2004), is shown in pink in Figs. 2.1b and 2.1c. In the following subsections, methods to separate out AR features from background moisture fields are summarized.

2.3 PW-based identification

For comparison, Fig. 2.2a shows an example of the observation-based method of identification used in *Neiman et al.* (2008a), which is typically applied to observations, but here is applied to reanalysis. The elongated geometry of an AR-feature is either visually identified (as in *Neiman et al.*, 2008a) or separated from background moisture using a skeletonization ap-

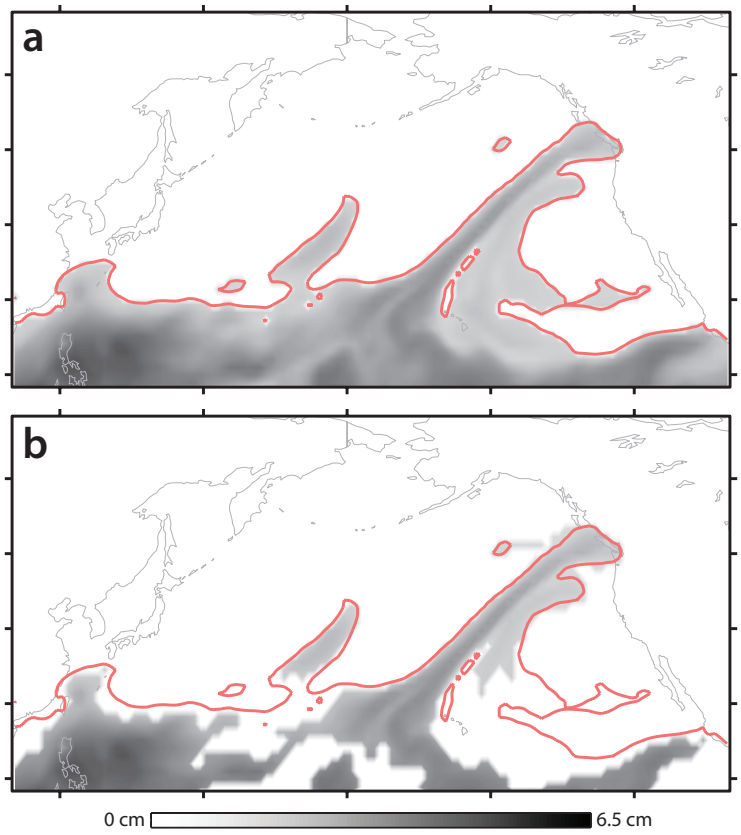

Figure 2.2: For 00:00 UTC 07 January 2009, (a) the observation-based method from (*Ralph et al.*, 2004) and (b) the identification method used in *Jiang and Deng* (2011). For reference, the 2 cm PW contour is shown in pink in each panel.

proach to trace the 'backbone' of high moisture (as in *Wick et al.*, 2013b). However, the difficulty with a static threshold on PW is in the boundary between AR-like features and high moisture in the tropics, where the boundary becomes indistinct.

In a study focusing on the downstream modulation of AR activity along the western coastline of North America, *Jiang and Deng* (2011) introduced an objective method of separating PW from background moisture based on an earlier approach in *Zhu and Newell* (1998, detailed in section 2.4). They used a spatially-dynamic threshold in both the meridional and zonal directions label grid points over the North Pacific as AR grid points over a 32 year period to calculate AR frequency of occurrence over the basin. By this method, AR associated

PW (PW_r) is calculated as,

$$\begin{aligned} PW_r &\geq PW_{zmean} + A\left(PW_{zmax} - PW_{zmean}\right), \\ PW_r &\geq PW_{mmean} + B\left(PW_{mmax} - PW_{mmean}\right), \end{aligned} \tag{2.3}$$

for the zonal (z) and meridional (m) directions and where A and B are tuned constants equal to 0.3 and 0.1, respectively. While there is some improvement in the filamentary structure of the AR over the eastern North Pacific, specifically in the subtropics near Hawaii, the large tropical signature still apparent in the western North Pacific is inconsistent with our definition from Chapter 1. Improvements to this approach include the use of observation-based constraints on geometry (e.g. *Jiang et al.*, 2014; *Rivera et al.*, 2014), however, it is more common that identification approaches use *MF*, as discussed in the next subsection.

2.4 MF-based identification

2.4.1 Overview

In one of the earliest studies to investigate the global occurrence of ARs, *Zhu and Newell* (1998) developed a method to isolate AR-features using reanalysis and modelling data. They demonstrated that traditional methods of partitioning moisture fluxes into time and zonal mean flow and transient and stationary eddies neglect important moisture transport mechanisms at very short timescales, namely ARs. Their method uses spatially-dynamic thresholding to separate the total moisture flux (MF_t) into so-called broad fluxes (MF_b) and river fluxes (MF_r), where,

$$MF_t = MF_b + MF_r, \tag{2.4}$$

and where MF_r is defined as,

$$MF_r \geq MF_{mean} + 0.3\left(MF_{max} - MF_{mean}\right). \tag{2.5}$$

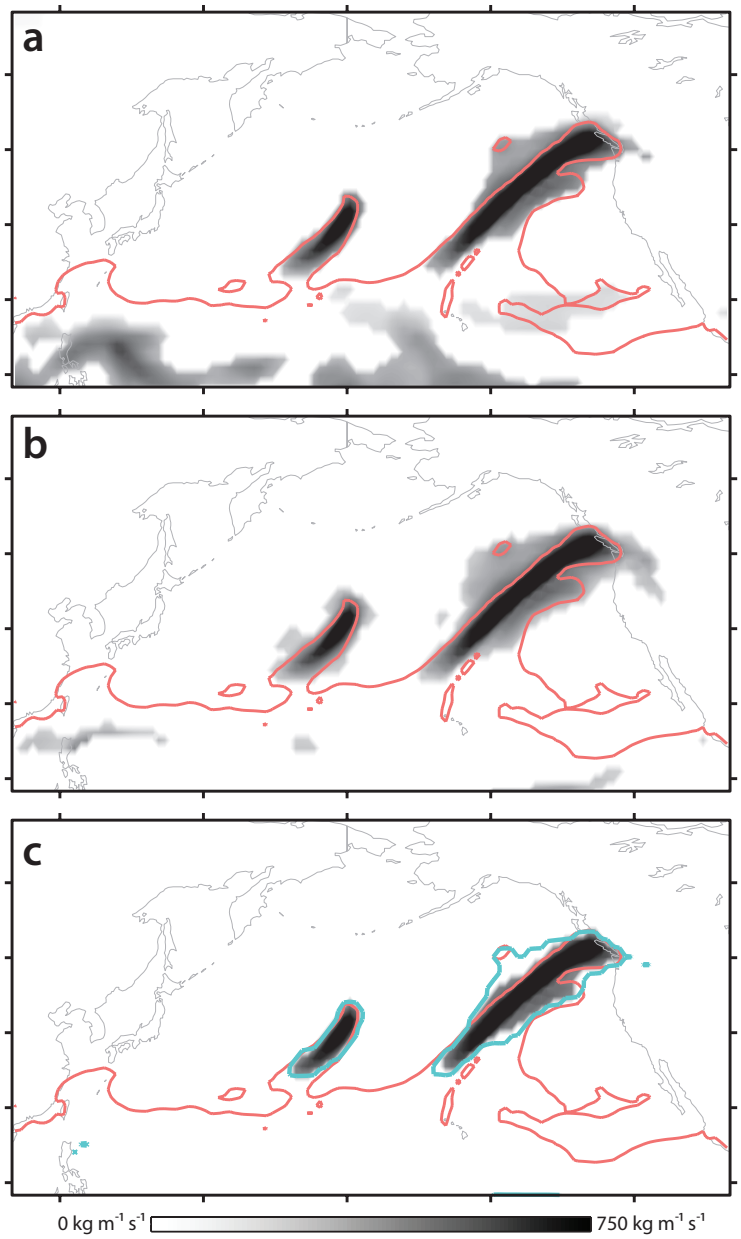

Figure 2.3: For 00:00 UTC 07 January 2009, (a) the *Zhu and Newell* (1998) method, (b) a static threshold of 250 kg m^{-1} s^{-1} used in *Rutz et al.* (2014) and (c) the observation-based method from *Lavers et al.* (2012) and *Payne and Magnusdottir* (2014). In (c), the effect of the landfall region on the magnitude of the ivt threshold is seen in blue. For reference, the 2 cm PW contour is shown in pink in each panel.

MF_{max} and MF_{mean} are the maximum and mean zonal moisture flux, respectively, and 0.3 is a constant tuned to the data and time period used in *Zhu and Newell* (1998). Figure 2.3a illustrates the effect of this method on MF, showing a clear separation of AR-like features

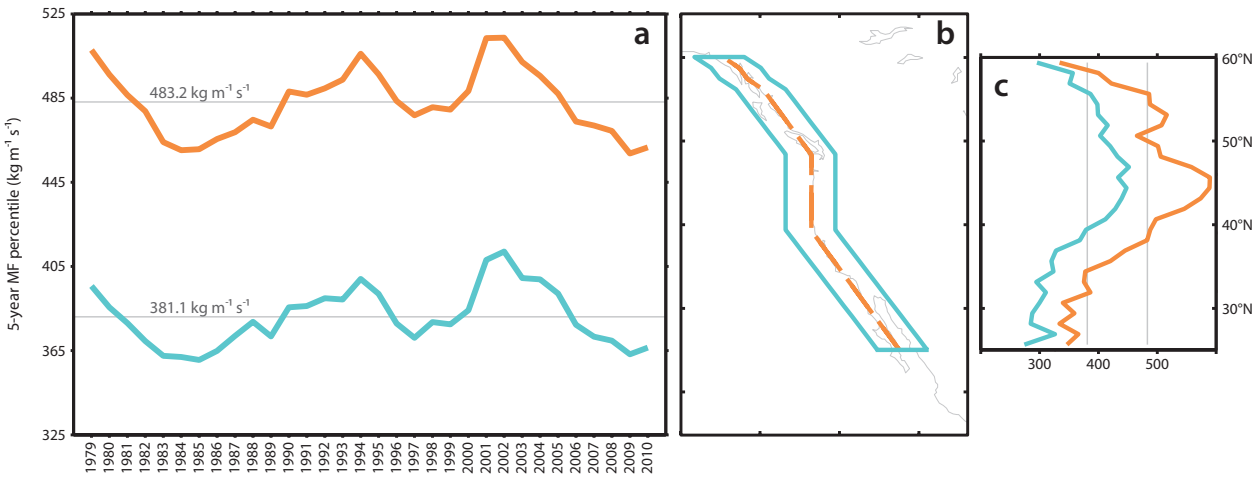

Figure 2.4: (a) *MF* percentiles for the landfalling regions shown in (b), calculated over 5-year running windows starting from 1979. The *MF* percentile for each region over the entire 36 year dataset is shown in grey text. (c) A comparison of a latitudinally-variable percentile threshold on *MF* for each region shown in (b).

over the extratropics. However, as this approach is subject to the constant used, comparison of ARs identified between two datasets can be somewhat subjective. In an investigation of in-land penetrating ARs, *Rutz et al.* (2014) explored their sensitivity to a static threshold on *MF*. They found effects on the magnitude of AR frequency with variations in this threshold, but little effect on the location of AR landfall. The threshold used in *Rutz et al.* (2014) serves as an unofficial threshold on *MF* over the North Pacific. Improvement in the representation of ARs over the region compared to the method used in *Zhu and Newell* (1998) is shown in Fig. 2.1b. *Rutz et al.* (2014) also showed that the length and width constraints used in observational studies were somewhat redundant when *MF* was used, as identified features above 250 kg m^{-1} s^{-1} were typically filamentary by default.

As a consequence of the focus on the North Pacific, many of the observational constraints on moisture and moisture transport are specific to the region. In a study focusing on the effect of landfalling ARs on Great Britain, *Lavers et al.* (2012) calculated the percentile threshold of *MF* along a cross-section following the North American coastline for ARs reported in *Neiman et al.* (2008b). They found an average percentile threshold of 85% over five different reanalysis

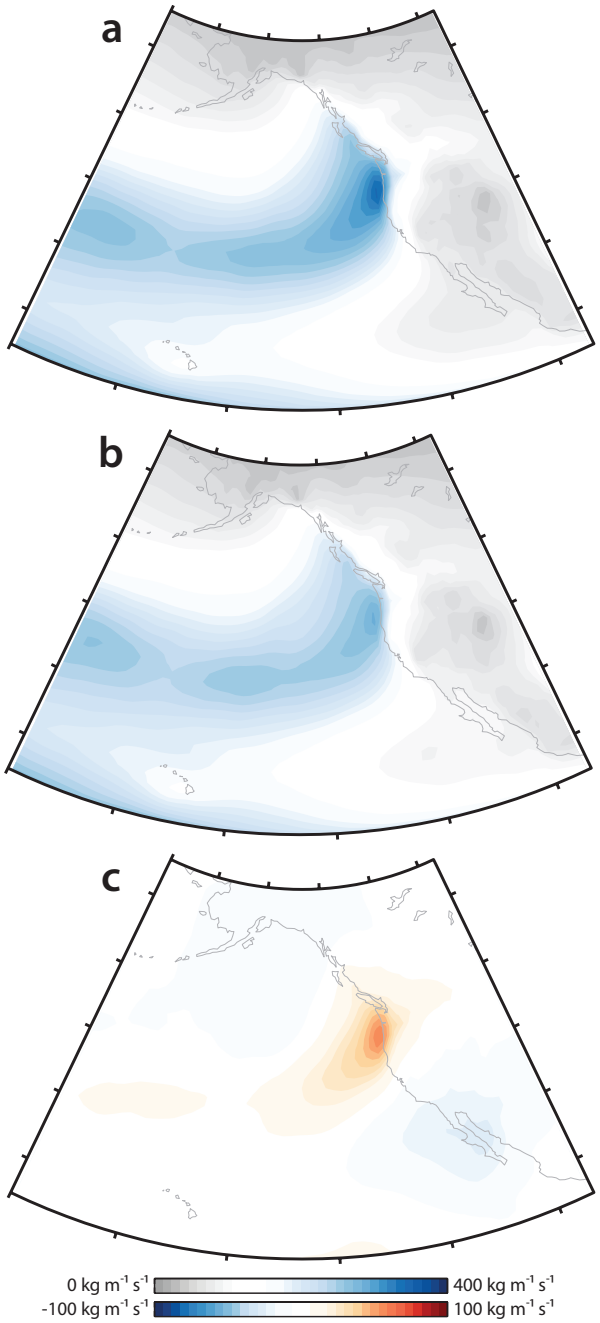

Figure 2.5: (a) *MF* percentiles for the landfalling regions shown in (b) calculated over 5-year running windows starting from 1979. The whole period *MF* percentile for each region is shown in grey text. (c) A comparison of a latitudinally-variable percentile threshold on *MF* for each region shown in (b).

products. The combination of a percentile threshold on *MF* with observational thresholds on lower level winds ($\geq$ 10 m s^{-1}) show much improvement in the isolation of the two ARs over the basin (Fig. 2.2c) and this basic approach is widely used in the literature for the investigation of landfalling ARs (e.g. *Lavers et al.*, 2012, 2013; *Ramos et al.*, 2015; *Warner et al.*, 2015; *Payne and Magnusdottir*, 2014, 2015; *Guan and Waliser*, 2015). This basic approach is used in the following chapters of this dissertation. In the next subsection, I provide a brief analysis of its robustness.

2.4.2 Validation

Depending on the region over which landfalling *MF* is calculated, the magnitude of the percentile threshold on *MF* can vary. This can be seen in the grey lines in Fig. 2.4a which show a comparison of *MF* percentiles using either a zonally averaged region centered on the coastline or a single transect following the coastline (region shown in Fig. 2.4b). While the magnitude of these thresholds differ (381.1 kg m^{-1} s^{-1} vs. 483.2 kg m^{-1} s^{-1}, respectively), both fall above the minimum accepted *MF* threshold of 250 kg m^{-1} s^{-1} used in *Rutz et al.* (2014) for the North Pacific region. The effect of the more lenient threshold on *MF* (using the zonally averaged landfall region) on the identified AR-feature in Fig. 2.3c is shown in blue contour and demonstrates its relatively small impact.

To ensure that the percentile threshold on *MF* does not experience any systematic trends over time, Fig. 2.4a shows *MF* percentiles calculated using a 5-year running window for the two landfall regions shown in Fig. 2.4b. While interannual variability is apparent over the roughly 30 year period considered, percentiles do not show consistent trends over time. The two values calculated over the entire period (shown in grey) are considered representative.

Focusing on the impacts of landfalling ARs over Europe, work in *Lavers et al.* (2013) introduced a variation of the percentile-based method described in section 2.4 not considered in this dissertation. To test the effect of this modified methodology on the results presented in the following chapters, I provide a brief summary of its impact. Rather than calculating a single percentile threshold on *MF* for an entire transect, the 85^{th} percentile is calculated

according to the daily maximum *MF* for preset latitudinal bins. The effect of this variation on the thresholds discussed previously is shown in Fig. 2.4c. Introducing latitudinal dependence in the calculation, means that thresholds are underestimated over the Pacific Northwest and overestimated over Southern California and Baja relative to the thresholds in Fig. 2.4a (the grey lines in Fig. 2.4a and 2.4c are the same). This can be seen in a composite analysis of landfalling ARs timesteps in *MF* identified using a static 85^{th} percentile threshold (as described in section 2.4, Fig. 2.5a) and a latitudinally-dependent 85^{th} percentile threshold (as described in this section, Fig. 2.5b). The difference between the two composites is shown in Fig. 2.5c. Consistent with a lower threshold over the Pacific Northwest, Fig. 2.5a shows a larger average *MF* associated with landfalling ARs. Despite these differences, the two methods show 85% overlap between identified landfalling dates. Furthermore, composite analysis of the dates not included in the definition in section 2.4 show that the overlooked ARs do not necessarily follow the typical geometry described by previous methods. Composite analysis of the dynamical fields investigated in this dissertation using this new dataset was performed and show little difference between the two datasets (not shown).

2.5 Concluding Remarks

In this section, I summarize several methods of AR identification found in the literature. Comparison of the different approaches demonstrates the usefulness of the precentile-based threshold on *MF* for separating AR-features from background moisture fields. Variations of this approach are used in the following chapters to identify AR conditions along the coastline of North America.

Chapter 3

Dynamics of landfalling atmospheric rivers over the North Pacific in thirty years of MERRA reanalysis

As appears in:

Payne, A. E. and G. Magnusdottir (2014), Dynamics of landfalling atmospheric rivers over the North Pacific in thirty years of MERRA reanalysis. *Journal of Climate*, **27**(18), 7133 - 7150, doi: 10.1175/JCLI-D-14-00034.1.

Abstract

A large-scale analysis of landfalling atmospheric rivers (ARs) along the west coast of North America and their association with the upper tropospheric flow is performed for the extended winter (November through March) for the years 1979 to 2011 using MERRA reanalysis data. The climatology, relationship to the El Niño - Southern Oscillation and the Madden - Julian Oscillation, and upper-level characteristics of approximately 750 ARs are presented based on the 85^{th} percentile of peak daily moisture flux. AR occurrence along the West Coast is dominated by early season events. In composites of upper level fields during AR occurrences, certain characteristics stand out irrespective of the tropical climate indices. This suggests that extratropical dynamical processes play a key role in AR dynamics.

The influence of the large scale circulation on AR intensity prior to landfall is examined by objectively selecting an extreme subset of 112 AR dates representing the 95^{th} percentile of strongest cases. Each AR date that is identified is traced backwards in time using a novel semi-automated tracking algorithm based on spatially and temporally connected organized

features in integrated moisture transport. Composites of dynamical fields following the eastward progression of ARs show a close relationship between the location of the jet, Rossby wave propagation and anticyclonic Rossby wave breaking in the upper troposphere of the east Pacific and moisture transport in the lower troposphere. Comparison between the strongest and the weakest ARs within our extreme subset shows differences in both the intensity of moisture transport and the scale and development of anticyclonic Rossby wave breaking in the east Pacific.

3.1 Introduction

Work over the Pacific basin has focused on the roles of El Niño - Southern Oscillation (ENSO), the Madden-Julian Oscillation (MJO), and the Pacific-North American pattern (PNA) in modulating the behavior of North Pacific atmospheric rivers (ARs) (*Higgins et al.*, 2000; *Bao et al.*, 2006; *Ryoo et al.*, 2013; *Mo and Higgins*, 1998a,b; *Jones*, 2000; *Ralph et al.*, 2011; *Guan et al.*, 2012, 2013). Most of these studies have based their conclusions on correlations between the signatures of ARs on land (such as total rainfall and snow water equivalent) and climate mode indices, rather than direct detection of ARs and the dynamical processes driving them. Very few studies have focused on the evolution of the feature itself over the Pacific prior to landfall. *Ralph et al.* (2011) performed a detailed case study of the development of a single AR over the Pacific basin and attempted to tie its formation and behavior to changes in moisture availability due to the progression of the MJO in the tropics. In the context of the impacts of ENSO on the background flow, *Ryoo et al.* (2013) found that moisture transport is modulated by both the strength of the subtropical jet and the location of Rossby wave breaking along the west coast of North America. Both of these studies suggest a role for large-scale dynamics in modulating ARs prior to landfall.

The scope of the research on large-scale influences on ARs is limited both by the ability of each study to sample ARs and by the complexity of the multi-scale processes contributing towards AR behavior prior to landfall. Because of these limitations, it is difficult to make sweeping conclusions on the dominant mechanisms contributing to variations in AR behavior

prior to landfall. Understanding how large-scale dynamical factors influence ARs over the Pacific in the observational record is essential to our understanding of the role ARs will play in the hydrological cycle in a warmer climate.

Here we examine the climatological characteristics of landfalling ARs on the West Coast, defined by the 85^{th} percentile of peak daily moisture transport (*Lavers et al.*, 2012), over the extended winter period from 1979 to 2011. To examine their behavior prior to landfall, we develop a back tracking algorithm based on moisture flux to resolve the progression of ARs across the basin in composites. We detail the dynamical influences on the behavior of an extreme subset of ARs that have been tracked over the Pacific basin in a reanalysis product covering more than thirty years of data. We address the following questions: (1) What is the relationship between ARs and upper-level dynamics? and (2) What influences the intensity of ARs prior to landfall?

This paper is organized as follows. Data and methodology for identifying landfalling ARs, as well as selecting the cases that make up our back tracked extreme subset, are described in sections 3.2 and 3.3. In section 3.4, we provide an overview of the characteristics of landfalling ARs over the extended winter for the years 1979 to 2011. Section 3.4 also shows the relationship between moisture flux over the basin and upper level dynamics using the extreme subset of ARs. In section 3.5, we show the connection of AR intensity to Rossby wave propagation and breaking. At the end of section 3.5, we put our results linking ARs to Rossby wave breaking in context by showing the difference between breaking frequency and extent for landfalling AR dates compared to the climatology for the entire extended winter. The conclusions of this study and their implications are found in section 3.6.

3.2 Data

We use the Modern-Era Retrospective Analysis for Research and Applications (MERRA) reanalysis dataset, available starting from 1979 from NASA. Use of the MERRA product has significant advantages as it is of high spatial and temporal resolution and was developed specifically for application to the hydrological cycle (*Rienecker et al.*, 2011). Specific humid-

ity, horizontal winds, and potential vorticity were retrieved from pressure levels at reduced spatial resolution ($1.25^\circ \times 1.25^\circ$) at 3-hrly intervals. Total surface precipitation was retrieved at native spatial resolution ($2/3^\circ \times 1/2^\circ$) at 1-hrly intervals. Precipitation data is converted from units of kg m^{-2} s to units of mm and then averaged every three timesteps. The precipitation data at 3-hrly intervals is linearly interpolated to reduced spatial resolution for use with the moisture and dynamical fields.

The behavior of the ARs is examined with respect to both the MJO and ENSO using the daily Real-time Multivariate MJO (RMM) index and the monthly Multivariate ENSO Index (MEI), respectively (*Wheeler and Hendon*, 2004; *Wolter and Timlin*, 1998). MJO activity with a RMM amplitude below 1 is considered too weak to have large-scale impacts on circulation and is not considered in the following analysis. El Niño events are indicated by MEI values greater than 0.5 and La Niña events are indicated by MEI values less than -0.5. For each landfalling AR date, the MJO phase (provided the amplitude is greater than 1) and the prevailing state of ENSO are recorded.

3.3 Methods

3.3.1 AR visualization

As has been pointed out by previous researchers (e.g. *Bao et al.*, 2006; *Newman et al.*, 2012), ARs do not represent trajectories of moisture as their name might suggest, but are rather constantly evolving pathways for moisture transport, recycling moisture between the atmosphere and the underlying ocean as they move over basins. Observational researchers have long used vertically integrated water vapor content, also known as total precipitable water measured in centimeters of liquid water equivalent, as a proxy for water vapor transport accomplished in ARs (*Ralph et al.*, 2004, 2005; *Neiman et al.*, 2008a; *Jiang and Deng*, 2011; *Wick et al.*, 2013b,a). However, the use of integrated moisture is primarily motivated by a lack of in situ low-level wind data over oceanic regions. The use of a dynamically consistent reanalysis dataset makes direct investigation of moisture transport possible.

We follow the methodology in *Lavers et al.* (2012) to simplify our analysis and define the

magnitude of the vertically integrated moisture flux (*MF*), as follows:

$$MF(\lambda, \phi, t) \;=\; g^{-1} \left| \int_{p_s}^{p_t} q(\lambda, \phi, p, t) \mathbf{V}(\lambda, \phi, p, t) \mathrm{d}p \right| \tag{3.1}$$

where $\mathbf{V}$ are the horizontal winds on isobaric surfaces measured in units of m s^{-1}, q is specific humidity measured in units of kg kg^{-1}, g is the gravitational acceleration (9.81 m s^{-2}), p_s is 1000 hPa and p_t is 700 hPa. Over the Pacific basin the influence of the jet stream dominates above 700 hPa, whereas water vapor drops off very quickly with height. While previous researchers have integrated to 300 hPa, we found that vertical integration to 700 hPa was appropriate.

3.3.2 AR dataset construction

Our focus is on wintertime ARs (November through March), as they have been shown to have higher moisture transport and have greater impacts on land (*Neiman et al.*, 2008a). It is important to note that we exclude the month of October in our selection of landfalling dates. Several significant ARs have made landfall during October, impacting the Pacific Northwest in particular, generally related to recurving transitional tropical cyclones (*Lynott and Cramer*, 1966; *Ralph et al.*, 2011). However, because October is a transition season that has many characteristics of late summer, it is very difficult to detect organized structures in *MF* over the Pacific basin. The ARs making landfall during October have largely different characteristics in both trajectory and in moisture transport from the ARs making landfall in November through March.

For each date between November 1^{st} and March 31^{st} for the years 1979 to 2011, we record two values: (1) peak daily *MF* and (2) total daily precipitation. These two values are calculated as follows. For each date, daily mean *MF* and precipitation are isolated over a seven gridpoint region, centered on the western coastline of North America between 20°N and 60°N (Fig. 3.1a-b). Within the outlined region in Fig. 3.1a, each variable is averaged in

the zonal direction. The blue and orange lines in Fig. 3.1c show the seven point averaged distributions for *MF* and precipitation, respectively. For each date, the peak *MF* and the total precipitation, summed over a seventeen gridpoint window in the latitudinal direction and centered on the peak *MF*, are recorded (Fig. 3.1c). Figure 3.1c shows an example of the seventeen-point range over which precipitation is summed and the values recorded for peak *MF* and total precipitation for 03 Dec 2007. The two values recorded for each date over the entire time period are illustrated in Fig. 3.2, which shows the distribution of all dates, sorted according to the peak daily *MF* (black line) and plotted with each date's total precipitation (light grey line).

We use two landfalling AR datasets in our study: (1) a climatology of all landfalling AR dates to impact the western coast of North America between 20°N and 60°N between the years 1979 and 2011 and (2) a backtracked subset of the climatology, isolating only the most extreme AR events to make landfall. The details of our methodology follow, where subsection 3.3.2a describes how we define our landfalling AR climatology, subsection 3.3.2b describes how we isolate an extreme subset of landfalling AR dates from our climatology and subsection 3.3.2c details our backtracking methods for the extreme subset of landfalling ARs.

Climatology

We define a climatology of landfalling AR dates using the 85^{th} percentile on peak daily *MF* (generally following the methods in *Lavers et al.* (2012)), where landfall is defined by physical proximity to the coastline of North America. Landfalling AR dates are all those dates in the time period with peak daily *MF* values greater than or equal to the 85^{th} percentile (233 kg m^{-1} s^{-1}). The vertical dark grey line in Fig. 3.2 shows the 85^{th} percentile of peak daily *MF*, where all dates to the right are labelled as landfalling AR dates. The green dots in Fig. 3.2 show the locations of 9 notable landfalling AR events, as listed on NOAA's Earth System Research Laboratory AR information page (*http://www.esrl.noaa.gov/psd/atmrivers/events/*).

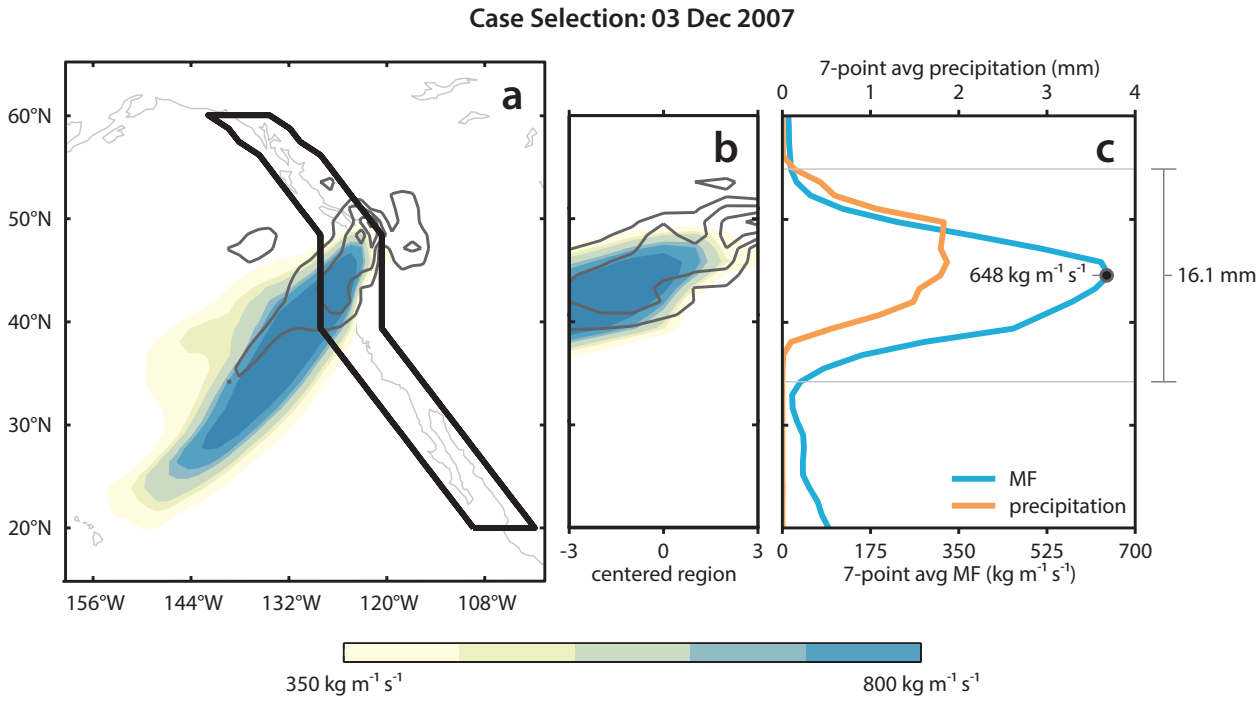

Figure 3.1: Example of the case selection methodology applied to 03 Dec 2007. (a) For each day in the time period considered, daily mean *MF* (kg m^{-1} s^{-1}, shaded) and daily mean precipitation (mm, contoured starting at 0.5 mm and increasing in intervals of 1 mm) are isolated in the region outlined in black, where (b) shows a straightened image of the two variables within the region. The two variables are then averaged over 7 grid points in the zonal direction, shown in (c). For each day, two values are recorded: the peak in daily mean 7-point averaged *MF* (blue line, c) and the sum of daily mean 7-point averaged precipitation over a 17-point range in the latitudinal direction, centered on the peak *MF*. As an example, for 03 Dec 2007, the boundaries of the 17-point range are shown in the horizontal grey lines in (c) and where the two values recorded are 648 kg m^{-1} s^{-1} (peak daily *MF*) and 16.1 mm (total daily precipitation).

Subset of extreme cases - selection

As we are unable to distinguish multi-day landfalling events or examine ARs prior to landfall with the climatology of landfalling ARs just described, case selection becomes necessary for in-depth analysis. We objectively isolate a subset of landfalling AR days, that can then be extended backwards in time using our tracking algorithm. We emphasize that no part of our case selection procedure is subjective. While our focus is on the intensity of ARs preceding landfall, rather than on any orographic influences, we recognize the importance of characterizing ARs as extreme precipitation events. Therefore, both peak daily *MF* and

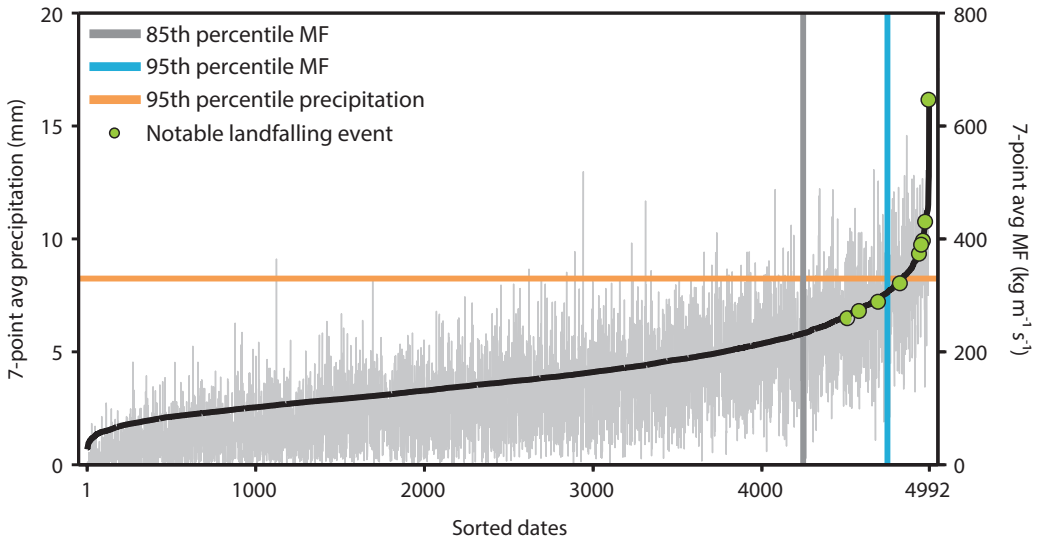

Figure 3.2: The distribution of all dates in our time period (NDJFM, 1979 to 2011) sorted according to the peak daily *MF* (kg m^{-1} s^{-1}, black line) and plotted with the associated total daily precipitation (mm, light grey line). The dark grey line shows the 85th percentile and dates to the right of this line are labeled as landfalling AR dates (749 total). Our extreme subset of cases are selected from all landfalling AR dates, with values above both the 95th percentile of peak daily *MF* (blue line) and the 95th percentile of total daily precipitation (orange line), with at least three days of separation. For validation of this methodology, 9 significant landfalling events (11 – 24 Feb 1986, 29 Dec – 04 Jan 1996/1997, 02 – 03 Feb 1998, 16 – 18 Feb 2004, 07 – 11 Jan 2005, 25 – 27 Mar 2005, 29 Dec – 02 Jan 2005/2006, 06 – 07 Nov 2006, 06 – 08 Jan 2009) are indicated by green points (multi-day events use the date with the highest peak daily *MF*).

total daily precipitation are used to select landfalling dates for our extreme subset.

Two thresholds are used to reduce the sample size for the purposes of a more detailed study and to retain the most extreme events to impact the coast. The 95th percentiles for all dates in the time period are calculated for the peak daily *MF* and associated total daily precipitation (*MF* threshold: 305 kg m^{-1} s^{-1}, precipitation threshold: 8.24 mm). All dates with peak daily *MF* and total daily precipitation that fall below the thresholds are discarded. The two thresholds on peak daily *MF* and total daily precipitation are shown as blue and orange lines, respectively, in Fig. 3.2.

A criterion is put in place to eliminate the possibility that the subset is dominated by a few large, slow moving events off the coast. For all dates with values greater than the two

thresholds, they must be separated by at least three days. This means that if two days with fewer than 3 days separation have sufficiently high values of peak daily *MF* and total daily precipitation, the date with the greater peak daily *MF* is retained and the date with the lower peak daily *MF* is discarded. Applying this logic, of all dates that had values above the set thresholds (127 dates total), 15 were discarded. Of the 15 dates discarded, 11 dates were part of the same multi-day landfalling AR event as a previously selected date. The 4 remaining dates (07 Jan 1990, 02 Feb 1991, 10 Dec 1995, 16 Dec 2002) belong to landfalling AR events directly preceding or directly following previously selected dates.

Of the 9 notable landfalling AR events mentioned previously (green dots in Fig. 3.2), only four events satisfy our criteria on both peak daily *MF* and total daily precipitation: 11 – 24 Feb 1986, 29 Dec – 04 Jan 1996/1997, 29 Dec – 02 Jan 2005/2006 and 06 – 07 Nov 2006. These four events, produced some of the largest flooding in the Pacific Northwest over the last 50 years and confirm that our case selection process does indeed isolate the most extreme landfalling ARs. When the month of October is considered, the dates originally selected remain largely the same, with 106 of the selected dates remaining the same and 19 dates being added due to October events. With improvements to our tracking methodology (description to follow) we may be able to investigate these transitional season landfalling ARs in the future.

Tracking

We developed a semi-automated algorithm to track the centroid of each selected AR back in time, over the course of its lifetime. Most previous studies only consider the few days right around AR landfall. Here, our aim is to study the development of the events, expanding the timeline of a single event beyond the few days of its landfall.

ARs are visualized over the basin, prior to landfall, using *MF* imagery with a static threshold of 350 kg m^{-1} s^{-1}. This threshold is only meant to separate peaks in *MF* from background moisture prior to landfall, over the basin, and is not used in any way to define the two datasets previously described. Moderately increasing or decreasing this threshold

only changed slightly the number of grid-points attributed to an AR and the location of its centroid, but ultimately did not affect the detection of the feature itself as an intense flux of moisture. For each timestep, connected grid points forming a unified area poleward of 23.5°N (focus on the extratropics) and greater than an area threshold of 21,000 km^2 were labeled as an instantaneous snapshot of a single AR (Fig. 3.3, top panel). The area threshold is chosen to retain only the larger scale features. Characteristics, such as the location of the centroid (the center of mass of the feature) and orientation (the angle between the a line of latitude and the major axis of the feature) of the AR, were recorded at each timestep. It should be noted that this algorithm cannot detect the exact moment of formation of the AR. However, because the focus of our study is to investigate the factors contributing to AR intensity rather than its formation, we consider the identification of its first appearance as an organized feature in the extratropics to be a good approximation.

We define the lifetime of an AR to be the series of instantaneous snapshots of connected gridpoints that are linked through time. An example of our process is shown in Fig. 3.3. Through the process described above, we identify the centroids of each possible AR over the Pacific basin at each timestep. The time-intensive part of our method comes with the manual recording of the selected AR's centroid over each timestep. While an automated method to track connected features in both space and time was developed, it was discarded pending further development because centroid locations attributed to each AR were at times inconsistent. Our criteria for linking centroids over time is as follows: (1) The centroid of the tracked feature at landfall must correspond to the selected landfalling date chosen using the methods described in the previous subsection. (2) The general progression of centroids should be eastwards. There is some east-west jumping in centroid location associated with the addition of remnant moisture to the selected feature, but it is quite minor compared to the overall progression of the feature in time. (3) The centroid of the westernmost feature is selected when two features merge (this can be seen between the 00h and 15h timesteps in Fig. 3.3).

For the 112 AR events tracked using our algorithm, we rank the events in order of weakest to strongest according to each AR's lifetime average of the areal maximum *MF* recorded at each timestep. This ranking system takes into account the entire AR lifetime rather than only its landfalling intensity and allows us to compare and contrast quantitatively the weakest and strongest ARs in the subset. The lifetime average intensities range from 533 kg m^{-1} s^{-1} to 1001 kg m^{-1} s^{-1}. It should be emphasized here that ARs are by definition extreme events and that the 'weak' ARs we refer to in our data subset are those selected ARs with the lowest lifetime average of maximum *MF*.

3.3.3 Composites

All composites in our study are calculated based on the longitudinal position of the AR centroid at each timestep, as regionally centered composites. The grey boxes in the following figures mark out 4 regions: (1) 175°–160°W, (2) 160°–145°W, (3) 145°–130°W, and (4) 130°–115°W. For each AR, variables are first averaged for all centroid values within a given region prior to calcu-

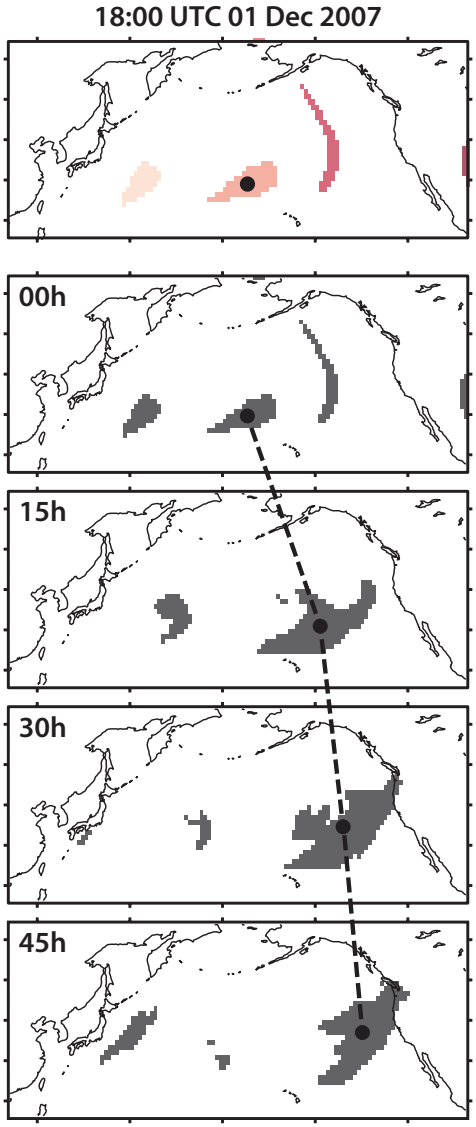

Figure 3.3: (top panel) An example of the tracking algorithm applied to 18:00 UTC 01 Dec 2007. (top panel) Separated features are colored in varying shades of pink and the centroid of the AR of interest is marked by a filled black dot. (00h – 45h) Starting from 18:00 UTC 01 Dec 2007, the AR of interest is tracked through time as indicated by the dashed black lines.

lating the composite to avoid double-counting slowly moving ARs. Even though many of the trajectories for the tracked ARs extend over the western Pacific, we limit our composites to the eastern Pacific (the four regions listed above) to avoid over-sampling the longest lived ARs.

3.3.4 Rossby wave breaking and diagnosis

Rossby wave breaking (RWB) is defined as the rapid and irreversible overturning of potential vorticity (PV) contours (*McIntyre and Palmer*, 1983). Rossby waves propagate along a strong PV gradient and break when the gradient is weakened, such as in a jet exit region. For composites we use PV on the 200 hPa surface to detect breaking and determine the type of breaking: anticyclonic, in which contours overturn in the SW-NE direction, or cyclonic, in which contours overturn in the NW-SE direction. Breaking type is determined on a case by case basis based on breaking direction (See Fig. 1 in *Strong and Magnusdottir*, 2008a). The impact of the breaking events is on forcing of the background flow, often determined to be greater when the spatial scale of the breaking is greater.

The location and zonal extent of each breaking event is quantified using a RWB detection algorithm first described in *Strong and Magnusdottir* (2008a) and adapted to 3-hrly MERRA PV data at 200 hPa (coarsened to a resolution of $2.5^\circ \times 2.5^\circ$ using linear interpolation). With this method, the Northern Hemisphere 200 hPa PV field is divided into 400 bins of equal area of approximately 6.4×10^5 km^2. For each 3-hrly timestep, we identify the longest circumpolar PV contour considering all contours between 0 and 20 PVU* (at an interval of 0.5 PVU). If overturning is detected (contour crosses a meridian more than once), the centroid of the breaking 'bay' and zonal extent (L, calculated as the degree arc length of a great circle passing through the centroid and spanning the breaking bay), and contour on which the breaking is detected are recorded (for details, see appendix in *Strong and Magnusdottir* (2008a)). For each bin centered on (λ, ϕ) and numbered $n = 1, \ldots, N$, the relative frequency of breaking (γ) and mean zonal extent of breaking ($\overline{L}$) are calculated as

*1 Potential Vorticity Unit (PVU) $\equiv 10^{-6}$ m^2 s^{-1} K kg^{-1}

follows:

$$\gamma(\lambda,\phi)_n \equiv \frac{1}{T}\sum_{t=1}^{T}\beta[(\lambda,\phi)_n,t] \tag{3.2}$$

$$\overline{L}(\lambda,\phi)_n \equiv \frac{1}{\sum_{t=1}^{T}\beta}\sum_{t=1}^{T}L[(\lambda,\phi)_n,t] \tag{3.3}$$

where,

$$\beta[(\lambda,\phi)_n,t] = \begin{cases} 1 & \text{if centroid is present} \\ 0 & \text{otherwise} \end{cases} \tag{3.4}$$

and where T is the total number of 3-hrly observations. For each type of breaking (anticyclonic and cyclonic), γ quantifies the spatial frequency of breaking for a given time period, where areas of high breaking frequency typically overlap areas of large zonal extents.

3.4 Characteristics of ARs at landfall

3.4.1 Climatology for extended winter

First we consider the landfalling characteristics of ARs off the west coast of North America using daily averages for the extended winter (November through March) 1979 - 2011. Landfall is defined as physical proximity to land, as shown in Fig. 3.1a. As described in section 3.3.2, our climatology of landfalling ARs is composed of all dates for which at least three gridpoints in the zonal direction, within the boxed region of Fig. 3.1, have peak daily *MF* values greater than a set threshold based on the 85^{th} percentile. Of the 4992 dates in the entire time period, 749 are retained as landfalling AR dates. Of the 128 AR dates listed in the climatology in *Neiman et al.* (2008a), 77 are contained in our climatology and an additional 16 occur in close proximity (within $\pm$ 2 days) to dates in our climatology. Moreover, a number of ARs identified in our study are not included in the Neiman climatology.

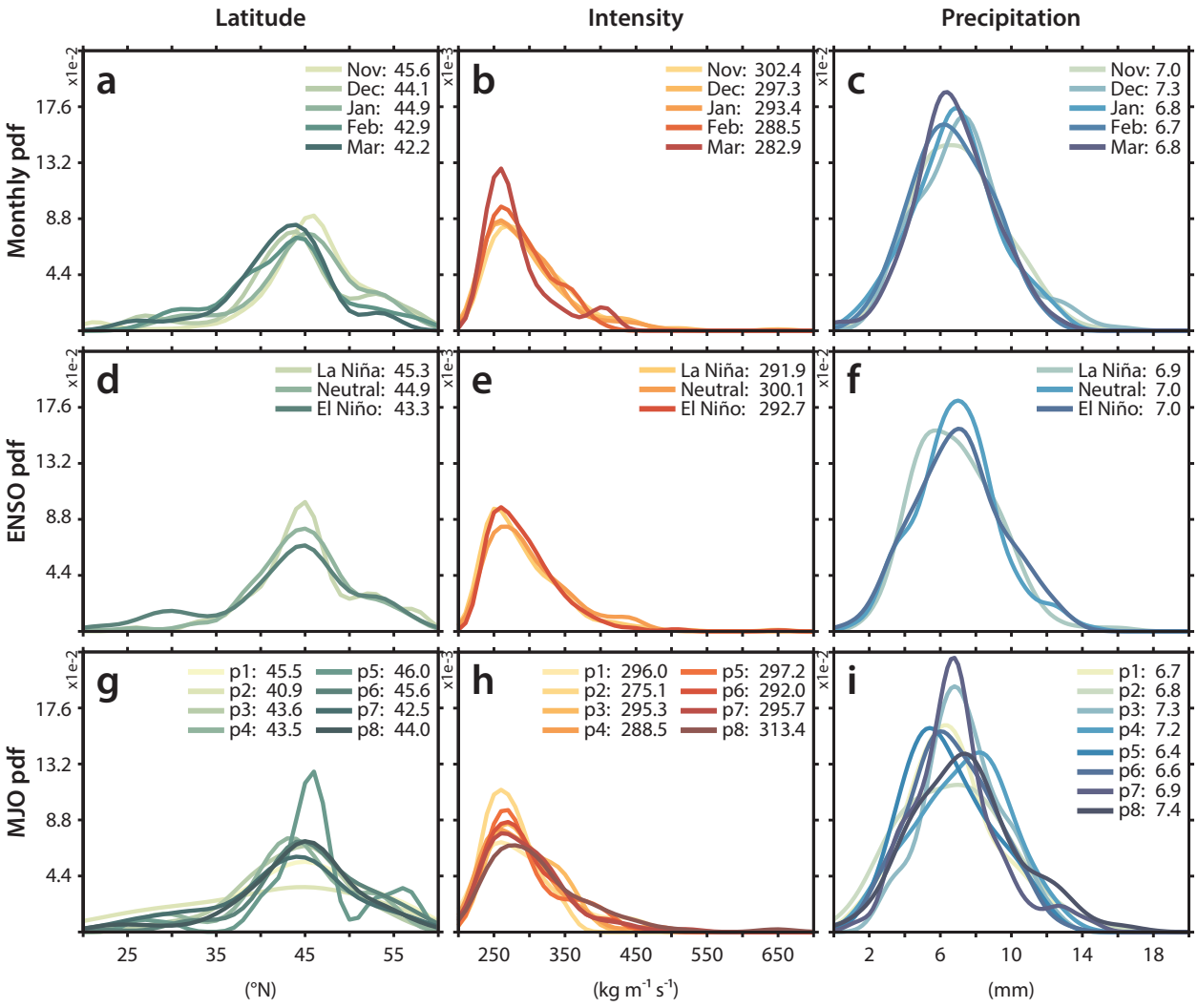

Figure 3.4: Probability density functions for landfalling ARs over the extended winter for the years 1979 to 2011 sorted according to: (a-c) month - 749 dates, (d-f) ENSO phase - 749 dates and (g-i) MJO phases with amplitudes greater than one - 469 dates. Each column shows the distribution of: (a,d,g) landfalling latitude, (b,e,h) landfalling peak daily *MF* and (c,f,i) landfalling total daily precipitation. The y-axis shows the probability density function for each panel, where the center column is an order of magnitude less than the right and left columns. Averages for each category are shown in the legend of each panel.

Differences between the two climatologies are likely attributable to different definitions of AR landfall and the use of *MF* rather than integrated water vapor, as was used in *Neiman et al.* (2008a). The 749 dates contain all of the most recent notable landfalling AR events (seen in Fig. 3.2).

The largest number of landfalling dates occur early in the season. An average of 6.1 landfalling dates occurred in November (202 dates total), 5.8 in December (192 dates total), 5.2 in January (179 dates total), 3.2 in February (110 dates total) and 1.9 in March (67 dates total). The decrease in the number of landfalling dates over the course of the season is in general agreement with the findings in *Neiman et al.* (2008a, their Fig. 2), which are based on observations of SSM/I integrated water vapor plumes for 1998 to 2005.

Figure 3.4a shows the seasonal breakdown of landfalling latitude. Landfalling latitudes show a shift equatorward towards the end of the season, from an average latitude in November of 45.6°N to a March average of 42.2°N. This shift is also seen in landfalling peak daily *MF* (Fig. 3.4b). The most intense landfalling AR dates occur in the month of November (302.3 kg m^{-1} s^{-1}) and the weakest occur in the month of March (283.6 kg m^{-1} s^{-1}). While, associated landfalling total daily precipitation do not show a similar trend (Fig. 3.4c), precipitation anomalies (based on the daily climatology) show a shift equatorward over the course of the season (not shown).

3.4.2 Effects of the MJO and ENSO on ARs

We perform an analysis of the roles of ENSO and the MJO in modulating ARs at landfall using the MEI and RMM indices, respectively. While these large-scale patterns certainly influence the precipitation distribution in the western United States (*Ropelewski and Halpert*, 1987; *Cayan et al.*, 1999; *Higgins et al.*, 2000; *Jones*, 2000), our purpose here is to investigate whether they play a direct role in AR behavior at landfall. In our analysis of the MJO, we limit our investigation to amplitudes of the MJO index greater than 1, reducing the number of dates from 749 to 469 landfalling AR dates.

The largest number of landfalling dates occur during El Niño (301 dates), the fewest

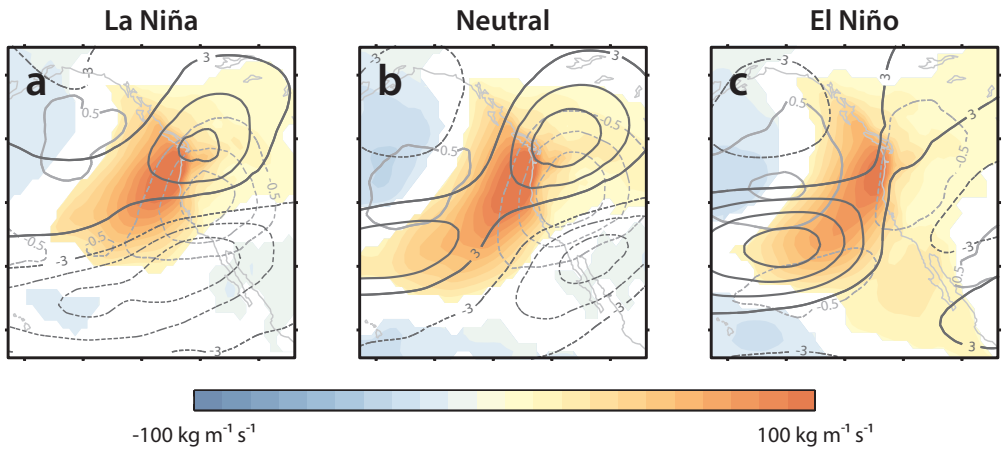

Figure 3.5: Composite 200 hPa zonal wind anomalies (dark grey contours, intervals of 3 m s^{-1}), 200 hPa PV anomalies (light grey contours, intervals of 0.5 PVU), and *MF* anomalies (shaded, intervals of 10 kg m^{-1} s^{-1}), with negative contours dashed, for (a) La Niña - 180 dates, (b) neutral - 268 dates, and (c) El Niño - 301 dates, for all 749 ARs over the extended winter over the years 1979 to 2011 (15°N to 65°N, 160°W to 115°W). Anomalies are calculated from the daily climatology of each variable. Statistical significance is calculated using Student's t-test at the 95% level.

during La Niña (180 dates), and 268 landfalling dates occurring during ENSO neutral conditions. Figures 3.4d-e show the breakdown of landfalling latitude, intensity and precipitation by phase of ENSO. Landfalling latitudes during El Niño events are shifted equatorward, with an average latitude of 43.3°N compared to an average latitude of 45.5°N and 44.9°N for La Niña and neutral phases, respectively. While total precipitation remains similar (Fig. 3.4f), the poleward shift in landfalling latitude during La Niña events and concentration of positive precipitation anomalies in the Pacific Northwest (not shown) is consistent with wintertime precipitation patterns for the region during La Niña (NOAA Climate Prediction Center). Increased intensity of moisture plumes during ENSO neutral landfalling dates is consistent with previous findings (*Higgins et al.*, 2000; *Bao et al.*, 2006). Landfalling intensities for El Niño and La Niña dates show little difference (Fig. 3.4e).

Figure 3.5 shows the composite anomalies of 200 hPa zonal wind (dark grey contours) and PV (light grey contours), and the composite anomalies of *MF* (shaded) for each phase of ENSO. Anomalies are calculated from the daily climatology for each variable and only

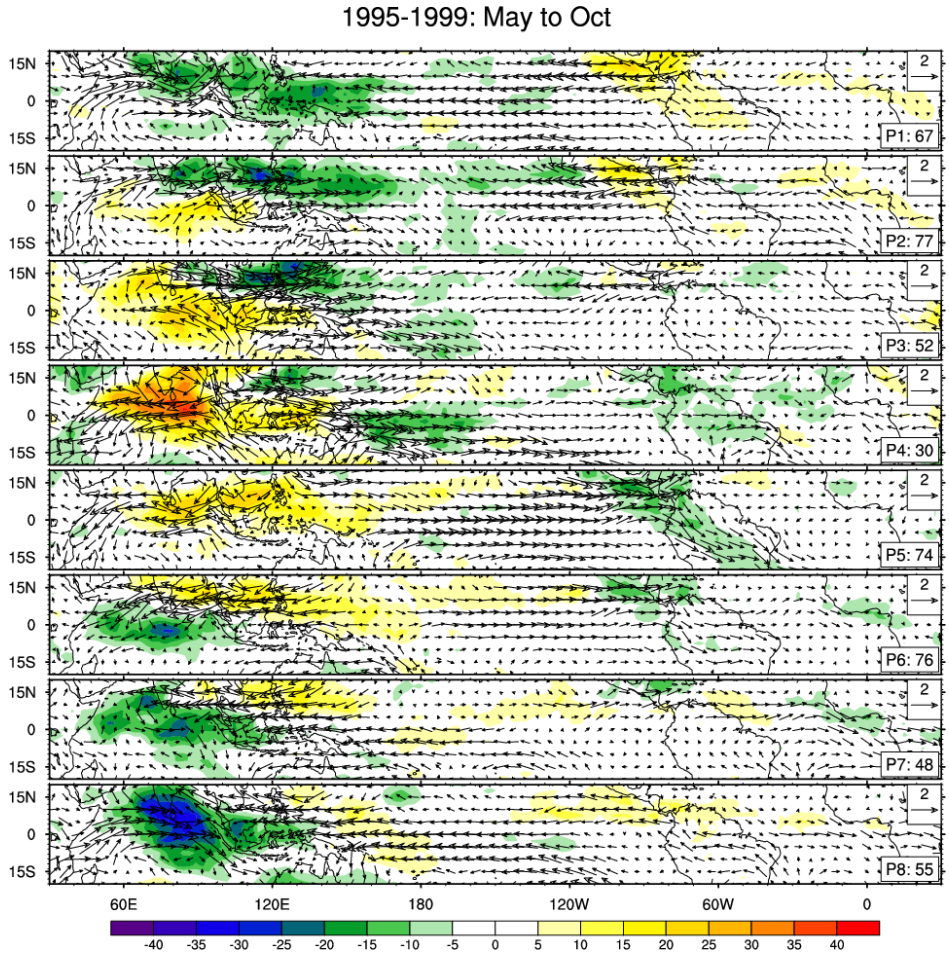

Figure 3.6: Life-cycle of the Madden-Julian Oscillation from Outgoing Longwave Radiation (OLR) and 850 hPa horizontal winds 20 - 100 day band passed anomalies over the years 1995 to 1999. The phase of each composite is shown in the lower right corner. Figure is from Climate Data Guide and is produced by D. Shea.

significant *MF* anomalies are shown (calculated at the 95% level using Student's t-test). Comparison of Figs. 3.5a and 3.5c show a clear equatorward shift in the zonal wind during El Niño dates that is in agreement with Fig. 3.4d. Significant *MF* anomalies during El Niño dates cover the entire coastline from Mexico to Alaska. The significant composite anomaly does not extend south of 35°N during La Niña and neutral dates. Warm phase positive precipitation anomalies mirror the meridionally extended range of *MF* anomalies (not shown), consistent with wintertime precipitation patterns during El Niño (NOAA Climate Prediction Center). The most noticeable difference between the different parts of Fig. 3.5 is in the zonal

wind anomalies. El Niño landfalling dates are associated with an equatorward shifted jet. This suggests that the major role ENSO plays in modulating landfalling ARs is through influence on the position of the jet, which affects the location of the Rossby wave breaking region, as will be discussed in Section 3.4.3.

Figures 3.4g-i show the breakdown of landfalling latitude, intensity and precipitation by phase of the MJO (a composite description of the MJO is shown in Fig. 3.6). There are two local maxima in the overall number of landfalling AR dates by phase (not shown). The largest number of landfalling AR dates occur during phase 6 (84 dates) and increased activity in phases 7 and 8 (71 dates each), and a smaller secondary peak occurs at phase 3 (62 dates). The peak in AR activity in association with phase 3 (when tropical convection is over the Indian Ocean) and the phase 7-8 increases are consistent with findings in *Jones* (2000). The peak at phase 6 is consistent with the increase in AR activity described in *Guan et al.* (2012). While there is no clear trend in landfalling latitude, phases 2 and 5 have the most extreme equatorward (40.9°N) and poleward (46.0°N) mean landfalling latitudes, respectively (Figs. 3.4a,d,g). The two peaks in the number of landfalling AR dates are approximately reflected in precipitation totals, with phase 3 showing the largest average at 7.3 mm and phase 5 showing the smallest average at 6.4 mm (Fig. 3.4i), consistent with wintertime precipitation patterns for the western United States (NOAA Climate Prediction Center).

Figure 3.7 shows 200 hPa zonal wind (dark grey contour) and PV (light grey contour) composite anomalies, and *MF* (shaded) composite anomalies for each phase of the MJO, showing only statistically significant *MF* anomalies. We find that positive precipitation anomalies shift approximately poleward from phase 1 to phase 8 (not shown), with the exception of phases 2 and 7. While all phases of the MJO show the presence of a statistically significant moisture anomaly, the anomaly for phase 2 is weak and spread out. It is the most equatorward reaching, consistent with the very low landfalling latitude and low intensity shown for phase 2 in Figs. 3.4g-h. The largest positive *MF* anomaly is in phase 7, which

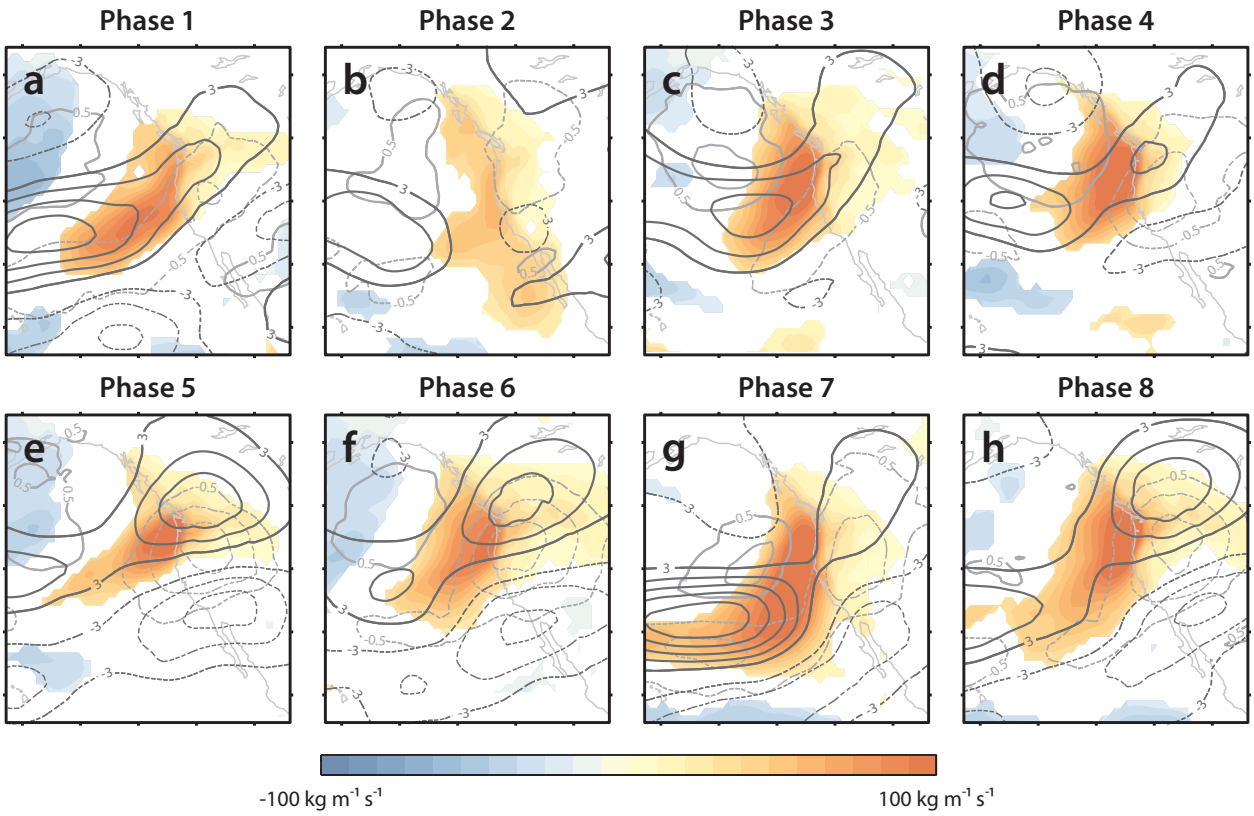

Figure 3.7: Same as Fig. 3.5, but for the MJO, for (a) phase 1 - 38 dates, (b) phase 2 - 49 dates, (c) phase 3 - 62 dates, (d) phase 4 - 43 dates, (e) phase 5 - 51 dates, (f) phase 6 - 84 dates, (g) phase 7 - 71 dates and (h) phase 8 - 71 dates, for all 469 ARs over the extended winter over the years 1979 to 2011 with RMM amplitudes greater than 1 (15°N to 65°N, 160°W to 115°W).

shows the presence of strong, equatorward zonal wind anomalies very similar to Fig. 3.5c, the El Niño composite. Phase 8, which has the largest landfalling intensity and precipitation total from Fig. 3.4h-i, also shows eastward extended zonal wind anomalies, consistent with higher latitude positive precipitation anomalies (not shown). MJO phases 3 and 7 have similar landfalling latitudes, intensities and precipitation patterns (not shown).

A strong common characteristic between AR composites during ENSO and MJO phases is the presence of a perturbed PV field in the eastern Pacific, in the location of the jet exit region, as indicated by the negative PV anomalies centered over the coastline in Figs. 3.5 and 3.7. The composites in this section suggest that, while ARs may be modulated by tropical influences on the extratropics, AR variability is ultimately strongly tied to extratopical

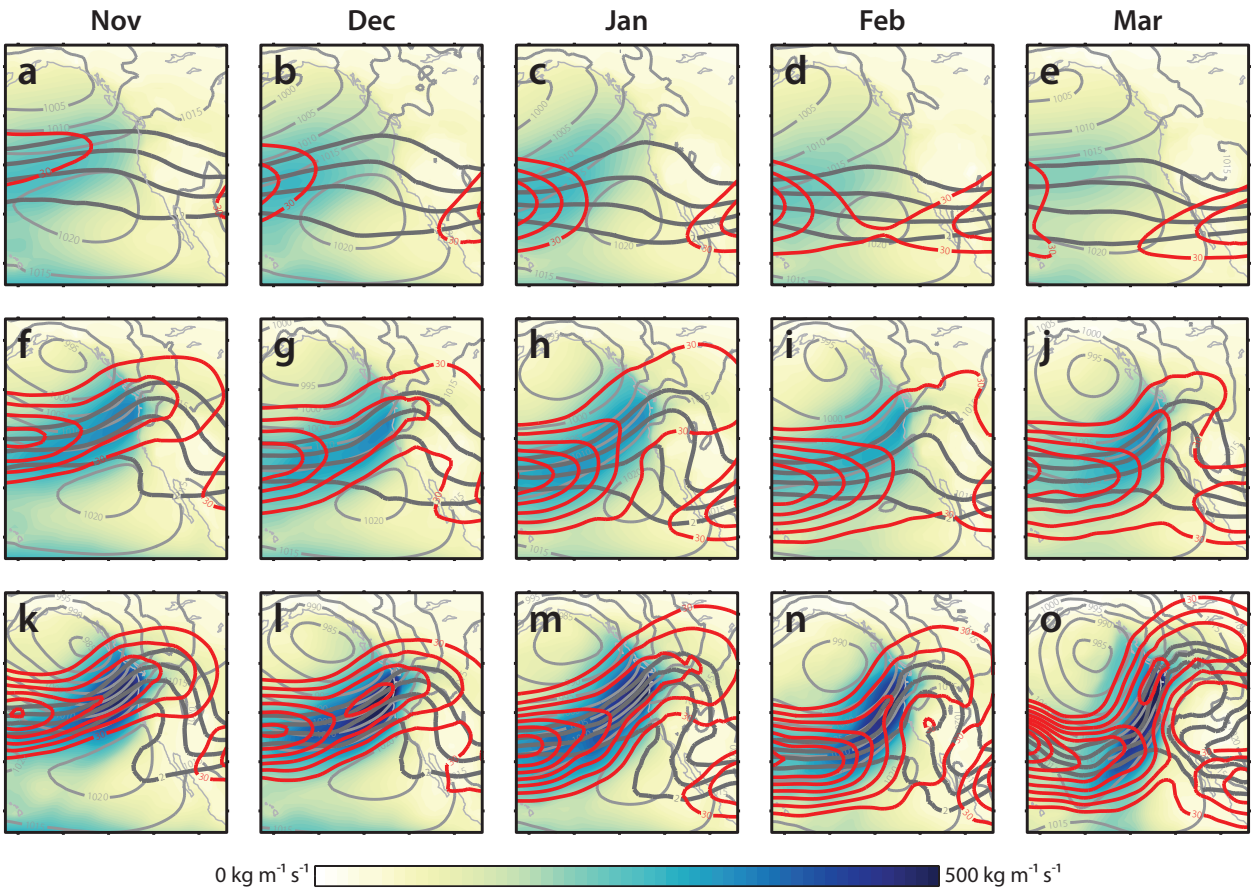

Figure 3.8: Composite SLP (light grey contour, intervals of 5 hPa), PV at 200 hPa (dark grey contour, intervals of 1 PVU), wind speed at 200 hPa (red contour, intervals of 5 m s^{-1}) and *MF* (shaded) for (a,f,k) November, (b,g,l) December, (c,h,m) January, (d,i,n) February, and (e,j,o) March for (top row) the climatological mean of the extended winter over the years 1979 to 2011, (middle row) all 749 ARs over the extended winter over the years 1979 to 2011 and (bottom row) the 112 selected landfalling dates (15°N to 65°N, 160°W to 115°W).

dynamical mechanisms. This common characteristic motivates our investigation of the dynamical mechanisms modulating ARs.

3.4.3 Dynamical perspective

We consider how landfalling AR dates are different from the mean state. Figure 3.8 shows composite SLP, 200 hPa PV, 200 hPa wind speed and *MF* for each winter month for: (a-e) the entire period (1979 – 2011), irrespective of peak daily *MF*, (f-j) all 749 landfalling AR dates (dates with values above the 85^{th} percentile of peak daily *MF*), and (k-o) all 112 selected AR

dates (dates with values above the 95^{th} percentiles of peak daily *MF* and associated total daily precipitation). Composites in Fig. 3.8f-j are composed of 202, 191, 179, 110 and 67 individual dates, respectively. Composites in Fig. 3.8k-o are composed of 34, 31, 27, 14 and 6 individual dates, respectively.

Comparison of the bottom two rows of Fig. 3.8 with the top row shows a striking departure in the dynamical make-up of AR dates from the climatological mean state over the eastern Pacific in terms of Rossby wave dynamics. The top row shows an unperturbed jet, with an associated largely zonal PV field and unremarkable *MF*. For each month (each column), the two AR rows, show that associated with the strong, lower tropospheric *MF* (which defines the ARs), the PV field and the jet are deformed to a varying extent, manifesting that Rossby wave breaking is taking place. While each frame is an average over many cases, one can still see evidence of overturning PV contours and, thus, Rossby wave breaking (or nonlinear Rossby wave behavior).

All AR dates (the middle and bottom rows of Fig. 3.8) are associated with a westward retreated jet, large perturbations in the PV field and a clearly defined low pressure center to the north and a weak high pressure center to the south of the jet. The jet is climatologically in its most poleward position in November and shifts equatorward over the course of the season. This shift in the jet is reflected in the equatorward shift in landfalling latitude shown in Fig. 3.4a. Retreat of the jet maximum westward over the course of the season weakens the PV gradient and allows for distortion of the PV contours in the eastern Pacific. The reduction in the PV gradient is downstream and equatorward of the jet exit region. The relationship between the jet and PV field in the monthly composites is consistent with the findings outlined in *Abatzoglou and Magnusdottir* (2006, their Fig. 5a-b).

Comparing the extreme subset of tracked AR dates (Fig. 3.8k-o) to all AR dates (Fig. 3.8f-j), we find that, consistent with the climatology, November has the largest number of ARs with 34 events and March has the lowest number with only 6 events. Unlike the climatology, however, the shift equatorward in landfalling latitudes is not apparent (not shown). All

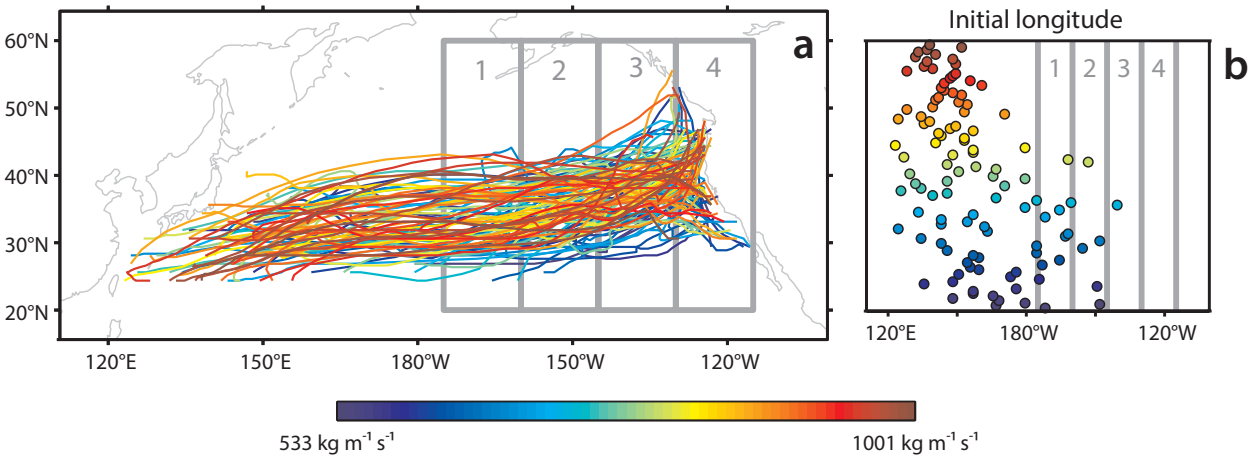

Figure 3.9: (a) Trajectories of all 112 landfalling AR cases, shaded according to lifetime intensity (as described in section 3.3.2). The grey boxes in (a) and (b) refer to the same areas and represent the regions over which composites are calculated based on AR centroid location: (1) 175°–160°W, (2) 160°–145°W, (3) 145°–130°W and (4) 130°–115°W. (b) Each point represents the longitude at which the AR is first detected.

months of the extreme subset show evidence of a strongly perturbed jet maximum and breakdown of the PV gradient in the eastern Pacific, both in association with the curvature of the moisture plume close to the surface towards the coastline (Fig. 3.8k-o). For the extreme subset of ARs (bottom row of Fig. 3.8), all months show a close relationship between the moisture plume at lower levels and the jet maximum at upper levels. This strong, yet deformed, jet is associated with increased distortion of the PV contours and anticyclonic breaking over all months. While there are no discernible changes in the strength of the high pressure center to the south of the moisture plume, the selected ARs have a much deeper low pressure center to the north.

3.4.4 Composites of selected cases over the basin

Moving away from static composites of ARs at landfall, we consider the variability of ARs over the Pacific and their development prior to landfall. Figure 3.9a shows trajectories, smoothed using a moving average filter, for all 112 ARs selected, colored according to their lifetime intensity. Figure 3.9b shows the relation of initial longitudinal locations in the extratropics relative to the four regions designated in Fig. 3.9a (the y-axis has no significance),

again, colored according to their lifetime intensity. The AR trajectories lie approximately equatorward of the storm track over the Pacific, consistent with their association with the warm sector of extratropical cyclones (based on visual comparison with Fig. 1 in *Hoskins and Valdes*, 1990; *Chang and Fu*, 2002). The strongest ARs have initial locations primarily in the western Pacific and the weakest ARs have initial locations generally located more eastwards (Fig. 3.9b).

Using the centroid information recorded for each AR, we investigate the nature of the relationship between Rossby waves in the upper troposphere and ARs in the lower troposphere. Figure 3.10 shows the composite time evolution of the 200 hPa PV field (dark grey contours), 200 hPa wind speed (red contours), SLP (light grey contours) and *MF* (shading). The red filled circle indicates the average AR centroid location for each composite. The first two frames of the figure (Figs. 3.10a-b) depict, in the PV field, the eastward propagation of the Rossby wave with the AR centroid following closely. By Fig. 3.10c, there is evidence of RWB, which becomes clearer in Fig. 3.10d in terms of the perturbed PV field. Mirroring the behavior

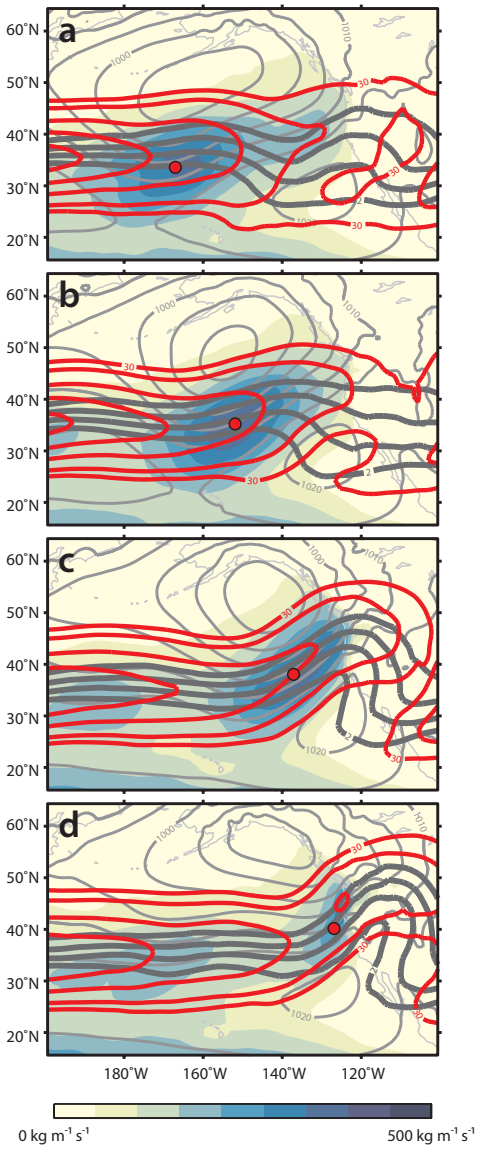

Figure 3.10: Composite SLP (light grey contour, intervals of 5 hPa), PV at 200 hPa (dark grey contour, intervals of 1 PVU), wind speed at 200 hPa (red contour, intervals of 10 m s^{-1}) and *MF* (shaded) for the 112 AR events in our extreme subset for (a) 175°–160°W, (b) 160°–145°W, (c) 145°–130°W and (d) 130°–115°W. The average location of the AR centroid is marked by a filled red dot.

of the PV field and the jet in the eastern Pacific, *MF* curves poleward just off the coast of North America (Fig. 3.10c-d).

It is important to note that Fig. 3.10 is a composite over many cases, which will lead to a smoothing out of the PV field. On a case by case basis, the ARs at landfall are typically positioned along the western edge of a breaking bay over the eastern Pacific and terminate prior to complete overturning of the PV contours. For most of the cases investigated, the resulting breaking is anticyclonic in nature, apparent in Fig. 3.10d (although diluted due to averaging). The location of breaking associated with the ARs is consistent with both the position of the ARs on the equatorward (anticyclonic) side of the jet and the winter-time RWB climatology for anticyclonic breaking over the Pacific, downstream of the jet maximum (*Strong and Magnusdottir*, 2008a).

3.5 Intensity differences in selected cases

To illustrate the dynamical differences that contribute to variations in AR intensity over the basin in greater detail, we divide our subset of extreme AR events into two groups according to average lifetime intensity. Dates with lifetime intensities exceeding the 90^{th} percentile were chosen as our top dates (11 total with values greater than 858.9 kg m^{-1} s^{-1}) and dates falling below the 10^{th} percentile were chosen as our bottom dates (11 total with values less than 612.6 kg m^{-1} s^{-1}). Composites for these two groups in the following figures are based on the position of the AR centroid, as in Fig. 3.10, with strong AR composites on the left and weak AR composites on the right.

3.5.1 Composites

Figure 3.11 shows the composited time evolution of the 200 hPa PV field (dark grey contours), 200 hPa wind speed (red contours), SLP (light grey contours) and *MF* (shading) of the 11 strongest ARs (a-d) and the 11 weakest ARs (e-h).

The progression of the strongest ARs is associated with a sustained upper-level jet, even as RWB is taking place, a deep low pressure center to the north and a well defined and

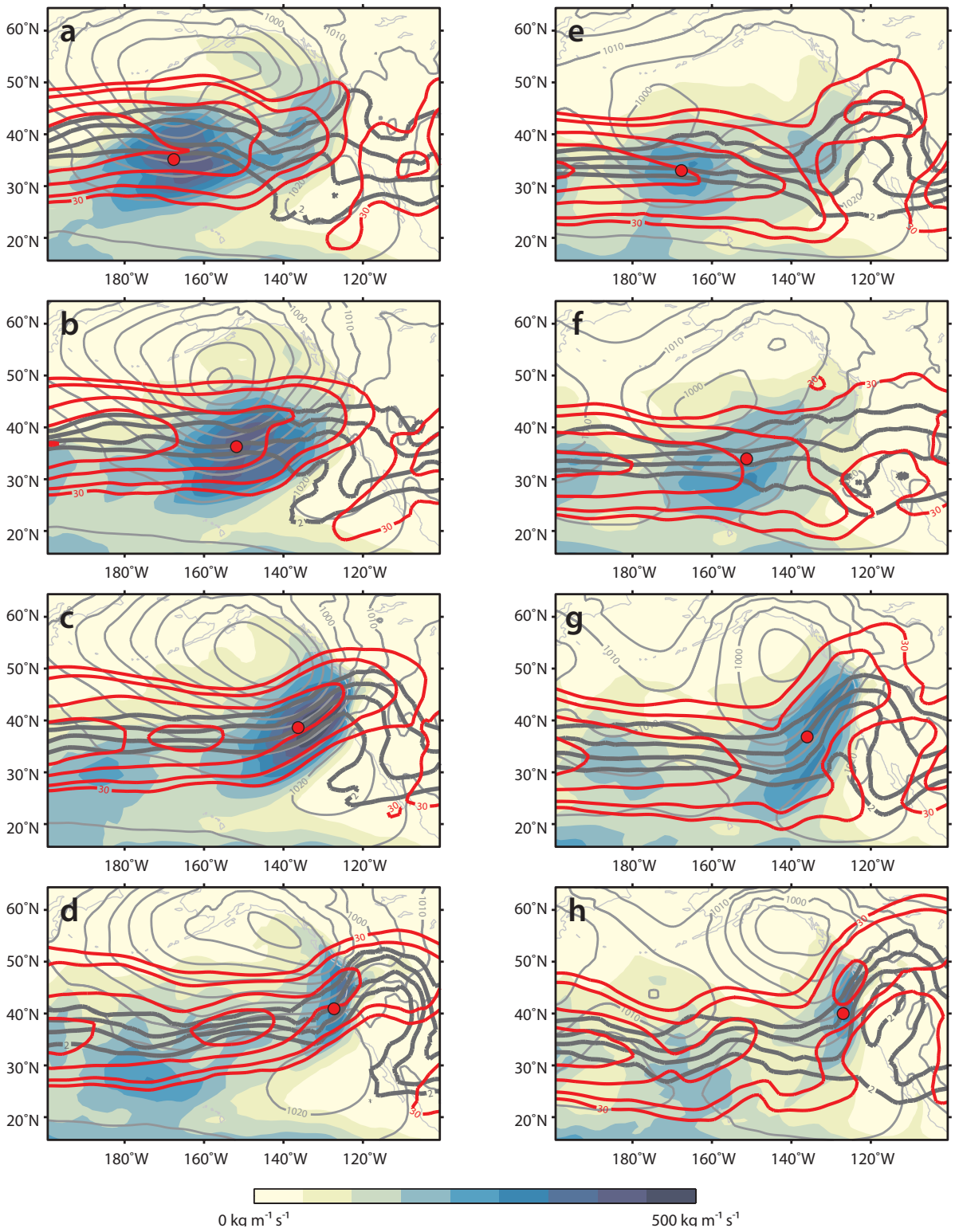

Figure 3.11: Same as Fig. 3.10, but for the (a-d) 11 strongest ARs and (e-h) 11 weakest ARs in our extreme subset for (a,e) 175°–160°W, (b,f) 160°–145°W, (c,g) 145°–130°W and (d,h) 130°–115°W. The average location of the AR centroid is marked by a filled red dot.

persistent high pressure center to the south (Fig. 3.11a-d). *MF* plumes have values in excess of 400 kg m^{-1} s^{-1} and are well supported throughout their lifetime by a strong, co-located upper level jet. Progression eastwards is associated with increased nonlinear behavior in the PV field (overturning of contours in Fig. 3.11b-d). In Fig. 3.11d, anticyclonic overturning of PV contours is apparent around 120°W and is concurrent with weakening of the AR plume.

Relative to the strongest ARs, the weakest ARs are associated with a weaker jet in the eastern Pacific, as RWB takes place, a shallower low pressure center to the north and the absence of a persistent high pressure center to the south (Fig. 3.11e-h). The associated extratropical cyclone for the strongest ARs is a much tighter system and stronger than the cyclone associated with the weakest ARs. Comparison of *MF* between the two groups shows the evolution of a much smaller and weaker AR, with values generally below 350 kg m^{-1} s^{-1}. The PV field remains relatively linear over the central Pacific with the appearance of the ARs. Same as for the strongest ARs, the weakest ARs are preceded by breaking in the eastern Pacific around 120°W. Development of nonlinear behavior in the PV field over the eastern Pacific with AR propagation is delayed and it is less coherent and not as well defined compared to features in the left column (Fig. 3.11g-h).

Both the weakest and strongest ARs are associated with the formation of anticyclonic breaking in the eastern Pacific. However, in the weakest ARs, this effect is muted in the composite, and appears later in their lifecycle (Fig. 3.11h). While ARs developing in association with linear Rossby wave propagation were observed, none had intense enough moisture transport off the coast of North America to fit into our extreme subset.

3.5.2 Rossby wave breaking

To examine the influence that each type of RWB has on AR intensity, we compare the locations and characteristics of RWB for the strongest and weakest ARs. In general, ARs are much more strongly associated with anticyclonic breaking than cyclonic breaking, especially over the eastern Pacific (i.e. Fig. 3.11). Cyclonic breaking associated with the progression of ARs over the basin and at landfall is dispersed relative to the location of the AR centroids

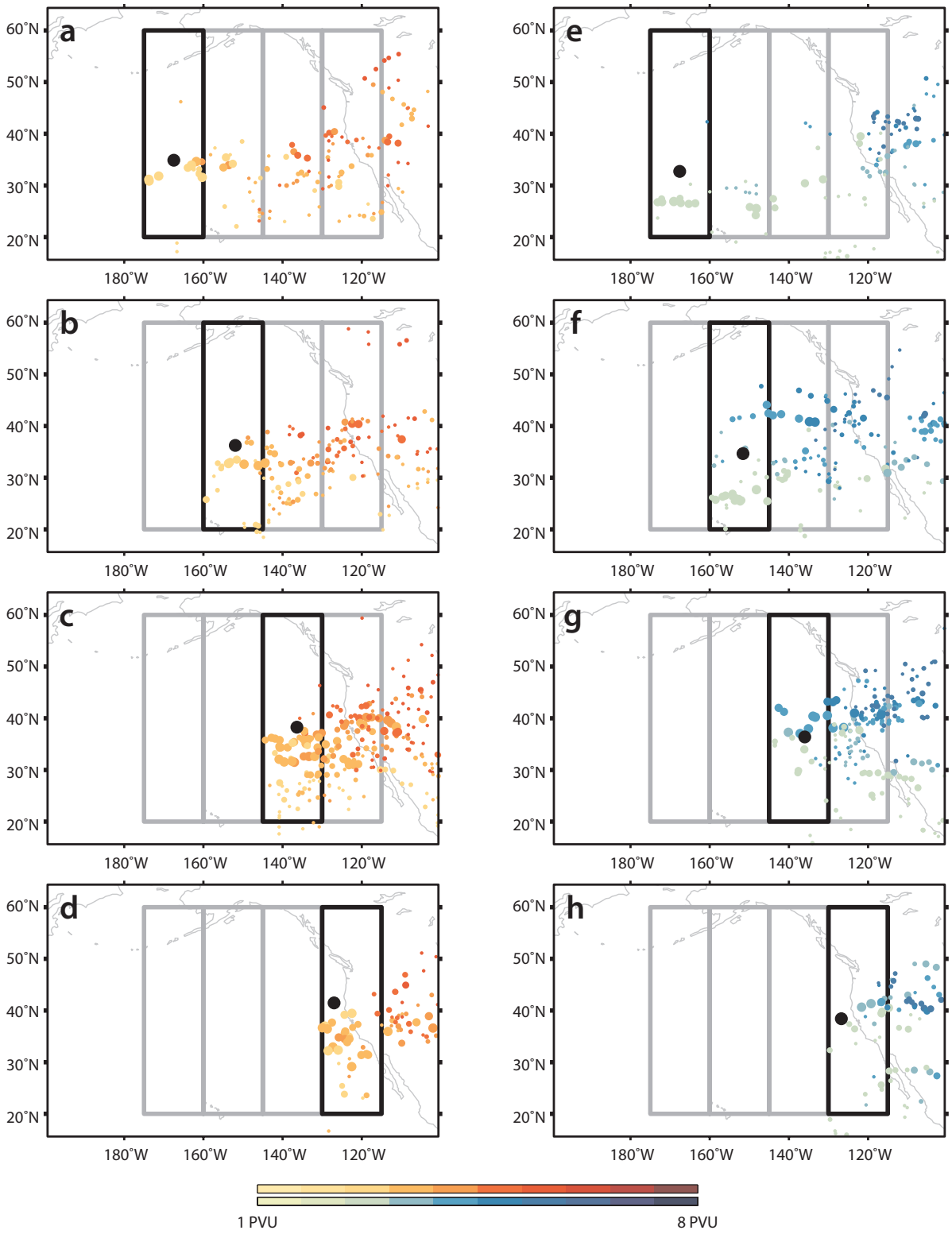

Figure 3.12: Relationship between the location of the AR (filled black dot) and anticyclonic RWB for the (a-d) 11 strongest and (e-h) 11 weakest ARs. Using the same regions as in Fig. 3.10, for each panel, the region the AR is in is outlined in black and all breaking occurring within and leading that region is plotted, where shading indicates the position of breaking (PVU) and size indicates its zonal extent.

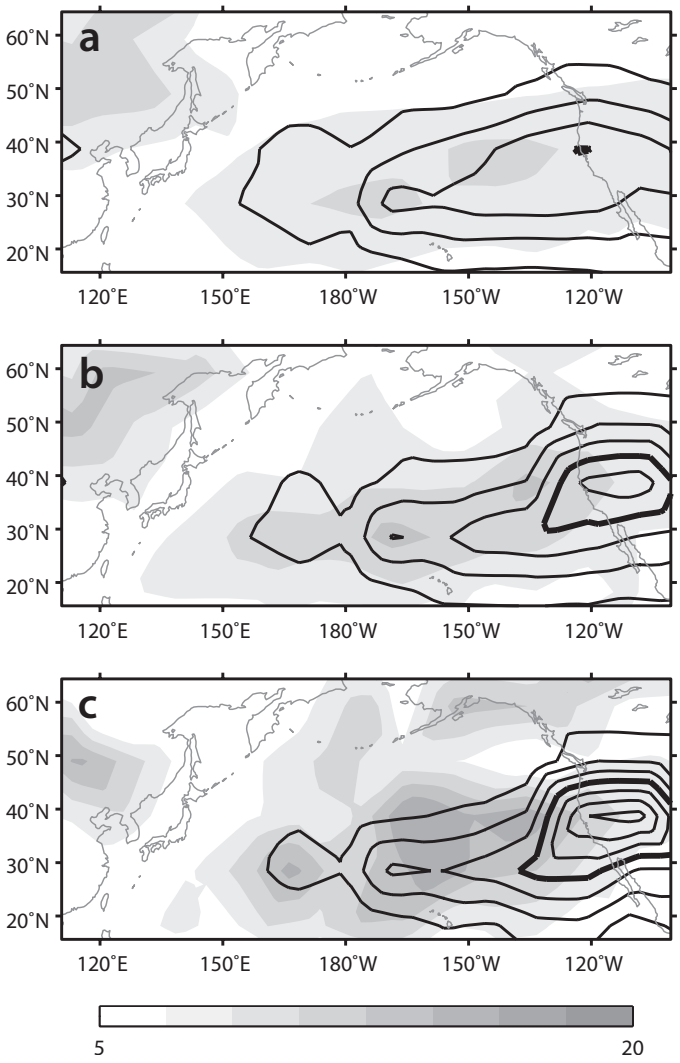

Figure 3.13: Anticyclonic RWB relative frequency, γ, (contoured, intervals of 0.05 with the 0.2 contour bolded) and average zonal extent, $\overline{L}$, (shaded, units of arc length) for (a) the climatological mean of the extended winter over the years 1979 to 2011, (b) all 749 landfalling AR dates over the extended winter over the years 1979 to 2011 and (c) the selected subset of 112 extreme landfalling AR dates.

(not shown). The weakest ARs are associated with an increase in the frequency of cyclonic RWB in the eastern Pacific relative to the strongest ARs (not shown). However, the average zonal extent of cyclonic breaking for both groups generally decrease as the ARs progress into the eastern Pacific. We focus on the influence of anticyclonic RWB on AR intensity for the remainder of this section.

To illustrate the influence of anticyclonic breaking on ARs, we investigate the breaking locations in relation to the average position of the AR centroid for the strongest and weakest ARs. Each row of Fig. 3.12 shows all anticyclonic breaking events that occur simultaneously with the centroid in the region outlined in black (both within the region and east of the region). The sizes of the colored markers are scaled according to the zonal extent of each breaking event. The shading of the markers indicates the PV contour on which overturning is detected in units of PVU. At 200 hPa, breaking is generally detected between 0.5 PVU and 8 PVU, consistent with breaking recorded for the 350 K level in *Strong and Magnusdottir* (2008a).

The strong association of ARs with anticyclonic RWB is consistent with position of ARs on the equatorward side of the jet and the location of the wintertime anticyclonic surf zone in the eastern Pacific (*Abatzoglou and Magnusdottir*, 2006; *Strong and Magnusdottir*, 2008a). For the strongest ARs, anticyclonic breaking is almost exclusively limited equatorward of the AR centroid and stays relatively concentrated as the AR moves eastward (Fig. 3.12a-d). For the weakest ARs, breaking is much more dispersed meridionally and is less concentrated (Fig. 3.12e-h). The overall frequency of anticyclonic breaking is slightly higher for the weakest ARs, however, there are no apparent trends in the frequency of breaking in each region for either the strongest or weakest ARs. The average zonal extents of the breaking events increase for the strongest ARs (from 9.3 to 10.6 arc length units) and decrease for the weakest ARs (from 10.6 to 9.1 arc length units) as the AR propagates eastwards. For the strongest ARs, anticyclonic RWB becomes more spatially concentrated equatorward of the AR centroid, as the AR approaches landfall (Fig. 3.12c-d).

3.5.3 Anticyclonic RWB characteristics of all landfalling ARs

We extend our results to the entire AR climatology and consider the frequency and extent of anticyclonic RWB for all landfalling AR dates compared to the RWB climatology for the extended winter. Figure 3.13 shows the relative frequency, γ, and average zonal extent, $\overline{L}$, for anticyclonic RWB for the climatology for the extended winter (a), all landfalling AR dates (b) and for the selected subset of extreme landfalling AR dates (c), respectively. Accounting for differences in the datasets and the use of the 200 hPa pressure surface, the general location of average zonal extent and breaking frequency are consistent with *Strong and Magnusdottir* (2008a, their Fig. 2a). Breaking events at this level are detected between 0.5 PVU and 8 PVU, again, generally consistent with the findings in *Strong and Magnusdottir* (2008a). Comparison of Figs. 3.13b-c to Fig. 3.13a shows that the maximum in anticyclonic RWB frequency is shifted eastward, over the coast, for AR dates. The strongest AR dates are associated with a substantially higher frequency of anticyclonic breaking in the eastern Pacific, located over the coastline and slightly equatorward of the relative frequency for all ARs over the time period.

3.6 Discussion and conclusions

This study uses MERRA reanalysis moisture and dynamical fields to investigate large scale features of ARs at landfall and the role of RWB in modifying their behavior and intensity over the Pacific basin prior to landfall. Landfalling ARs are identified as plume like features in *MF* that are above a threshold determined by the data and in physical proximity to the coastline of North America. We investigate the general characteristics of AR landfall over the extended winter (November through March) over more than three decades (1979 to 2011) by setting this threshold to the 85^{th} percentile of peak daily *MF* averaged over the region defined in Fig. 3.1a. For a more in-depth investigation, from this dataset of landfalling ARs, we objectively select 112 landfalling AR dates by changing the set threshold to the 95^{th} percentiles of peak daily *MF* and total daily precipitation, again, averaged over the region defined in Fig. 3.1a. The 112 AR dates include 4 significant AR storms that are well

documented in the literature. A tracking algorithm based on *MF* was developed to expand each landfalling event to its full lifetime, from its first appearance in the extratropics as a persistent feature to its termination after making landfall. Use of this tracking algorithm allows for an investigation of the characteristics of each AR, specifically intensity and the path of its centroid over time.

Approximately 15% of the dates are landfalling AR days. The largest and most intense landfalling AR days occur in November, with fewer and less intense ARs later in the season. Latitude of landfall shifts equatorward, with the poleward-most ARs occurring in November and the equatorward-most ARs occurring in March. While there are no seasonal trends in total daily precipitation, positive precipitation anomalies shift equatorward over the course of the season (not shown), in line with the seasonality of extreme precipitation events in the western United States (e.g., Fig. 3 in Ralph et al. 2014).

Composites of landfalling AR events show a close relationship between ARs, the 200 hPa PV field and the closely associated 200 hPa jet. The most noticeable difference in ARs between the different phases of ENSO is in the latitude of landfall. Most landfalling AR dates occur during El Niño, and the fewest occur during La Niña. The MJO is shown to modulate the intensity of landfalling ARs, as well as, precipitation totals.

While seasonality in the jet structure may influence the intensity of ARs prior to landfall, not all of the most intense ARs make landfall early in the season. Investigation of the upper-level characteristics of the extreme subset of dates tracked over the basin shows some common features, such as an extended strong jet and the formation of RWB in the eastern Pacific (Fig. 3.8f-j). Focusing on the behavior of the tracked ARs over the basin, the strongest ARs first appear in the extratropics in the western Pacific and their trajectories generally correspond to the equatorward side of the jet. Composites of upper-level fields following the progression of the AR eastwards over the basin, show a close relationship between Rossby wave-activity flux and moisture flux. In general, most of the ARs studied formed in association with Rossby wave propagation in the central Pacific, eventually terminating as

anticyclonic RWB took place in the east Pacific.

We focus on the dynamical differences influencing AR intensity prior to landfall by comparing the strongest dates to the weakest dates in our subset, determined based on the 90^{th} and 10^{th} percentiles of the lifetime intensity of all 112 tracked ARs, respectively. The differences in the strongest and weakest ARs are apparent in the development and extent of anticyclonic RWB in the east Pacific. The strongest ARs are associated with a well developed anticyclonic breaking 'bay' in the east Pacific, a strong, but highly perturbed, jet, a tight low pressure center to the north or northwest and a persistent high pressure center to the south or southeast. The weakest ARs are associated with less extensive RWB, that occurs later in the lifetime of the AR, a less perturbed jet, a shallower low pressure center to the north and the absence of a persistent high pressure center to the south.

What emerges from this study is the clear dominant influence of extratropical dynamics in terms of Rossby wave propagation and Rossby wave breaking over the east Pacific on the existence of landfalling West Coast ARs. ARs are associated with strong anticyclonic RWB over the east Pacific. This is a dynamically robust region of the world where anticyclonic RWB has been shown to lead to a positive polarity of the North Atlantic Oscillation far downstream (*Strong and Magnusdottir*, 2008b).

Our results present a physical link between the large-scale climate patterns and ARs over the North Pacific. Previous studies have alluded to a connection between climate patterns and ARs based on correlations between signatures of ARs on land and climate pattern indices. The physical link is the process of RWB that takes place on a similar time scale as the AR lifetime. We have shown a direct link between RWB and ARs. Thus we conclude that the way in which ARs are modulated by extratropical climate patterns is driven by the interaction of these climate patterns with RWB (*Strong and Magnusdottir*, 2008b; *Rivière*, 2010).

Acknowledgments

We thank the two anonymous reviewers who contributed valuable comments and suggestions to improve the manuscript. This work is supported by NSF grant AGS-1206120 and NSF GRF under grant DGE-1321846.

Chapter 4

Development of persistent landfalling atmospheric rivers over the eastern North Pacific

Abstract

Landfalling atmospheric rivers (ARs) are linked to heavy precipitation and extreme flooding, most notably along the western coast of North America. The duration and magnitude of landfalling ARs are correlated to their hydrological impacts on land. The forecast of these hydrologically significant landfalling events can be improved through a better understanding of the mechanisms leading to their formation and evolution prior to landfall.

A subset of persistent landfalling AR events is identified in 3-hrly MERRA reanalysis and validated against observational datasets. These events are identified as lower tropospheric wind and moisture features with extended geometry that persist over the coastline for longer than two days. A composite analysis of persistent landfalling events shows an eastward extended, perturbed upper-level jet and anticyclonic overturning of potential vorticity contours, indicating anticyclonic Rossby wave breaking. The association of persistent circulation anomalies with long-duration ARs is investigated using weather regime analysis. Three weather regimes identified using K-means clustering of daily anomalies of the 700 hPa geopotential height field. Only one of the three regimes is found to be associated with anomalously enhanced moisture transport and contains the highest frequency of AR occurrence. Slight differences are found between persistent and all AR events within this regime.

4.1 Introduction

Atmospheric rivers (ARs) are synoptic scale, filamentary features with high water vapor content in the lower troposphere that have also been shown to play an important role in the regional hydrology of the western coastline of North America. Their interaction with topography and inland extension have been linked to extreme precipitation and flooding (*Ralph et al.*, 2005, 2006; *Dettinger*, 2011; *Ralph and Dettinger*, 2012). However, despite their extreme nature, ARs have also been shown to be an important source of water to the region, providing up to 50% of total water resources (*Guan et al.*, 2010; *Dettinger*, 2011). Improved forecasts of the intensity and potential impacts of landfalling events to water resources is therefore essential to the region.

Landfalling AR events vary greatly in duration and intensity. Variability in these characteristics contribute to the large interannual variability in total precipitation found over the region (*Dettinger et al.*, 2011; *Ralph and Dettinger*, 2012). Along with precursor soil moisture conditions, the duration and magnitude of landfalling AR events are strongly associated with their hydrological impacts (*Ralph et al.*, 2013; *Moore et al.*, 2012). In particular, ARs with sustained and persistent moisture transport are connected to heavy precipitation on land. *Moore et al.* (2012) documented the role of a persistent AR that contributed heavy rainfall and flooding over central Tennessee and Kentucky over a two day period in May 2010. They attributed the development of two quasi-stationary mesoscale convection systems to the near constant presence of an AR over the region. *Ralph et al.* (2013) investigated the hydrological characteristics of landfalling events over a six year period, using station-based observations near the Russian River basin in California. While the average duration of events passing over this region were 20 hours, persistent events in excess of 30 hours were observed. Little has been done to investigate the mechanisms contributing to the development of persistent ARs at the large-scale over the North Pacific (e.g. *Ramos et al.*, 2015). The forecast of these hydrologically significant landfalling events can be improved through a better understanding of the mechanisms leading to their formation and evolution

prior to landfall, a point that has not been sufficiently explored in the current literature.

Large-scale influences on precipitation over western North America have been extensively investigated in the literature. Strong evidence for the role of teleconnection patterns in the modulation of precipitation and snowpack exists for the El Niño – Southern Oscillation (ENSO ; *Ropelewski and Halpert*, 1987; *Dettinger et al.*, 1998; *Mo and Higgins*, 1998a,b; *Higgins et al.*, 2000, 2007; *Cayan and Redmond*, 1994), the Madden-Julian Oscillation (MJO; *Guan et al.*, 2010, 2012), the Northern Annular Mode (NAM; also referred to as the Arctic Oscillation or AO in the literature; *Higgins et al.*, 2007; *McAfee and Russell*, 2008; *Guan et al.*, 2013), and the Pacific-North American pattern (PNA; *Cayan*, 1996; *Guan et al.*, 2013). These patterns of variability are important on seasonal and interannual timescales. Against this slowly-varying climate framework, we investigate the question of variation in the duration of landfalling ARs. To do this, we focus on dominant patterns of persistence in atmospheric flow, known as weather regimes. The timescales of these weather regimes vary from a few days and up to two weeks (*Legras and Ghil*, 1985; *Reinhold and Pierrehumbert*, 1982; *Robertson and Ghil*, 1999). These persistent weather patterns have been connected to both temperature (*Michelangeli et al.*, 1995; *Carrera et al.*, 2004) and precipitation (*Ely et al.*, 1994; *Robertson and Ghil*, 1999; *Ramos et al.*, 2014; *Carrera et al.*, 2004) anomalies over North America and Europe.

Our aim is to investigate the characteristics of persistent AR events over the North Pacific. Here, we address two main questions: (1) How are these events different from 'normal' AR conditions? and (2) Are the upper-level characteristics of these events uniquely associated with intense wintertime moisture transport? Our data and methods are described in section 4.2. A description of the dataset of landfalling events used in this investigation and a composite analysis of persistent AR events are shown in sections 4.3.1 and 4.3.2. Weather regime analysis and the association of persistent atmospheric patterns with anomalous moisture transport are shown in section 4.3.3. This chapter finishes with a brief summary and a discussion of future work on this topic.

4.2 Data and Methods

4.2.1 Data

We use the Modern-Era Retrospective Analysis for Research and Applications (MERRA) reanalysis dataset, available from 1979 to 2014 (*Rienecker et al.*, 2011). Geopotential height (Z), sea level pressure (SLP) and potential vorticity (PV) are retrieved from pressure levels at reduced spatial resolution ($1.25° \times 1.25°$) at 3-hrly intervals. Derived variables, the magnitude of vertically integrated moisture flux MF and integrated precipitable water PW, are calculated as in Chapter 2. Total precipitation is retrieved at native spatial resolution ($2/3° \times 1/2°$) at 1-hrly intervals. Precipitation data is converted from units of kg m^{-2} s to units of mm hr^{-1} and the cumulative 3-hr precipitation total is calculated. The precipitation data at 3-hrly intervals is linearly interpolated to reduced spatial resolution for use with moisture and dynamical fields.

Large-scale climate patterns, such as the El Niño - Southern Oscillation (ENSO), the Madden-Julian Oscillation (MJO; *Madden and Julian*, 1972), the Northern Annular Mode (NAM) and the Pacific-North American (PNA) teleconnection pattern have all been shown to influence climate variability across western North America. As in Chapter 3, we use the monthly Multivariate ENSO Index (MEI) and the daily Real-time Multivariate MJO (RMM) index to quantify variations in ENSO and the MJO, respectively (*Wheeler and Hendon*, 2004; *Wolter and Timlin*, 1998). Only MJO phases with RMM amplitudes greater than 1 are considered in our analysis (for the purpose of removing weak MJO signals). The NAM and PNA patterns are quantified using their respective monthly indices, available through NOAA's Climate Prediction Center.

4.2.2 Identification of AR conditions and event clustering

As in *Payne and Magnusdottir* (2014, 2015), we focus on wintertime landfalling ARs (October through March), defined by their physical proximity to the western coastline of North America. Conditions along a single grid-point wide transect following the coastline are recorded using MERRA reanalysis (25°N to 60°N, Oct - Mar, 1979 - 2014). A set of criteria

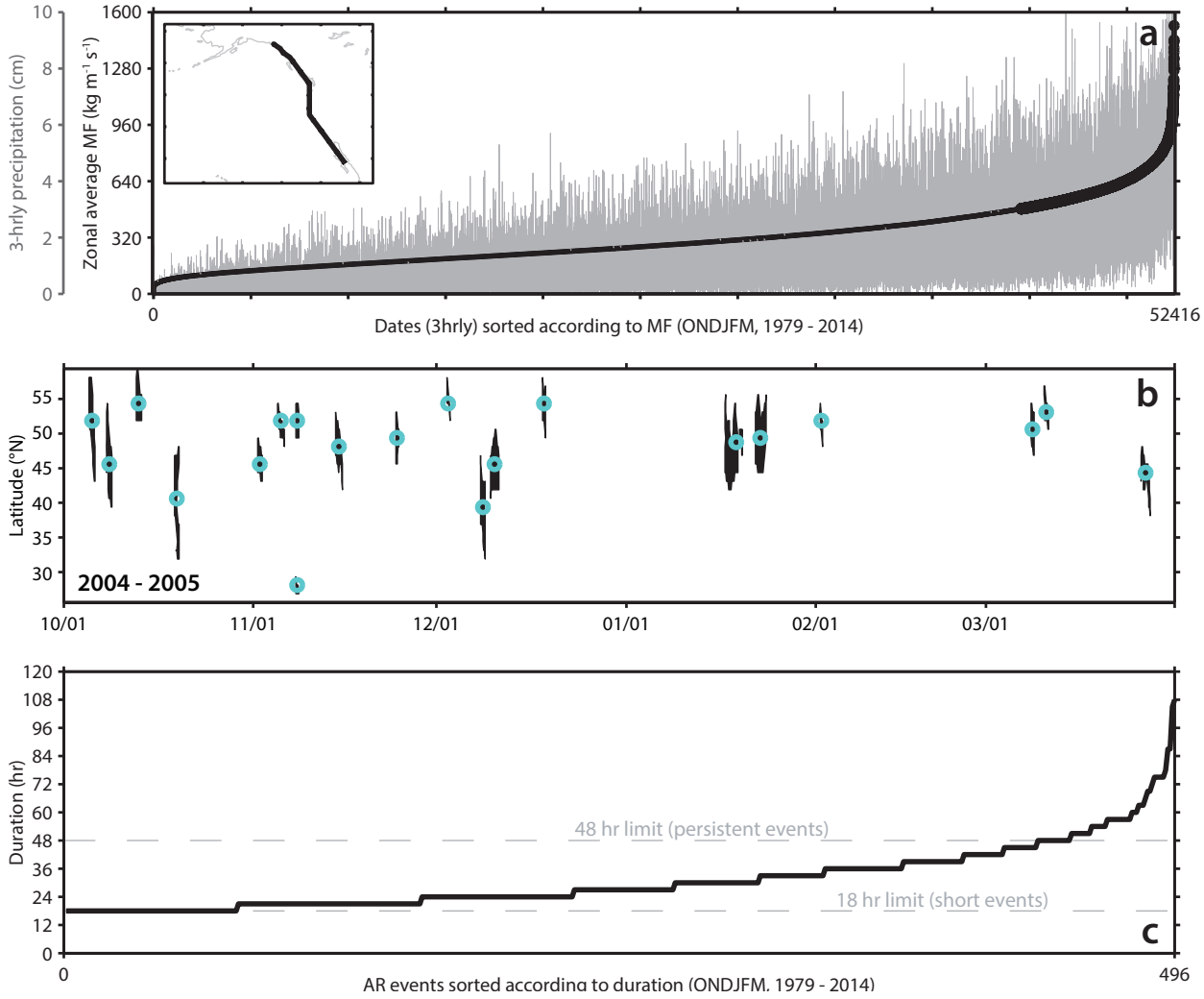

Figure 4.1: Using MERRA reanalysis, (a) all 3-hrly timesteps in the winter season (OND-JFM, 1979 - 2014) sorted according to the magnitude of integrated moisture transport (MF, black line) as detected along the West Coast. Associated precipitation totals for each timestep are shown in grey. Identified AR conditions are shown as filled black circles. (b) As an example, identified AR events for the 2004 - 2005 winter season, with the median land-falling latitude marked as a teal open circle. (c) All identified AR *events* sorted according to duration, with long duration events falling above the 48-hr limit.

based on observational studies are used to identify AR conditions at each 3-hrly timestep: (1) MF $\geq$ 85th percentile (*Lavers et al.*, 2012), (2) PW $\geq$ 2 cm (*Ralph et al.*, 2004, 2005; *Neiman et al.*, 2008a), and (3) 850 hPa wind speed $\geq$ 10 m s^{-1} (*Ralph et al.*, 2004, 2005).

The transect used to record conditions is shown in the insert of Fig. 4.1a and differs slightly from the method in *Payne and Magnusdottir* (2014) as we only consider a single gridpoint for each latitude for the region hugging the coastline. Since the purpose of this research is to look at duration of each landfalling event rather than general characteristics, averaging over a zonal section as in *Payne and Magnusdottir* (2014) may introduce uncertainty in the duration of the event by smoothing out its initiation or termination. Figure 4.1a shows the distribution of all timesteps considered, sorted according to MF (black line) with associated cumulative 3-hrly precipitation (grey line). The timesteps identified as having AR conditions are marked by a filled black circle.

Timesteps that are identified as having AR conditions are clustered in time into distinct landfalling events by grouping temporally and spatially consistent MF and PW. In order to ensure the feature fits the definition of an AR, we require that it exceeds 2000 km in length at least once in its lifetime (e.g. *Lavers et al.*, 2012). To reduce false identification, AR conditions must persist along the coastline for longer than 18 hours (e.g. *Ramos et al.*, 2015) and the latitude at which the feature intersects the coastline must be consistent with adjacent timesteps. As an example, Fig. 4.1b shows the latitudinal position (y-axis) and duration (x-axis) of identified landfalling events for the 2004 - 2005 winter season. The average latitudinal position of each event is shown as an open teal circle. Figure 4.1c shows all AR events identified (479 total), where long-duration events are defined as those persisting over the coastline for more than 48 hours.

This method does not take into account those ARs making landfall along the southern coastline of Alaska north of 60°N, which may be important for moisture transport to high latitudes (e.g. *Liu and Barnes*, 2015), nor does it consider short duration events persisting for less than 18 hours along the coastline.

4.2.3 Weather regime analysis

Weather regimes for the North Pacific sector are calculated for all days within the winter seasons for the 36 year period under investigation (October - March, 1979 - 2014) using daily anomalies of the 700 hPa geopotential height field (Z700). Anomalies are calculated using the daily climatology for each date between October 1979 and March 2015. Following the methods in *Yiou et al.* (2007), in order to isolate the dominant atmospheric patterns, the leading 15 Empirical Orthogonal Functions (EOFs) and Principal Components (PCs) for the North Pacific sector (20°N to 80°N, 130°E to 120°W) are calculated using Z700 anomalies. A K-means clustering algorithm based on *Michelangeli et al.* (1995) is applied to the PCs to categorize each day within the period of interest to one of four centroids according to a spatial correlation coefficient ($r > 0.25$). In-line with our definition of a persistent AR, only days with regimes lasting at minimum two days are considered.

For simplicity, we consider only three weather regimes following the example in **?**. However, there is some disagreement on the number of robust regimes for the North Pacific sector (e.g. *Smyth et al.*, 1999). Work in *Robertson and Ghil* (1999) identified six regimes for the North Pacific sector. They determined that these six regimes were a subset of the ones identified in *Michelangeli et al.* (1995).

4.2.4 Statistical significance

Statistical significance throughout the chapter is assessed using a two-sample Student's t-test at the 95% significance level. In composite maps, significance is indicated by grey stippling.

4.3 Results

Our results are divided into three parts. First we discuss characteristics of the persistent landfalling event dataset, then we investigate whether persistent ARs show unique characteristics compared to the climatology of all AR events identified. Finally, we approach our research questions from a different angle and investigate whether the upper-level characteristics identified for persistent events are uniquely associated with high moisture transport

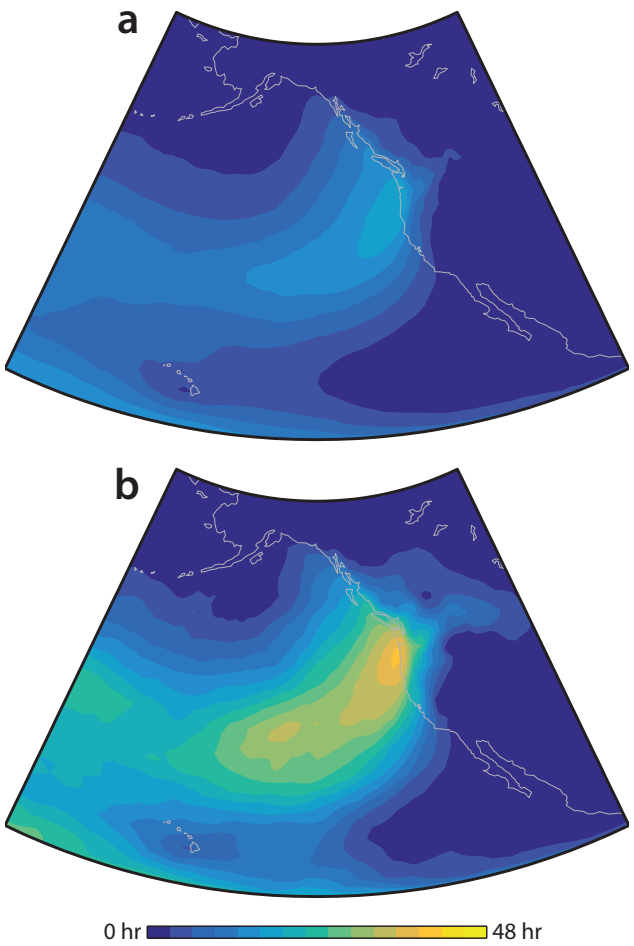

Figure 4.2: Comparison of average duration of (a) all ARs to (b) persistent ARs. Calculated as the average number of timesteps with $MF \geq 250$ kg m^{-1} s^{-1}.

using weather regime analysis.

4.3.1 Overview of dataset

Over the 36 year period considered in this investigation, 7042 3-hrly time-steps were identified as having landfalling conditions ($MF \geq$ 85th percentile, $PW \geq 2$ cm, 850 hPa wind speed ≥ 10 m s^{-1}). These timesteps are clustered into 496 landfalling events, for an average of 13 events identified over each 6 month half-year. From this dataset, 62 events were identified as persisting for longer than 48 hours.

Many AR identification schemes exist in the literature (see discussion in Chapter 2; e.g. *Lavers et al.*, 2012; *Guan and Waliser*, 2015). However, few can be applied to an analysis

of AR duration. Outside of case studies, identification schemes generally identify time-steps with AR conditions rather than multi-timestep events. To place our results in context, we compare our dataset of landfalling AR events against existing records. Our dataset shows excellent agreement with the reanalysis-based dataset used in *Guan and Waliser* (2015), with 92% overlap (97% with a ± 2 day buffer). Our dataset is in general agreement with 56% overlap with older records that use satellite-derived humidity observations (no wind) to identify landfalling events in total column precipitable water (*Neiman et al.*, 2008a). However, agreement increases to 98% with a ± 2 day buffer. All notable landfalling events singled out in the literature are captured by our dataset (e.g. *Leung and Qian*, 2009; *Galewsky and Sobel*, 2005; *Ralph et al.*, 2003, 2006, 2011; *Smith et al.*, 2010; *Neiman et al.*, 2008b, 2011).

Consistent with a similar analysis in *Ramos et al.* (2015) and with findings in *Ralph et al.* (2013), the majority of the AR events identified persist between approximately 24- to 36-hours with only a few persisting longer than 48 hours. We show average duration of AR conditions (calculated as $MF \geq 250$ kg m^{-1} s^{-1}) over all AR events in our dataset compared to those in the persistent AR subset in Fig. 4.2, following the measure used in *Rutz et al.* (2014). Consistent with their findings, the landfalling ARs are most present along the coastline of the Pacific Northwest. The maximum duration averaged over all AR events is 26 hours. The average duration decreases to approximately 2 hours at lower latitudes, again, consistent with *Rutz et al.* (2014, their Figure 1a). Comparison of the average duration of all ARs to the average duration of the subset of persistent ARs shows a large increase (Fig. 4.2b). While the spatial structure between the two panels is similar, the maximum averaged duration for the persistent ARs is 50 hours. The in-land extension of AR conditions is more pronounced in this subset. The agreement of this dataset with established records and the clear difference in average duration between persistent and all AR events supports its use for an investigation of variability in the timing of landfalling events.

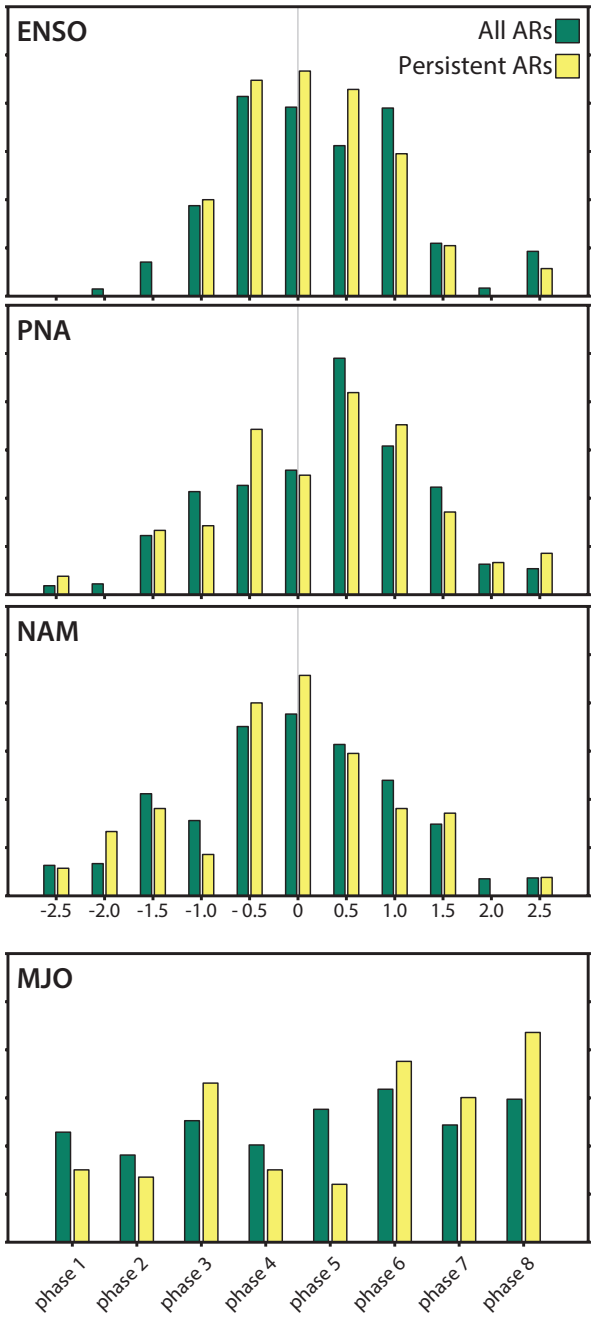

Figure 4.3: Normalized comparison of persistent ARs (yellow) to all ARs (green) for ENSO, PNA, NAM and the MJO.

4.3.2 Are persistent events different?

Results in Chapter 3 highlight the importance of large-scale climate patterns on the behavior of landfalling ARs. The purpose of this section is to determine whether persistent landfalling events are uniquely different from all landfalling events. We start with an investigation of the relationship between AR duration and large-scale patterns of variability and finish with a composite analysis of the differences between persistent ARs and all AR events in relevant dynamical and moisture fields.

Large-scale patterns

Figure 4.3 shows the normalized distribution of persistent ARs (in yellow) compared against all ARs (in green) categorized according to the indices of ENSO, the PNA pattern, the NAM and the MJO (for RMM amplitudes greater than 1). Among the four modes of variability, the largest difference between the two datasets occurs in association with the eastward propagation of the MJO. Persistent AR events are more frequent during MJO phases 3, 6, 7 and 8. The increased frequency found in phases 3 and 6 is consistent with work in *Guan et al.* (2012), which showed MJO modulation of the Sierra Nevada snowpack, and in phases 7 and 8 is consistent with work in *Payne and Magnusdottir* (2014). They showed these phases to be associated with a strong equatorward-shifted zonal wind anomalies and positive *MF* anomalies. As the *Guan et al.* (2012) study focused on a limited region over the Sierra Nevadas, the reduction in snowpack in phases 7 and 8 may be a function of variations in AR characteristics and landfalling location.

Among the remaining three modes of variability, while there are no significant differences between persistent and all ARs, the identified events as a whole show patterns consistent with previous work. *Guan et al.* (2013) showed weakened *MF* in association with La Niña conditions and strengthened *MF* in association with El Niño conditions. The relationship between ARs and ENSO was further explored in *Payne and Magnusdottir* (2014). They found that the highest number of AR conditions occur during El Niño and the fewest during La Niña, roughly consistent with what is seen in Fig. 4.3. Furthermore, the higher frequency

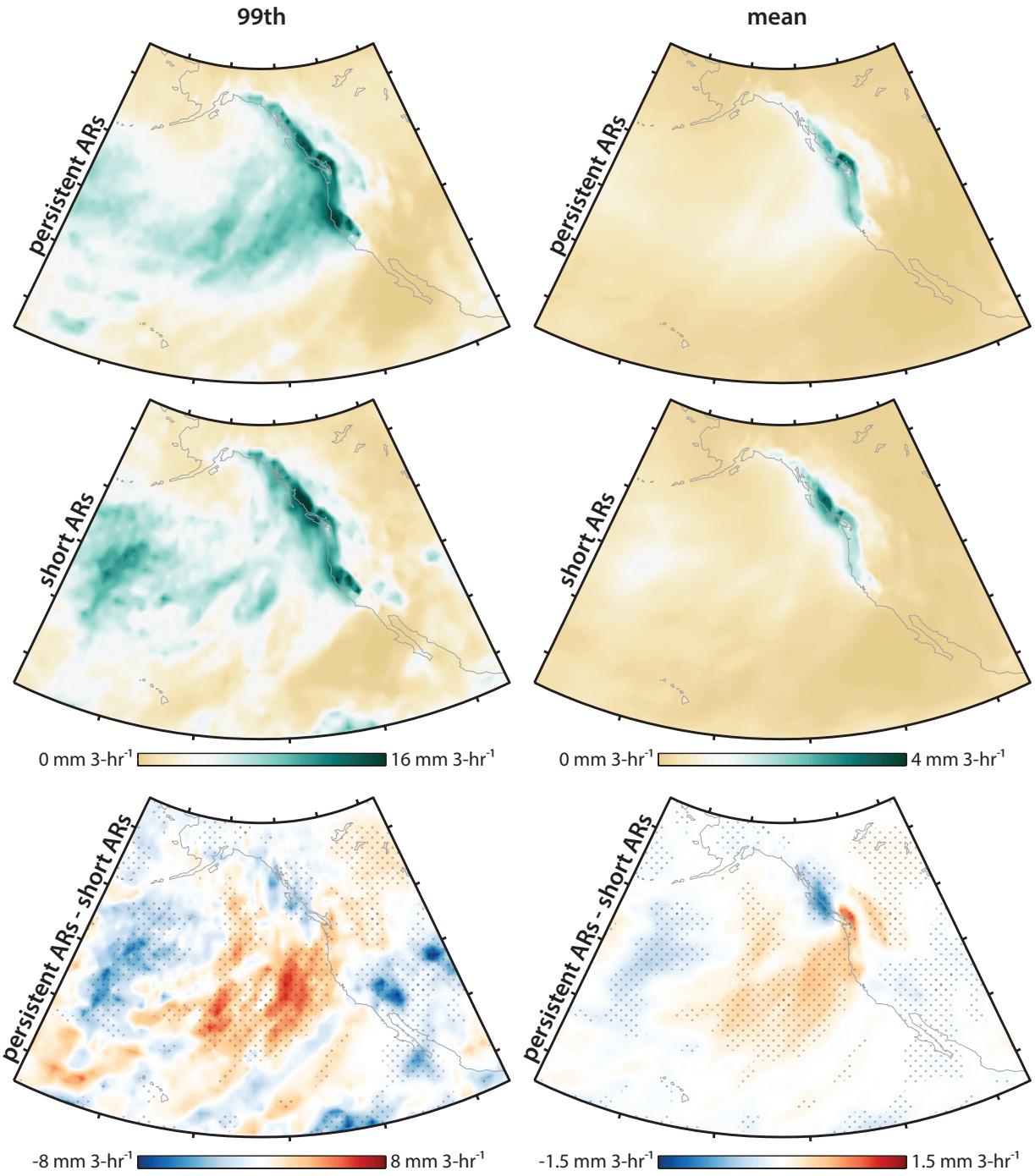

Figure 4.4: Comparison of the (left column) 99th percentile and (right column (mean) precipitation for (top row) persistent ARs compared to (middle row) short ARs (lasting shorter than 18 hours) and (bottom row) their difference. Grey stippling shows statistical significance at the 95% level.

of positive PNA and negative NAM ARs is consistent with stronger moisture transport over the basin as shown in *Guan et al.* (2013). A slightly higher number of persistent events are found during negative NAM conditions, consistent with results in *Guan et al.* (2013). However, unlike in *Guan et al.* (2013), we do not find the same relationship between the negative NAM and PNA.

Hydrological importance

To investigate whether the persistent events isolated in our subset are associated with significant precipitation events, we compare both the 99^{th} percentile and mean precipitation totals over the region between persistent ARs (lasting longer than 48 hours) and transient ARs (lasting shorter than 18 hours) in Fig. 4.4. The number of events described by these two subsets are approximately equal, with 62 persistent events and 77 short events (compare dashed lines in Fig. 4.1c).

For both datasets, precipitation is concentrated over the coastal mountains along the Pacific Northwest, consistent with findings in *Rutz et al.* (2014). Persistent AR events show higher precipitation rates at both the 99^{th} percentile level and against the mean over all timesteps. The relationship between persistent events and heavy precipitation remains when compared against all AR events (not shown).

Composite analysis

In order to summarize the differences between persistent events and all ARs, we investigate differences in composites of SLP, *MF*, *PW* and 350 K PV (Fig. 4.5). Persistent events are associated with a broad, deep low pressure anomaly slightly equatorward of mean location of the the Aleutian Low (Fig. 4.5a). Consistent with this cyclonic circulation anomaly, extensive positive anomalies in *PW* and *MF* extend from near Hawaii to the northeast over the Pacific Northwest (Figs. 4.5b and 4.5c). Upper-level PV shows an extensive negative anomaly centered over the western United States, with a positive anomaly over the Pacific, a signature of consistent with the development of anticyclonic Rossby wave breaking inland

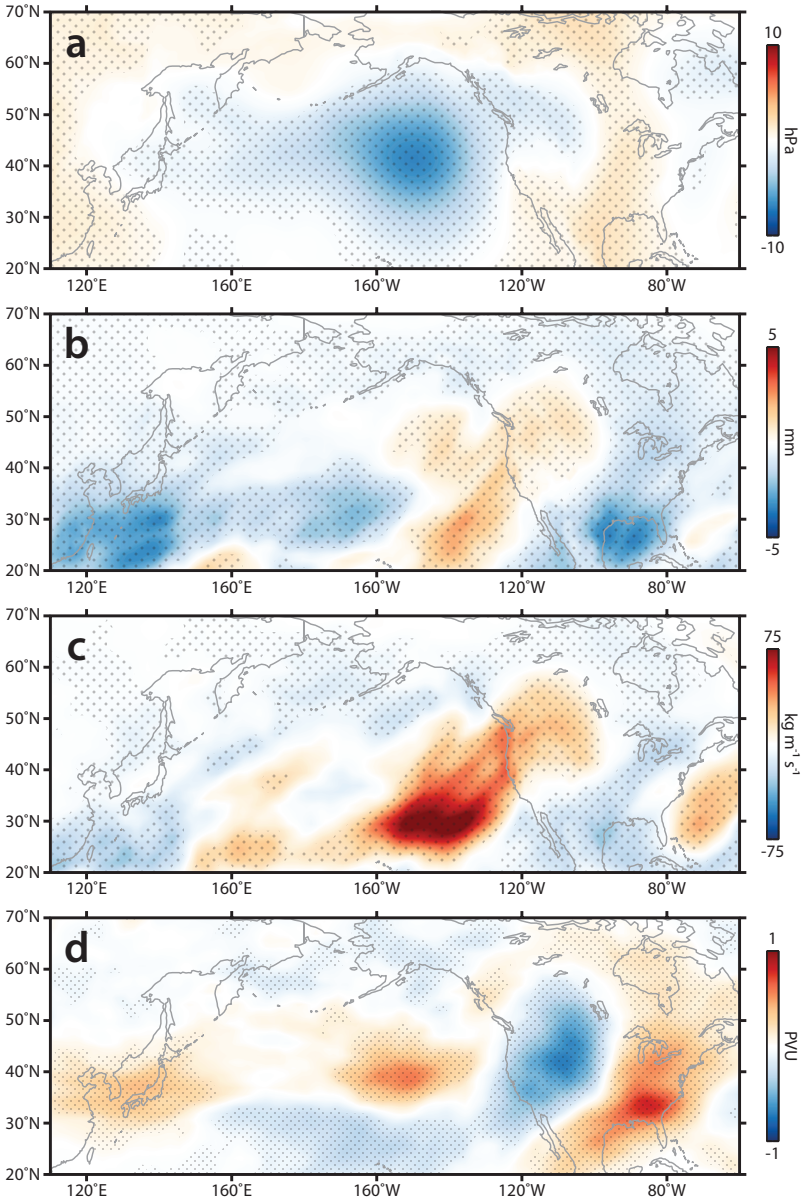

Figure 4.5: The difference between persistent AR events and the climatology of all AR events for (a) SLP (hPa), (b) PW (mm), (c) MF (kg m^{-1} s^{-1}) and (d) 350 K PV (PVU). Grey stippling shows statistical significance at the 95% level.

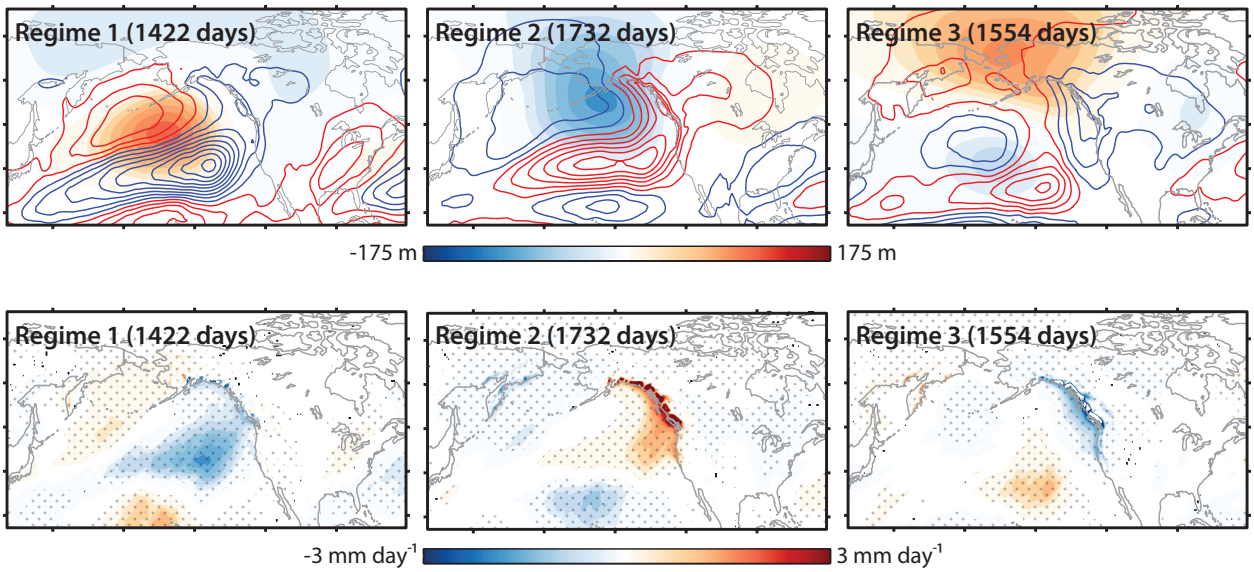

Figure 4.6: (top row) Composites of daily anomalies of Z700 (shading) and *MF* (contour, starting from 5 kg m^{-1} s^{-1} in intervals of 10, red is positive and blue is negative) for each of the regimes identified using the clustering algorithm. The total number of days (out of ONDJFM, 1979 - 2014) categorized into each regime is shown in the upper left of each panel. Only statistically significant Z700 anomalies are shown. (bottom row) Composites of daily anomalies of precipitation categorized into each regime. Grey stippling shows statistical significance of Z700 anomalies at the 95% level.

from the coastal region. This finding is in agreement with the strong association between ARs and anticyclonic Rossby wave breaking identified in *Payne and Magnusdottir* (2014). However, this negative anomaly is shifted eastward relative to the breaking pattern found in Fig. 3.13.

4.3.3 Are large-scale characteristics unique?

Here, we shift our focus from AR events to persistent weather regimes over all dates in the winter half-year for the years 1979 to 2014. The purpose of this section is to determine whether persistent circulation anomalies can explain the differences between persistent and all AR events. We use the K-means algorithm described in section 4.2 to classify daily Z700 anomalies over all timesteps into three weather regimes. Of the 6552 days in the entire time period, only 4708 are included in each composite as they meet the criteria for the persistence of the weather regime ($\geq$ 2 days) and spatial correlation ($r > 0.25$). The top row of Fig. 4.6

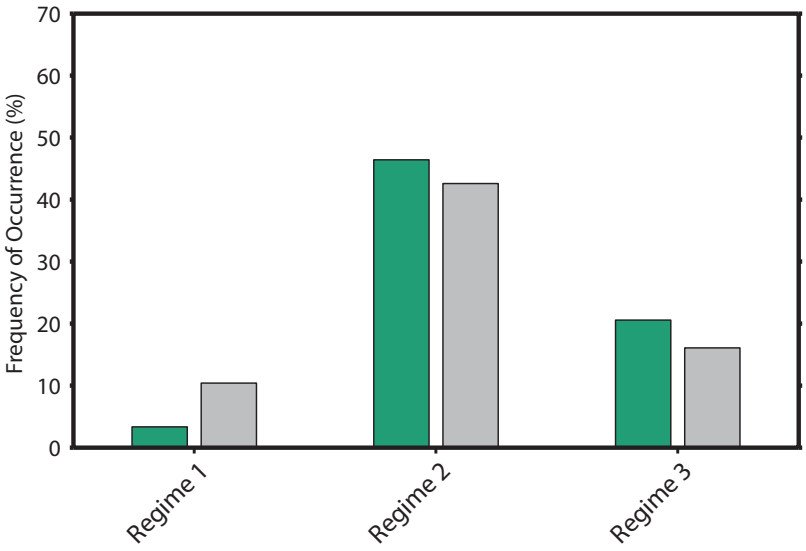

Figure 4.7: Frequency of occurrence of AR events during each regime for (grey) all ARs and (green) persistent ARs.

shows composite Z700 and *MF* anomalies for each weather regime. The three regimes shown are consistent with the findings in *Kimoto and Ghil* (1993, KG93), *Michelangeli et al.* (1995, MVL95) and *Robertson and Ghil* (1999, RG99). The three regimes are (1) a reverse PNA-like pattern (regime 2 in KG93, regime 3 in MVL95, and regime 4 in RG99), (2) a PNA-like pattern (regime 1 in KG93, regime 2 in MVL95, and regime 2 in RG99), and (3) a blocking-type pattern (regime 6 in KG93, regime 3 in MVL95 and regime 5 in RG99). The total number of days included in each composite is shown in the upper left of each panel

The three weather regimes are associated with varying circulation and moisture transport anomalies. Positive *MF* anomalies are found along the coastline only in weather regime 2. This pattern is characterized by a deep trough over the mean position of the Aleutian low and a weak ridge over central North America. The positive *MF* anomalies are associated with positive precipitation anomalies along the coastline of the Pacific Northwest and western Canada (bottom row of Fig. 4.6), consistent with results in *Pandey et al.* (1999) for precipitation over the northern Sierra Nevadas. Weather regimes 3 shows negative precipitation anomalies the Pacific Northwest, but little change in the southern portion of the domain. This is roughly consistent with work in *Carrera et al.* (2004). They showed an

increased frequency of heavy precipitation days in the Southwest and Intermountain West of the United States associated with the development of blocking over Alaska (consistent with our regime 3).

The differences between the three weather regimes are highlighted when we focus on the normalized frequency of occurrence of both persistent and all AR events for each regime (Fig. 4.7). In agreement with the strongly positive *MF* along the coastline, ARs are dominantly associated with the the PNA-like weather regime, with a slightly higher number associated with persistent events. Weather regime 3 has the second highest percentage, with a larger difference between the two datasets. The differences between weather regimes 2 and 3 may be related to different controlling mechanisms for ARs impacting the northern and southern ends of the region under investigation.

The three weather regimes described here follow the approach in *Michelangeli et al.* (1995), who argued that a higher number of regimes over the North Pacific might be the result of an unstable solution. This point was further discussed in *Smyth et al.* (1999). They used a mixture model to identify a conservative number of stable weather regimes for the Northern Hemisphere, finding two to be the most stable consisting of PNA-like and reverse PNA-like patterns. The larger number of regimes reported in (*Robertson and Ghil*, 1999) and in (*Kimoto and Ghil*, 1993) were found to be subsets of more stable solutions. Despite this, (*Robertson and Ghil*, 1999) argues that limiting the number of regimes may mask important physical relationships. The small differences between persistent ARs and all ARs seen for weather regimes 2 and 3 argue for a detailed investigation of whether a larger number of weather regimes might allow for further differentiation of the two datasets.

4.4 Conclusions

Here, we use a unique dataset to investigate the duration of AR events and to quantify differences between persistent ARs and the climatology of all ARs. The dataset used in this research shows excellent agreement with existing records of landfalling events. Comparison of the average duration of each AR event to the average duration of persistent events shows

that long-duration events do show persistence along the coastline.

Our results highlight the large-scale differences of persistent AR events. Composite analysis of dynamical and moisture fields show significant differences in SLP, PW, MF and 350 K PV. The association between ARs and anticyclonic Rossby wave breaking shown in Chapter 3 persists for persistent events, but is shifted inland over western North America.

Three weather regimes are isolated for the North Pacific sector following the methodology of *Michelangeli et al.* (1995). The highest frequency of AR occurrence is found for a PNA-like weather regime, which shows a deep trough centered near the mean position of the Aleutian Low and positive MF along the coastline. A composite of precipitation anomalies for this regime are positive, consistent with MF. While there is a slightly higher frequency of persistent events for this regime, the difference is not significant. A second regime, the blocking-type pattern, may be associated with impacts to the southern part of the domain. Total frequency for this second regime is less than the PNA-like pattern, but show a larger difference between persistent ARs and all ARs. These results motivate future work to look at the effect of increasing the total number of regimes.

Chapter 5

An evaluation of atmospheric rivers over the North Pacific in CMIP5 and their response to warming under RCP 8.5

As appears in:

Payne, A. E. and G. Magnusdottir (2015), An evaluation of atmospheric rivers over the North Pacific in CMIP5 and their response to warming under RCP 8.5, *Journal of Geophysical Research Atmospheres*, **120**, 11,173 - 11,190, doi: 10.1002/2015JD023586.

Abstract

Landfalling atmospheric rivers over the North Pacific are evaluated in historical (1980 - 2005) simulations from 28 models participating in the fifth phase of the Coupled Model Intercomparison Project (CMIP5) and compared to the MERRA and ERA-Interim reanalyses. Landfalling dates are identified as having spatially elongated high wind and moisture features in physical proximity to the coastline. Model performance relative to reanalysis is found to be quite variable. The majority can resolve the spatial structure of landfalling events, but few correctly resolve the frequency distribution, interannual variability in number and amplitude of moisture flux, and median landfalling latitude.

The response of a subset of high performing models to projected warming at the end of the 21^{st} century is investigated using Representative Concentration Pathway (RCP) 8.5 (2070 - 2100) projections. Selected models show a broadening of the frequency distribution, with the largest increase in frequency occurring equatorward of peak historical frequency. While there is a robust increase in AR-related moisture transport compared to the historical

period, this increase is not linked to more extreme AR events within the context of the projected future climate. The occurrence of years with many AR dates is greater at the end of the 21^{st} century than during the historical period. The equatorward increase in peak historical frequency is co-located with increases in the 850- and 250-hPa zonal winds. The moisture flux response to warming is mostly thermodynamic, but dominated by a dynamic response equatorward of its peak distribution.

5.1 Introduction

Despite their filamentary geometry, atmospheric rivers (ARs) play an important role in meridional moisture transport and in the global redistribution of heat from the tropics (*Zhu and Newell*, 1998; *Bao et al.*, 2006; *Newman et al.*, 2012). They are characterized by high moisture content and a strong low-level jet (*Ralph et al.*, 2004). ARs are closely associated with the warm conveyor belt within the warm sector of extratropical cyclones and are sustained by pre-frontal moisture convergence (*Bao et al.*, 2006; *Stohl et al.*, 2008; *Sodemann and Stohl*, 2013; *Dacre et al.*, 2015). When they cross over land (so-called landfall), they are a major source of cold-season precipitation (*Neiman et al.*, 2008a; *Dettinger et al.*, 2011; *Dettinger*, 2013). The extreme precipitation and flooding that sometimes accompany landfalling ARs over coastal areas with steep topography can have severe socio-economic consequences.

Given the essential role ARs play in the hydrological cycle and extratropical moisture transport (*Newman et al.*, 2012), the influence of projected climate change on AR behavior must be considered. Lower-tropospheric atmospheric moisture is expected to increase with warming, in-line with the Clausius-Clapeyron relation (see review in *Meehl et al.* (2007)). The increase in atmospheric moisture with warming has been found to result in a robust increase in the horizontal moisture transport in model projections, with little change in vertical mass fluxes (*Held and Soden*, 2006; *Lavers et al.*, 2015).

The association of ARs with extratropical cyclones and the mid-latitude storm track must also be considered. In the Northern Hemisphere, amplified surface warming at high latitudes decreases the surface meridional temperature gradient, while the warming of the

tropical upper troposphere increases the upper level temperature gradient. These changes are associated with an increase in upper tropospheric eddy kinetic energy and the vertical expansion of the climatological storm track (*Yin*, 2005; *Chang et al.*, 2012). ARs over the eastern North Pacific are closely related to Rossby wave propagation and breaking (*Ryoo et al.*, 2013; *Payne and Magnusdottir*, 2014). *Payne and Magnusdottir* (2014) showed a link between intense landfalling ARs and the development of anticyclonic Rossby wave breaking over the eastern North Pacific. The association of Rossby wave breaking with the exit region of the mid-latitude jet is, therefore, of importance in understanding the behavior of landfalling ARs. Over the North Pacific, *Barnes and Polvani* (2013) have identified an increased meridional wobbling of the jet at the end of the 21^{st} century in Representative Concentration Path (RCP) 8.5 projections from the fifth phase of the Coupled Model Intercomparison Project (CMIP5). Increased meridional variability of the jet has implications for the location of breaking and is of interest in investigating the response of ARs to warming.

Much of the focus of recent research has been on the response of precipitation in warming projections. Few studies have focused on the explicit response of ARs, as intense moisture transport events, to warming. *Dettinger* (2011) was the first to investigate this topic using an ensemble of projections from seven global climate models used in the fourth Intergovernmental Panel on Climate Change (IPCC) assessment report. Comparing historical simulations to end of the century warming projections, he found an increase in moisture transport and an increase in the number of years with many ARs. Investigation was furthered by use of data from CMIP5 in *Warner et al.* (2015). They identified ARs using the 99^{th} percentile of moisture transport along a transect just off the coast of North America in thirty years of historical simulations and RCP 8.5 projections from ten different models. Similar to the findings in *Dettinger* (2011), *Warner et al.* (2015) found a robust increase in moisture transport within ARs, but little change in lower-level winds. While focused on the eastern North Atlantic, *Lavers et al.* (2013) found similar increases in AR intensity as *Dettinger* (2011) and *Warner et al.* (2015) using an ensemble of five models participating in CMIP5 and a

different method to identify ARs.

A comprehensive overview of the performance of the CMIP5 models in resolving landfalling ARs over the North Pacific has yet to be undertaken. Here, we evaluate the statistics of landfalling ARs in historical simulations of 28 different CMIP5 models. We add to the existing research by identifying a subset of high performing CMIP5 models for North Pacific ARs and characterize the AR response to warming using CMIP5 simulations under the RCP 8.5 forcing scenario. Our emphasis is on the large-scale dynamics, in association with Rossby wave dynamics, that generate the sometimes quite delicate AR spatial structures (*Payne and Magnusdottir*, 2014).

The purpose of this paper is two-fold: (1) to evaluate the ability of CMIP5 models to simulate landfalling ARs over the eastern North Pacific and (2) to investigate the response of AR behavior to projected climate change, specifically focusing on their dynamical responses. The paper is organized as follows. In section 5.2, we outline the CMIP5 models and simulations we use, how landfalling ARs are identified in each dataset and summarize our evaluation metrics. In section 5.3, we evaluate the ability of CMIP5 historical simulations to resolve AR frequency over the North Pacific as compared to two different reanalysis products. In section 5.4, we investigate changes in AR behavior in end of the century RCP 8.5 projections. We summarize our conclusions in section 5.5.

5.2 Data and Methods

5.2.1 Datasets

In order to comprehensively evaluate CMIP5 performance, we use data from 28 models originating from 18 different modeling groups participating in CMIP5. From each model, we use two sets of simulations: historical (1980 - 2004) and RCP 8.5 projections (2070 - 2099). Historical simulations are forced by both anthropogenic and natural changes in atmospheric composition, and include changes in land cover (*Taylor et al.*, 2012). While data from historical simulations are available over the entire industrial period, we focus on the years that have overlap with our reanalysis datasets (satellite era) and are common

Table 5.1: Details for all 28 CMIP5 models used in order of resolution (historical, 1980 - 2005 and RCP 8.5, 2070 - 2100). A numerical identifier is shown in the first column, model name in the second column, spatial resolution in the third column and modeling group in the fourth column.

ID	Model	Resolution	Group
01	CMCC-CESM	3.7 × 3.7	Centro Euro-Mediterraneo per I Cambiamenti Climatici
02	FGOALS-g2	3.1 × 3.1	LASG,Institute of Atmospheric Physics, Chinese Academy of Sciences and CESS,Tsinghua University
03	BNU-ESM	2.8 × 2.8	College of Global Change and Earth System Science, Beijing Normal University
04	bcc-csm1-1	2.8 × 2.8	Beijing Climate Center, China Meteorological Administration
05	CanESM2	2.8 × 2.8	Canadian Centre for Climate Modelling and Analysis
06	MIROC-ESM-CHEM	2.8 × 2.8	Japan Agency for Marine-Earth Science and Technology, Atmosphere and Ocean Research Institute (The University of Tokyo), and National Institute for Environmental Studies
07	MIROC-ESM	2.8 × 2.8	Japan Agency for Marine-Earth Science and Technology, Atmosphere and Ocean Research Institute (The University of Tokyo), and National Institute for Environmental Studies
08	GFDL-ESM2G	2.0 × 2.0	NOAA Geophysical Fluid Dynamics Laboratory
09	GFDL-ESM2M	2.0 × 2.0	NOAA Geophysical Fluid Dynamics Laboratory
10	NorESM1-M	1.9 × 1.9	Norwegian Climate Centre
11	IPSL-CM5A-LR	1.9 × 1.9	Institut Pierre-Simon Laplace
12	IPSL-CM5B-LR	1.9 × 1.9	Institut Pierre-Simon Laplace
13	CMCC-CMS	1.9 × 1.9	Centro Euro-Mediterraneo per I Cambiamenti Climatici
14	MPI-ESM-LR	1.9 × 1.9	Max Planck Institute for Meteorology
15	CSIRO-Mk3-6-0	1.9 × 1.9	Commonwealth Scientific and Industrial Research Organization in collaboration with Queensland Climate Change Centre of Excellence
16	inmcm4	1.5 × 1.5	Institute for Numerical Mathematics
17	MIROC5	1.4 × 1.4	Atmosphere and Ocean Research Institute (The University of Tokyo), National Institute for Environmental Studies, and Japan Agency for Marine-Earth Science and Technology
18	CNRM-CM5	1.4 × 1.4	Centre National de Recherches Mètèorologiques/Centre Européen de Recherche et Formation Avancee en Calcul Scientifique
19	IPSL-CM5A-MR	1.3 × 1.3	Institut Pierre-Simon Laplace
20	ACCESS1-0	1.2 × 1.2	Commonwealth Scientific and Industrial Research Organization (CSIRO) and Bureau of Meteorology (BOM), Australia
21	ACCESS1-3	1.2 × 1.2	Commonwealth Scientific and Industrial Research Organization (CSIRO) and Bureau of Meteorology (BOM), Australia
22	HadGEM2-CC	1.2 × 1.2	Met Office Hadley Centre
23	EC-EARTH	1.1 × 1.1	EC-EARTH consortium
24	MRI-CGCM3	1.1 × 1.1	Meteorological Research Institute
25	MRI-ESM1	1.1 × 1.1	Meteorological Research Institute
26	bcc-csm1-1-m	1.1 × 1.1	Beijing Climate Center, China Meteorological Administration
27	CCSM4	0.9 × 0.9	National Center for Atmospheric Research
28	CMCC-CM	0.7 × 0.7	Centro Euro-Mediterraneo per I Cambiamenti Climatici

among all models. We evaluate the response of ARs to warming in the most extreme scenario available, RCP 8.5, in which radiative forcing increases to a peak of 8.5 W m^{-2} by the end of the 21^{st} century (*Taylor et al.*, 2012).

Only a handful of models output daily fields for multiple ensembles. Therefore, we chose to limit our study to that of a single ensemble member from each model (the first available). Specific humidity (q), and zonal and meridional winds (u, v) are downloaded on pressure levels 1000-, 850-, 500-, 250-hPa from a central repository, the Earth System Grid - Center for Enabling Technologies (ESG-CET) (http://pcmdi9.llnl.gov/esgf-web-fe/). Further information on each model is detailed in Table 5.1.

We use reanalysis data to serve as an 'observational' comparison for quality control over the period 1980 - 2004. We use MERRA reanalysis (*Rienecker et al.*, 2011) at 1.25° × 1.25° horizontal resolution, and ERA-Interim reanalysis (*Dee et al.*, 2011) at 0.75° × 0.75° horizontal resolution. For consistency with CMIP5 data, daily averages are used. Both reanalysis datasets have previously been used to study ARs and they perform well against observational case studies (e.g. *Jiang and Deng* (2011); *Lavers et al.* (2012); *Ryoo et al.* (2013); *Rutz et al.* (2014); *Payne and Magnusdottir* (2014)).

We focus on the extended winter (defined as October through March), which is considered the active season for ARs over the North Pacific (*Neiman et al.*, 2008a). Here, years are referred to as starting in October and ending in March. As there is no consistent calendar type between the different datasets, we remove 29 February from each leap year resulting in a 365-day year. The exception is the Hadley model (HadGEM2-CC), which has a 360-day year.

5.2.2 AR identification

We focus on ARs making landfall, which is defined by physical proximity to the coastline between 30°N and 60°N in the eastern North Pacific, using the methods described in *Payne and Magnusdottir* (2014) (see their Figure 1). We note that the spatial resolution of the majority of the CMIP5 models is coarser than the fine-scale ARs. Therefore, in order to

identify AR-like features in this dataset, we look for events with high moisture transport and an elongated geometry, impacting the coastline. Since our analysis extends over different models and two climates, landfalling AR dates are defined according to dataset-dependent percentiles based on the historical simulation for each model (e.g. *Lavers et al.* (2012)). Our threshold on vertically integrated moisture flux *MF* (as defined in Eq. 5.1 below) is distribution based and fixed to the 85^{th} percentile of *MF* over all dates for the extended winter (Oct - Mar) (*Lavers et al.*, 2013).

The following criteria are used to detect AR-like features: (1) *MF* exceeds the 85^{th} percentile over the landfall region (verified in all models to be above the static 250 kg m^{-1} s^{-1} threshold commonly used, e.g. *Rutz et al.* (2014); *Warner et al.* (2015)), (2) precipitable water (*PW*, as defined in Eq. 5.2 below) exceeds 2 cm (*Ralph et al.*, 2004; *Neiman et al.*, 2008a), (3) the 850 hPa zonal and meridional components of the wind are both positive and the wind speed exceeds 10 m s^{-1} (*Neiman et al.*, 2008a; *Dettinger*, 2011; *Hagos et al.*, 2015). We also require that the long axis of the identified feature extends more than 2000 km in the zonal direction (*Ralph et al.*, 2004). We note that the combination of the dataset-dependent percentile thresholds over a range of variables means the total number of landfalling AR dates varies between datasets. Using this set of criteria, MERRA captures 80% and ERA-Interim captures 77% of the dates listed in Tables 1 and 2 of *Neiman et al.* (2008a). Both reanalysis datasets capture the notable February 1986 and January 1997 landfalling AR events (*Leung and Qian*, 2009).

Our reanalysis datasets are at spatial resolutions approximately equal to or higher than the majority of the CMIP5 models investigated. For direct comparison of reanalysis with CMIP5 data, we interpolate all datasets to a common $2^\circ \times 2^\circ$ grid using bilinear interpolation after case selection.

MF is calculated as the product of the horizontal wind speed and the specific humidity

vertically integrated from 1000 hPa to 500 hPa:

$$MF(\lambda, \phi, t) = g^{-1} \left| \int_{p_s}^{p_t} q(\lambda, \phi, p, t) \mathbf{V}(\lambda, \phi, p, t) \mathrm{d}p \right|, \tag{5.1}$$

where $\mathbf{V}$ is the horizontal velocity and q is specific humidity (both in SI units), g is 9.81 m s^{-2}, p_s is 1000 hPa and p_t is 500 hPa. We calculate the climatology for each date in the extended winter, over all years, for each dataset (1980 - 2004 and 2070 - 2099, respectively). For identified landfalling AR dates, the daily *MF* anomaly is the difference between the *MF* value and the *MF* climatology for that day of the season.

PW is calculated as specific humidity in units of equivalent depth of a liquid unit column of water, vertically integrated from 1000 hPa to 500 hPa:

$$PW(\lambda, \phi, t) = (g\rho_w)^{-1} \int_{p_s}^{p_t} q(\lambda, \phi, p, t) \mathrm{d}p, \tag{5.2}$$

where ρ_w is 1000 kg m^{-3}.

The horizontal length of the feature is determined by connected gridpoints satisfying the criteria on *MF*, *PW* and the 850 hPa horizontal winds (described above), trailing westward from the point of landfall (similar to that described in *Lavers et al.* (2013)). With the exception of seasonal and interannual analysis, we use composites over all landfalling dates to investigate differences between reanalysis products and historical simulations.

5.2.3 Statistical metrics

We use several different measures to evaluate model performance in representing landfalling ARs compared to the two reanalysis datasets. All horizontal calculations are weighted by the normalized square-root of the cosine of latitude. Model bias (B) is defined as the difference between the model historical data (M) and each reanalysis dataset (O). Spatial correlations between each model and observations are quantified using the area-weighted Pearson correlation coefficient (R).

To describe the amplitude of the differences between the models and the observations, we calculate the area-weighted root-mean square error (E):

$$E = \sqrt{\sum_{i=1}^{N} (M_i - O_i)^2}. \tag{5.3}$$

To allow for the comparison of the error in each model for a given reanalysis dataset and field, we calculate the relative model error, $E^{'}$ (*Gleckler et al.*, 2008):

$$E^{'} = \frac{E - \widetilde{E}}{\widetilde{E}}, \tag{5.4}$$

where, $\widetilde{E}$ is the median error over all models for a given observational dataset and field. This quantity allows for comparison of the relative amount of error in each model so that models with a low $E^{'}$ have less error than models with a high $E^{'}$.

While we use criteria-based methods to rank models in subsections 5.3.1 and 5.3.2, we summarize model performance against reanalysis by quantifying model rank using the Taylor score, S (*Taylor*, 2001):

$$S = \frac{4\,(1+R)^4}{\left(\sigma_M/\sigma_O + \sigma_O/\sigma_M\right)^2 (1+R_o)^4}, \tag{5.5}$$

where R_o is the maximum correlation attainable, which is here assumed to be 1, and σ is the standard deviation of each model (σ_M) and of each reanalysis dataset (σ_O). For each model we calculate the Taylor score for a range of variables, and approximate model performance by averaging the Taylor scores over all variables. We weight the average model score by the standardized difference from the average number of AR dates in reanalysis.

5.3 Evaluation of landfalling ARs in historical CMIP5 simulations

This section is broken into three parts; we focus on: (1) the frequency of AR-like conditions over the basin during landfalling dates, (2) the total number of dates identified by each

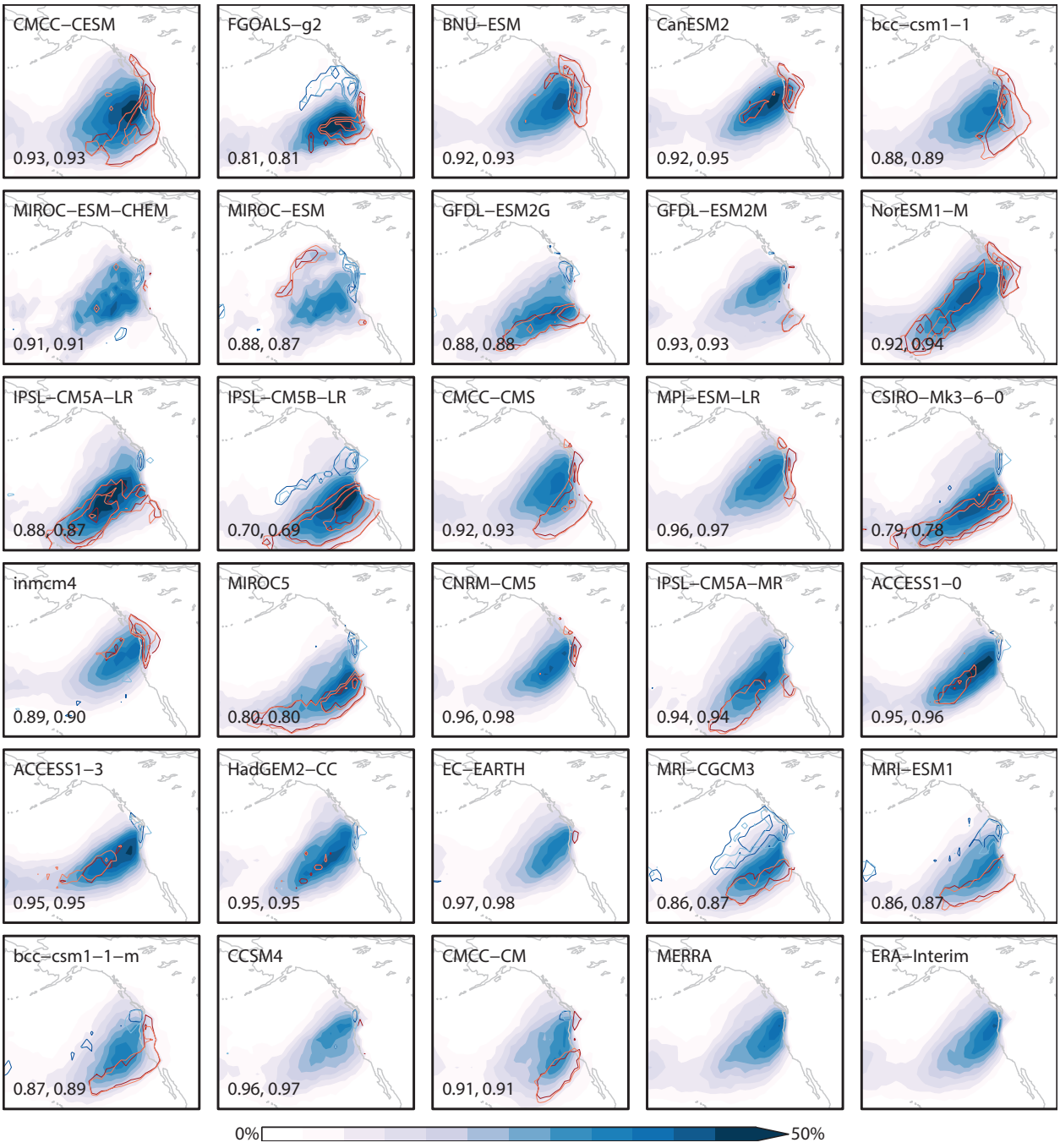

Figure 5.1: For historical simulations (1980 - 2004), AR frequency (shading, %) for all models (lowest resolution, top left to highest resolution, bottom right) compared against MERRA and ERA-Interim reanalysis in the lower right corner. Model bias (MERRA, dark and ERA-Interim, light) is shown in contours (intervals of 10%, from ±10%, where blue is negative and red is positive). The correlation coefficient is shown in the lower left corner of each panel (MERRA, ERA-Interim). Only statistically significant bias shown (Student's t-test, 95% level).

model, including their seasonal and interannual variability, and (3) the deviation in relevant fields from reanalysis (frequency of occurrence, moisture flux, specific humidity, and the zonal and meridional winds at 850- and 250-hPa). The purpose of this section is to identify those models that best simulate the statistics of extreme moisture transport over the eastern North Pacific. We focus our evaluation specifically on landfalling AR dates over the historical period so that the selected models may be used to evaluate their response to warming in RCP 8.5 simulations.

5.3.1 AR distribution and amplitude

AR frequency

Figure 5.1 shows the frequency of AR occurrence (shaded) and model bias (contoured) for each of the CMIP5 models. Frequency is defined as the total number of times each gridpoint satisfies criteria detailed in section 5.2.2, divided by the total number of landfalling AR dates identified in each model over the entire time period (1980 - 2004, Oct - Mar). In order to consider the role of model native resolution in their performance, panels are ordered from lowest resolution in the top left (CMCC-CESM), to highest resolution in the bottom right (CMCC-CM). The two reanalysis datasets are shown in the bottom right.

Comparison of the frequency distribution of the two reanalysis datasets shows excellent agreement over the ocean ($R = 0.988$, $p \leq 0.01$). Differences between the two datasets are concentrated over land (not shown). Overall, models capture the general shape of AR frequency. Frequency peaks in the Pacific Northwest and Northern California regions and drops off towards lower latitudes along the coastline. From the coastline, this peak in frequency trails westward and equatorward over the basin, consistent with observations (*Neiman et al.*, 2008a). Closer examination of the frequency distribution for each dataset, however, shows large variation. Correlation coefficients (relative to MERRA and ERA-Interim, respectively) are shown in the lower left of each panel and show variable performance, with correlations ranging from a low of 0.69 (IPSL-CM5B-LR) to a high of 0.98 (EC-EARTH) (Fig. 5.1).

For a comprehensive overview of the distribution of AR frequency over the domain shown

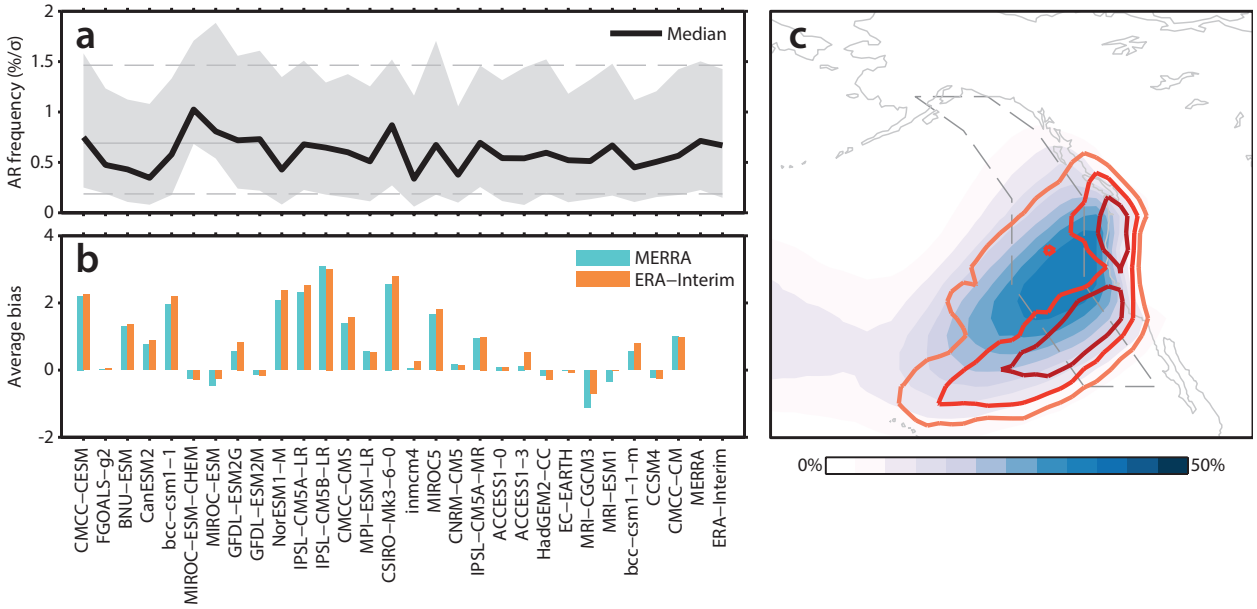

Figure 5.2: (a) The standardized distribution of non-zero AR frequency for each model in order of resolution (left to right) and MERRA and ERA-Interim reanalysis (far right), as represented by their median (black) and 25^{th} (bottom edge) and 75^{th} (top edge) percentiles. For reference, the average median (solid grey) and 75^{th} and 25^{th} percentiles (dashed grey, top and bottom, respectively) for both reanalysis are shown as horizontal lines. (b) For statistically significant bias (Student's t-test, 95% level), the average bias for each model compared to (blue) MERRA and (orange) ERA-Interim reanalysis. (c) For AR frequency, the standard deviation across all models (contour intervals of 2σ, from 6σ) and the multi-model mean (shading, intervals of 10%, from 10%). The outlined region (25°N - 60°N) is used to calculate anomalies for Fig. 5.3.

in Fig. 5.1, we show the standardized frequency distribution for each dataset (the frequency distribution divided by its standard deviation) in Fig. 5.2a. Shading indicates values between the 25^{th} and 75^{th} percentiles and the solid black line refers to the median frequency. Again, agreement between the two reanalysis datasets is excellent, with consistent median (MERRA: 0.71, ERA-Interim: 0.67) and quantile values (MERRA: 0.23−1.50, ERA-Interim: 0.15−1.43). With the exception of MIROC-ESM-CHEM and MIROC-ESM, model frequency distribution is generally consistent with reanalysis. Models tend to under-estimate median frequency ($\sim 0.1\%/\sigma$ lower than average reanalysis) and high extremes ($\sim 0.07\%/\sigma$ lower than average reanalysis).

Model bias

Returning to Fig. 5.1, we show the spatial distribution of model bias calculated as the difference in frequency between each model and each reanalysis dataset. Positive bias is indicated by red contours, negative bias is indicated by blue contours, and each reanalysis dataset is distinguished by contour shading (MERRA, dark colored contours and ERA-Interim, light colored contours). At each gridpoint, we calculate significance using a two-sided Student's t-test in which the interannual variation in AR frequency is used for sample variance, following the example in *Anstey et al.* (2013). Only statistically significant bias (at the 95% level) is reported.

Comparison of the bias relative to each reanalysis dataset shows very good agreement both in magnitude and in location (compare dark and light contours in Fig. 5.1). To provide a quantitative overview of the bias in each model, Fig. 5.2b shows the average magnitude of bias over all points for all models. While a comparison of bias between the lowest resolution models (top left) and the highest resolution models (bottom right) show a general decrease with increasing resolution, bias does not scale linearly with resolution. Changes in the resolution of the common grid do not have any impact on the results reported here. Average bias is generally positive indicating a spatial overestimation of AR frequency compared to reanalysis. We confirm this in Fig. 5.2c where we show the multi-model composite of AR frequency (shading) and its standard deviation calculated over all 28 models (contouring). The figure illustrates the largest disagreement between models is concentrated equatorward of the peak frequency, indicating disagreement in the average latitudinal position of AR landfall. We note that this peak in standard deviation is not an artifact of high moisture.

***MF* distribution and amplitude**

We further our investigation of the spatial variability of ARs in the different models in Fig. 5.3, which shows Hövmoller diagrams of the seasonal variability over all years for each model compared to reanalysis (in the lower right corner). Each seasonal composite is composed of the sector zonal average (over the dashed box in Fig. 5.2c) standardized *MF*

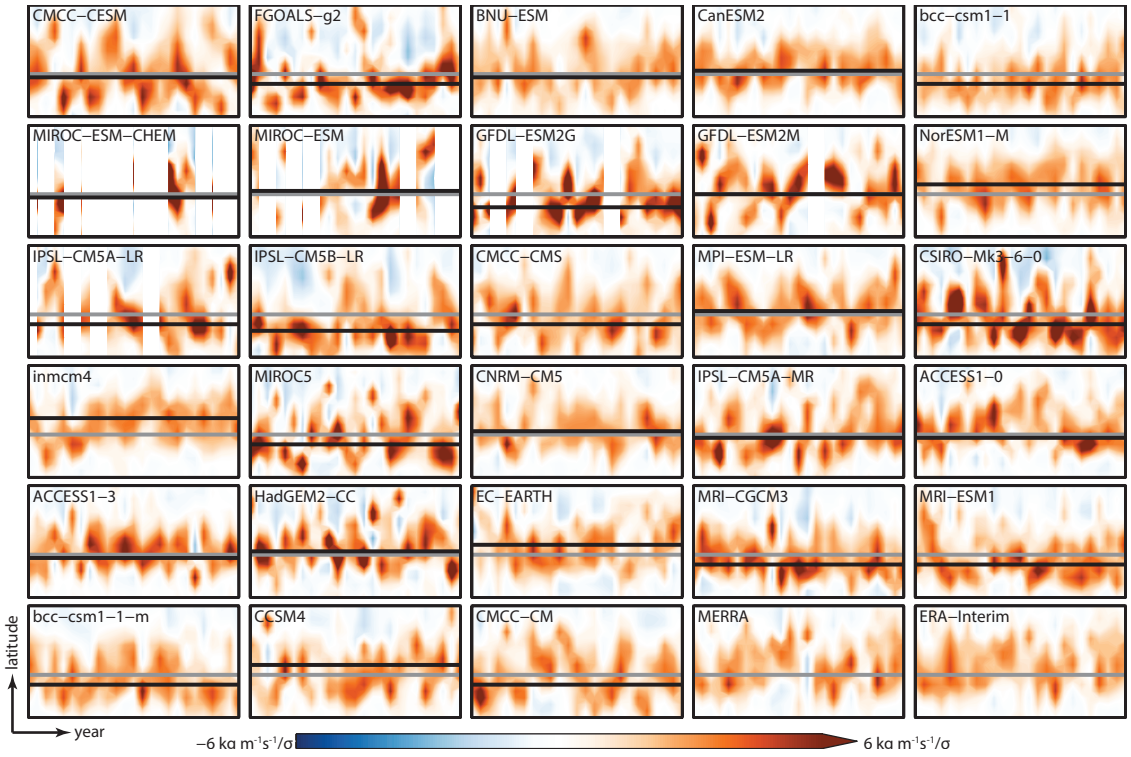

Figure 5.3: For historical simulations (1980 - 2004), a Hövmoller diagram of the interannual variability for the extended winter (x-axis) of the sector zonal average (calculated over dashed region in Fig. 5.2c) of daily anomalies of *MF* for landfalling AR dates. The median latitude of positive *MF* anomalies in each model (black) is compared to that in the average of both reanalysis (grey).

anomalies for all landfalling AR dates. Positive anomalies of *MF*, as areas of anomalously high moisture transport, are used as a proxy for AR frequency. We compare the median latitude of the peak in positive anomalies between each model (black) and the average over reanalysis (grey). As we do not require an equal number of AR dates to be identified in each model (discussed in detail in section 5.3.2), years with no identified dates are shown in white. It is apparent from Fig. 5.3 that the performance of models in resolving AR latitude compared to reanalysis varies greatly. While several models show an equatorward shift in median latitude relative to reanalysis, this shift varies in magnitude and is not consistent with changes in model resolution.

Differences in the amplitude of positive *MF* anomalies are less consistent with changes in resolution. Figure 5.4a shows the yearly amplitude of positive *MF* anomalies (shown in Fig. 5.3) across all models compared to the average amplitude from reanalysis (MERRA, blue and ERA-Interim, orange). For models, we note that we are focusing not on the year-to-year variability, but rather on the overall amplitude of variability. While the median amplitude of the standardized positive *MF* anomalies is consistent with reanalysis, the total range of values over all models is quite large. In particular, model extremes are largely overestimated. This may be due to differences in the total number of dates identified in each model, which will be addressed in section 5.3.2.

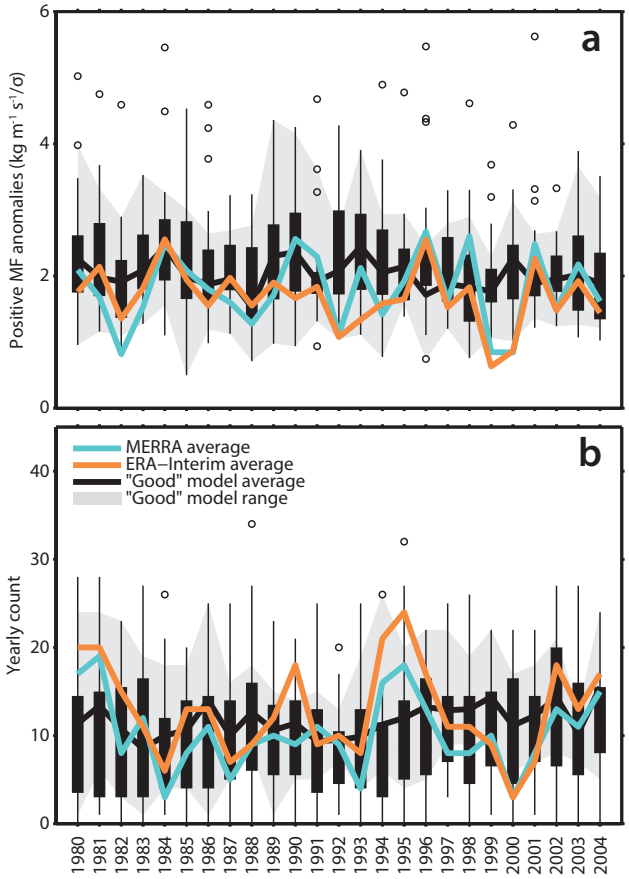

Figure 5.4: For all models, a box-and-whisker plot showing (a) the range of positive *MF* anomalies for landfalling AR dates identified in each extended winter year (Oct - Mar) and (b) yearly counts of landfalling AR dates. The solid boxes show the model spread between the 25^{th} and the 75^{th} quantiles, with the median shown as a black line. The circles represent outliers. The averages for MERRA (blue) and ERA-Interim (orange) are shown in each panel. The range of the high performing subset of models is shown in grey shading, with their average (black) in reference to the evaluation in (a) section 5.3.1 and (b) section 5.3.2.

Overview

In this subsection we evaluated the distribution of landfalling AR dates in historical model simulations and investigated differences in the amplitude of identified events using *MF* anomalies. Based our analysis, we can characterize high performing models as those hav-

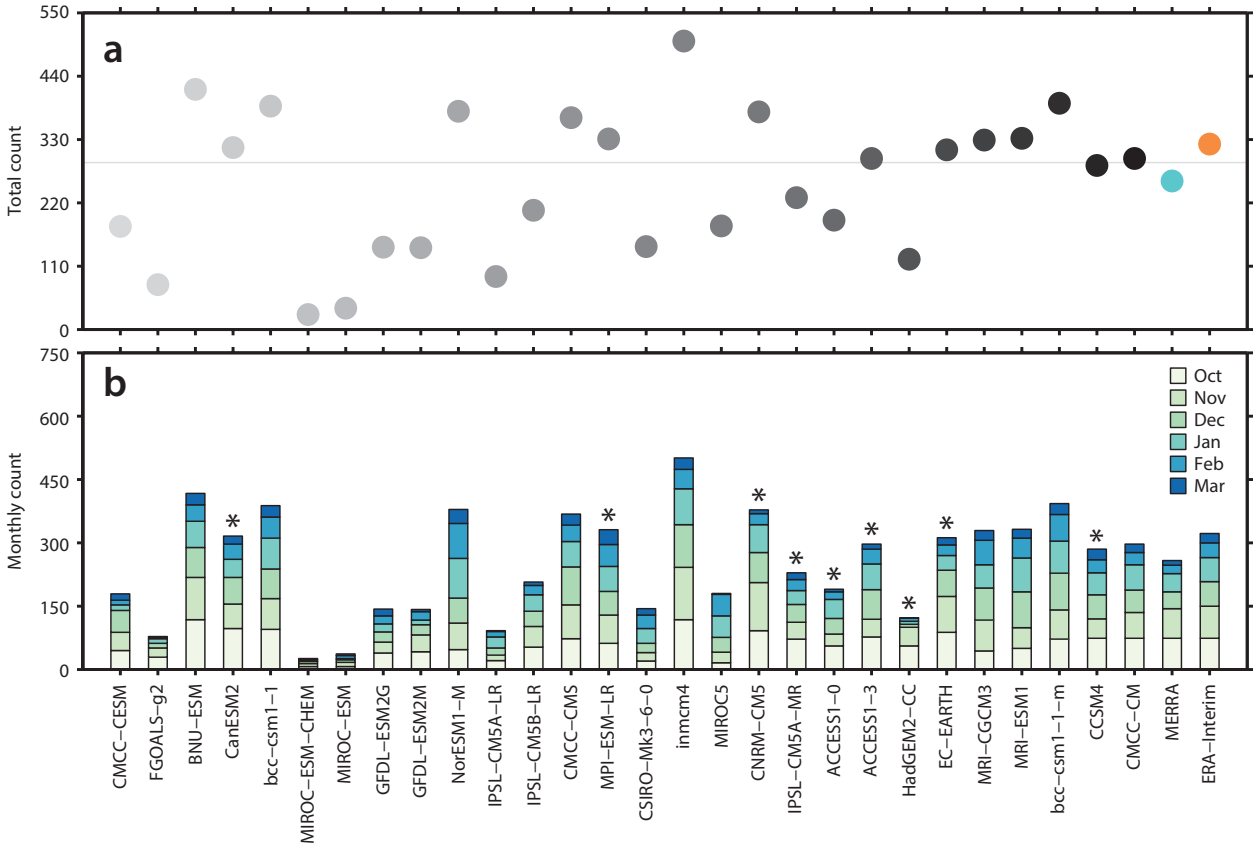

Figure 5.5: (a) The total number of landfalling dates selected by each model (lowest resolution, lightest grey and highest resolution, darkest grey) compared to reanalysis (MERRA, blue and ERA-Interim, orange). (b) The separation of the total number of landfalling dates into monthly counts. The subset of high performing models identified in section 5.3.1 are marked with an asterisk.

ing: (1) high spatial correlation of AR frequency relative to reanalysis (R$\geq$ .93), (2) low average bias ($\overline{B} \leq 1$), and (3) a median latitude of positive *MF* anomalies close to the average of reanalysis ($\leq 3°$). By this criterion, an initial subset of high performing models include CanESM2, MPI-ESM-LR, CNRM-CM5, IPSL-CM5A-MR, ACCESS1-0, ACCESS1-3, HadGEM2-CC, EC-EARTH and CCSM4. To test the performance of this subset against all models considered, we return to Fig. 5.4a, where we show their range (shading) in positive *MF* anomalies. These models show a marked improvement of the multi-model ensemble and generally capture the range of the interannual variability of *MF* amplitude in reanalysis. Many of the extreme outliers present in the original 28 models are excluded in this subset.

5.3.2 Seasonal evolution and interannual variability

Total counts and seasonal evolution

Figure 5.5 shows the total number of landfalling dates identified in each dataset and the breakdown of that total into the number identified in each month. Resolution increases from left to right with the two reanalysis datasets shown at the far right side of the figure. There is rather good agreement between the two reanalysis datasets, with more AR dates identified in ERA-Interim (322) than in MERRA (258). Compared to reanalysis, the number of AR dates identified in models varies widely. The highest number of landfalling dates are identified in inmcm4 (501) and the fewest are identified in MIROC-ESM-CHEM (26). Generally, increases in model resolution are associated with an increased consistency in the number of identified AR dates compared with reanalysis.

From observations we know that the highest number of landfalling events (over the entire coastline) occur early in the season (*Neiman et al.*, 2008a). Models generally perform well against observations, identifying more AR dates early in the season. Exceptions to this seasonality include NorESM1-M, MIROC5 and CSIRO-Mk3-6-0.

Interannual variability in total counts

Figure 5.4b shows the interannual variability of identified landfalling dates for each year in the historical period as compared to the two reanalysis datasets for all models. Again, the

two reanalysis datasets are consistent with each other, with notable exceptions in 1982, 1990 and 1995. However, given the difference in the total number of dates identified by each dataset, this is to be expected (there are 64 more dates identified in ERA-Interim). While the number of identified dates in all models varies widely each year, their average amplitude is generally consistent with observations.

Overview

In this subsection we evaluated the number of AR dates identified and their seasonal and interannual variation. We add to our criteria of high performing models from section 5.3.1, to include: (1) total counts consistent with observations (within 100 of the average of reanalysis) and (2) a higher number of identified dates early in the season.

For a closer investigation of their seasonal variability, we indicate the subset of models identified in section 5.3.1 in Fig. 5.5b with an asterisk. All models in this subset correctly resolve the AR seasonality, with the highest number of AR dates in the earliest three months (Oct - Dec) and the fewest in the last three months (Jan - Mar). Likewise, the majority of the identified models have total counts consistent with observations. An exception is HadGEM2-CC, which we now exclude from our subset.

Returning to Fig. 5.4b, we again test the performance of our revised subset and show their range of yearly counts in shading (EC-EARTH, CNRM-CM5, MPI-ESM-LR, CCSM4, ACCESS1-0, ACCESS1-3, IPSL-CM5A-MR, and CanESM2). While totals remain consistent with reanalysis, comparison of the model average of the subset with reanalysis still shows some over- and under-estimation of total counts, though now within the range of what is seen in reanalysis.

5.3.3 Model performance summary

In this subsection we evaluate the performance of all models against relevant fields: (1) AR frequency, (2) *MF*, (3) 850 hPa specific humidity, (4) 850 hPa horizontal winds, and (5) 250 hPa horizontal winds. We investigate the performance of each model against upper-level

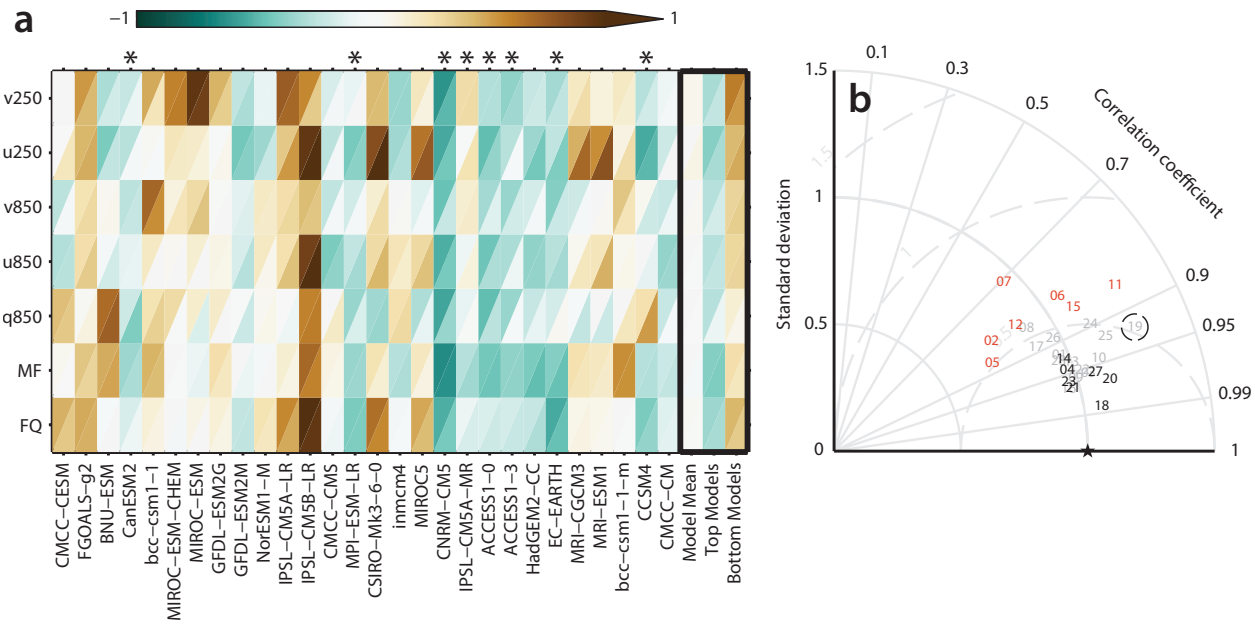

Figure 5.6: (a) A portrait diagram display of the relative error for each model (x-axis) against each observational dataset (MERRA, top triangle and ERA-Interim, bottom triangle) over (y-axis, from top) 250 hPa meridional wind (v250), 250 hPa zonal wind (u250), 850 hPa meridional wind (v850), 850 hPa zonal wind (u850), 850 hPa specific humidity (q850), *MF* and AR frequency (FQ). (b) Taylor diagram display of the average model performance for variables (each standardized by reanalysis) in (a). Models are identified by their ID in Table 5.1, where both reanalyses are represented by a black star. Points are positioned according to their standard deviation (radial distance from the origin), root mean square error (radial distance from reanalysis) and correlation (azimuthal position). The identifiers for the final list of the subset of high performing models are in black bold and for the 7 lowest performing models, are in red bold.

winds because of the association of intense ARs with the extratopical jet and Rossby wave dynamics (*Payne and Magnusdottir*, 2014). Figure 5.6a shows the relative error, E′ for each variable (y-axis) from each model (x-axis). Each grid box is divided along the diagonal to show calculations relative to MERRA reanalysis (bottom triangle) and ERA-Interim reanalysis (top triangle). The shading shows where models have high error (positive, brown) and low error (negative, teal) relative to the entire set of models being evaluated. The revised subset of models identified in the previous subsection is marked by an asterisk at the top of Fig. 5.6a.

Results show that during landfalling AR dates, relative error tends to be consistent across

different metrics and there is a clear separation between high and low performing models. The subset of models previously identified all show relatively low error. The exception is IPSL-CM5A-MR, which is inconsistent with reanalysis for both upper and lower level winds and shows marginal improvement in performance over the remaining metrics. CCSM4 shows poor performance in lower level moisture, but otherwise performs reasonably well.

Figure 5.6b shows a Taylor diagram display (see *Taylor* (2001) for details) of the average of standardized metrics for each variable shown in Fig. 5.6b, where models are indicated by their numerical identifier from Table 5.1. High performing models are those falling closest to reanalysis (black star). Radial distance of each point from the origin shows standard deviation. Radial distance of each point from reanalysis shows error and the azimuthal position of each point shows the correlation. The identifier for each high performing model in our subset is in bold (black). The poor performance of IPSL-CM5A-MR (dashed circle in Fig. 5.6b) is reflected in its distance from the other models in the subset. For this reason, we exclude IPSL-CM5A-MR from our subset.

Models are ranked according to the average of the Taylor scores and standardized difference from the average number of AR dates in reanalysis. In Fig. 5.6a (black outline), the relative error for the model mean is compared to our subset of high performing models (EC-EARTH, CNRM-CM5, MPI-ESM-LR, CCSM4, ACCESS1-0, ACCESS1-3, and CanESM2) and to the lowest seven performing models (FGOALS-g2, bcc-csm1-1, MIROC-ESM-CHEM, MIROC-ESM, IPSL-CM5A-LR, IPSL-CM5B-LR, CSIRO-Mk3-6-0), identified in bold (red) in Fig. 5.6b. Error is reduced in the high performing models and increased in the low performing models.

We note that our evaluation is rather robust to changes in the AR identification scheme. Increasing the threshold on *MF* from the 85^{th} percentile to the 95^{th} percentile (close to the threshold used in *Warner et al.* (2015)) changed only 1 of the 7 high performing models we identified (CMCC-CM replaced CanESM2).

5.4 Future changes in landfalling AR dates in RCP 8.5 simulations

In this section, we: (1) characterize the change in AR behavior with warming by comparing end-of-century RCP 8.5 simulations to historical simulations and (2) decompose the moisture flux equation into the thermodynamic and dynamic components to investigate the influence on the change in AR frequency with warming. The purpose of this section is to characterize the large-scale responses of ARs, as an atmospheric feature, to warming.

5.4.1 Response of AR behavior to warming

AR frequency

Figure 5.7 shows the difference in the frequency of AR occurrence between RCP 8.5 and historical simulations (shading, with historical frequency contoured) for the 7 high performing models identified by our evaluation in section 5.3. As in section 5.3.1, frequency is defined as the total number of times each gridpoint satisfies criteria in section 5.2.2, divided by the total number of landfalling AR dates identified. The multi-model average is shown in the lower right corner. Comparison to the superimposed historical frequency distribution (contours) shows a consistent pattern of increased frequency equatorward in RCP 8.5 projections. Frequency increases (of varying magnitudes) are also apparent poleward of historical peak frequency in several models (CanESM2, MPI-ESM-LR, ACCESS1-0, ACCESS1-3,EC-EARTH). Frequency decreases are approximately co-located with the historical peak frequency, and are apparent in all models.

In order to determine whether the dominant increase in equatorward frequency is due to an absolute shift in landfalling latitude or due to a broadening of the peak frequency region, we show the sector zonal average (over the dashed box in Fig. 5.2c) of the frequency difference field in Fig. 5.7b. We compare the latitude of the frequency peak for the historical (solid black) and RCP 8.5 (dashed black) datasets to the centers of maximum standard deviation in the frequency difference field (grey solid). While there is a small difference in latitude ($\sim 2^{\circ}$), the centers of variability are generally concentrated equatorward and poleward of this latitudinal shift. These results do not change when the full ensemble of models evaluated in the

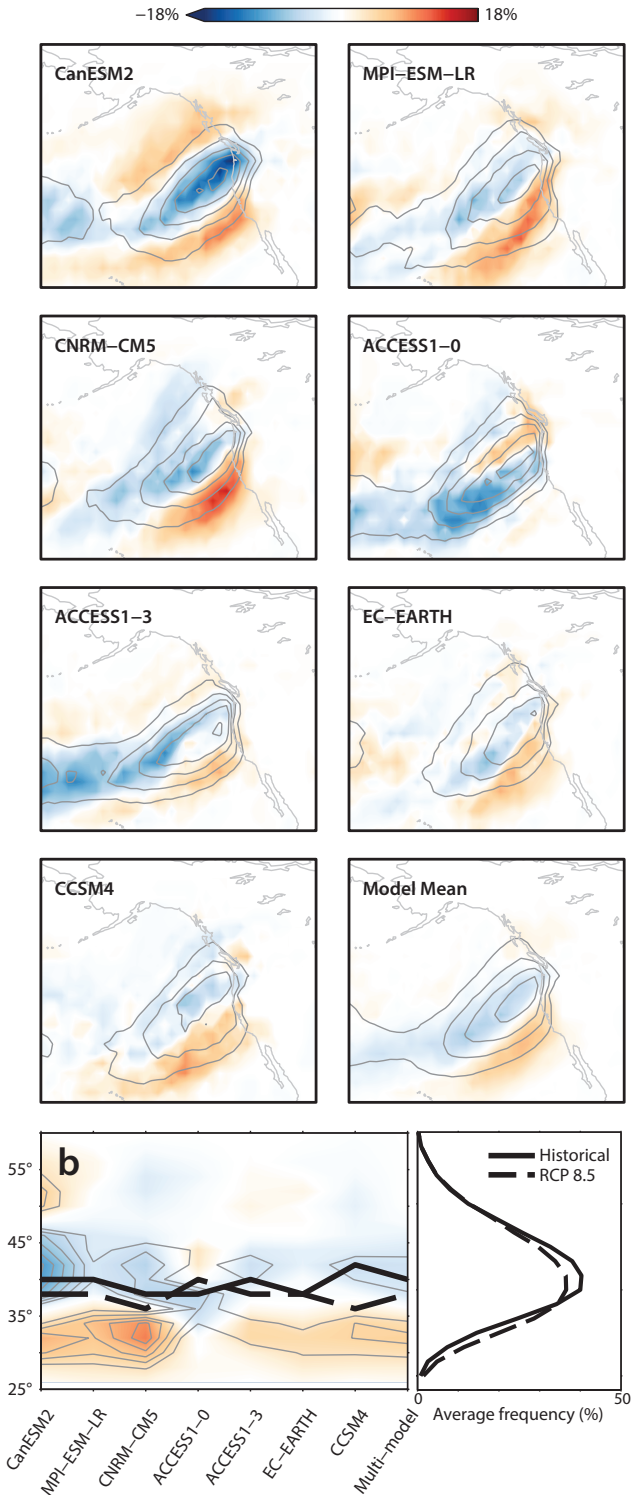

Figure 5.7: For selected models and multi-model mean, (top 8 panels) the AR frequency difference (shading, %, RCP 8.5 - historical). The historical distribution is shown in contour (intervals of 10%, starting from 10%). (b) The sector zonal average (over the dashed box in Fig. 5.2c) of the difference field. The left panel shows the latitude of peak frequency for the historical (solid black) and RCP 8.5 (dashed black) datasets, and grey contours show the standard deviation (intervals of 1σ, from 2.5σ). The multi-model zonal average frequency for each period is shown to the right in (b). 94

previous section are considered, with several exceptions (bcc-csm1-1, MIROC-ESM-CHEM, MIROC-ESM, GFDL-ESM2M, IPSL-CM5A-LR, MIROC5, IPSL-CM5A-MR, HadGEM2-CC, and CCSM4). The rather static latitudinal peak in frequency suggests that a portion of the change in the distribution in Fig. 5.7b is due to a broadening of the region of peak frequency. This means that the end of the century landfall is likely to occur over a wider latitude range than for the current climate. Broadening of the frequency distribution is confirmed in the right panel in Fig 5.7b, which shows the multi-model zonal average frequency for each period.

Interannual variability

In order to focus on the direct response of AR-like features to warming, we examine the change in *MF* at landfall. Consistent with previous research (*Lavers et al.*, 2013; *Warner et al.*, 2015), we find an absolute increase in *MF* within ARs in projections. Our results show between a 23% and 35% increase in the number of AR dates identified with warming. However, ARs are extreme events by definition. Therefore, we focus not on absolute changes in *MF*, but on changes in daily positive *MF* anomalies (as shown in Fig. 5.3) between the two climates. For a direct comparison of the interannual variability between the two datasets, we use only twenty years from each (Oct - Mar, historical: 1980 - 1999 and RCP 8.5: 2080 - 2099).

We first address the question, do ARs at the end of the century have increased intensity compared to ARs at the end of the previous century? Another way to phrase this question: Is there a shift in the distribution of moisture transport extremes? Figure 5.8a shows a comparison of the full range of positive *MF* anomalies between historical simulations (grey shading) and RCP 8.5 projections (teal shading). The mean of the distribution of each dataset is shown as a grey and a teal line, respectively. Positive *MF* anomalies in late century RCP 8.5 projections show similar amplitudes to historical simulations, with extreme values falling within the total range of historical anomalies. This is also apparent when comparing the average of the two datasets, which are statistically indistinguishable (Student's t-test at 95% level).

We do find an absolute increase in the *MF* of AR dates with warming, seen in the dashed lines in Fig. 5.8a. This increase in *MF* does translate to more intense landfalling events, which is in agreement with previous research (*Dettinger*, 2011; *Lavers et al.*, 2013; *Warner et al.*, 2015). However, within the context of the projected climate at the end of the 21^{st} century, we do not find an increased occurrence of extreme events measured as percentiles.

In Fig. 5.8b, we compare the interannual variability of the number of AR dates identified for the same two twenty year periods as in Fig. 5.8a. All models show an increase in the total number of landfalling dates in RCP 8.5 projections (between 30 and 100 days, with an average of a 62 day increase). Results generally show similar interannual variability in both datasets, with years of many and few AR dates. However, years with an extreme number of identified dates in RCP 8.5 fall well outside the historical range. This is most apparent in comparison of the years 1987/2087 and 1991/2091, in which high extremes in RCP 8.5 projections greatly exceed historical extremes. An analysis of the clustering of AR dates (multi-day landfalling events) within each dataset shows an increase in their number, but little to no change in

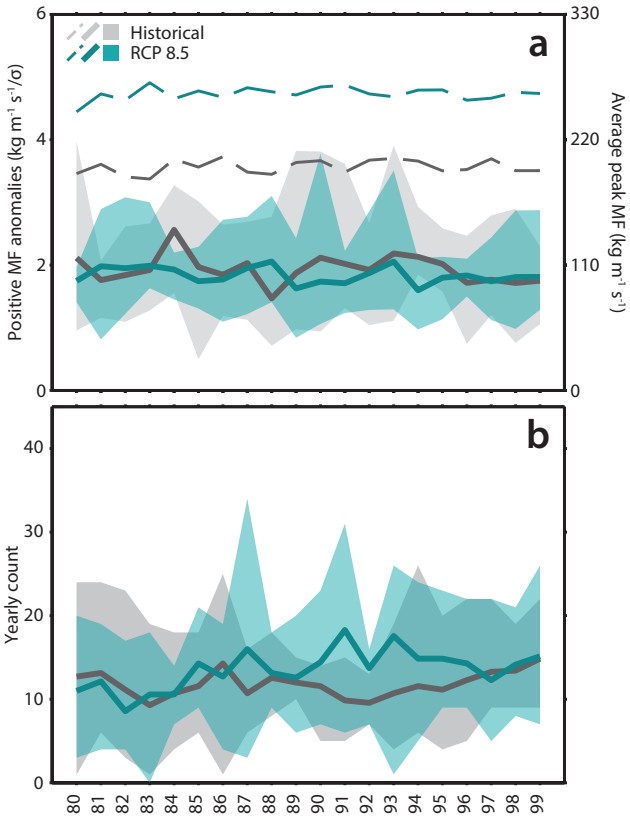

Figure 5.8: For two twenty year periods (historical: 1980 - 1999 and RCP 8.5: 2080 - 2099), for identified landfalling AR dates, (a) the range of positive *MF* anomalies (shading) in each extended winter year (Oct - Mar) and (b) the range of yearly counts (shading). The full range of historical data is shown in grey shading and the full range of RCP 8.5 data is shown in teal shading. The average for each dataset in both panels is shown as a dark grey and dark teal solid line, respectively. In (a) the average peak *MF* in each extended winter (Oct - Mar) is shown as a dark grey and dark teal dashed line, respectively.

their average length. This suggests that the increase in the total number of landfalling dates is related to an increased number of multi-day landfalling events.

Moisture and wind response

We break the change in *MF* due to warming into the response in the moisture field and the response in the wind field. Returning to the criteria we use to define landfalling AR dates, we first look at the change in our percentile based thresholds, noting that we are now focused on the region hugging the coastline, eastward of the box in Fig. 5.2c. Since the thresholds we use to identify ARs are distribution based, the difference in the threshold used for historical simulations and RCP 8.5 can give insight into the response of each of the fields to warming. Figure 5.9 shows the standardized change in the threshold between the two climates. The change in *MF* thresholds over all models shows a large positive shift, consistent with the robust increase in *MF* discussed previously. The similar magnitude of this shift over all models is confirmation of our evaluation in section 5.3, as it indicates similarities in the *MF* distribution of the selected models. Consistent with an increase in atmospheric moisture, we also find a large shift in the *PW* threshold with warming. The threshold for wind speed generally shows a decrease in RCP 8.5 projections. We investigate the change in the 850 hPa meridional and zonal components of the wind using 10 m s^{-1} as a baseline for the historical period. The change in the 850 hPa zonal and meridional baselines are shown in solid and dashed light orange lines, respectively, in Fig. 5.9. All selected models show a decrease in the zonal wind baseline and some degree of increase in

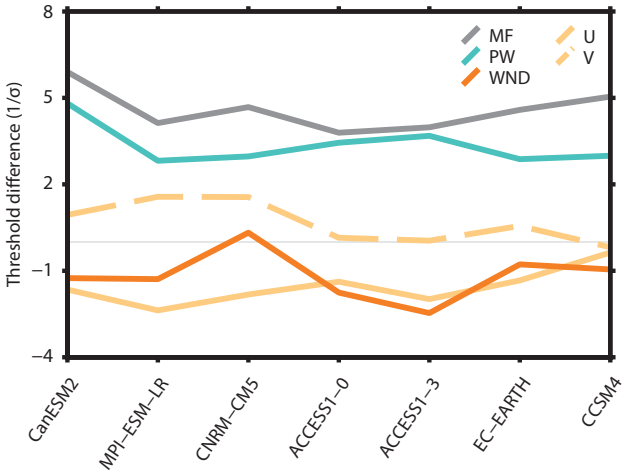

Figure 5.9: For selected models, the standardized difference in thresholds for *MF* (grey solid), *PW* (blue solid), wind speed (dark orange solid), meridional wind (light orange, dashed) and zonal wind (light orange, solid).

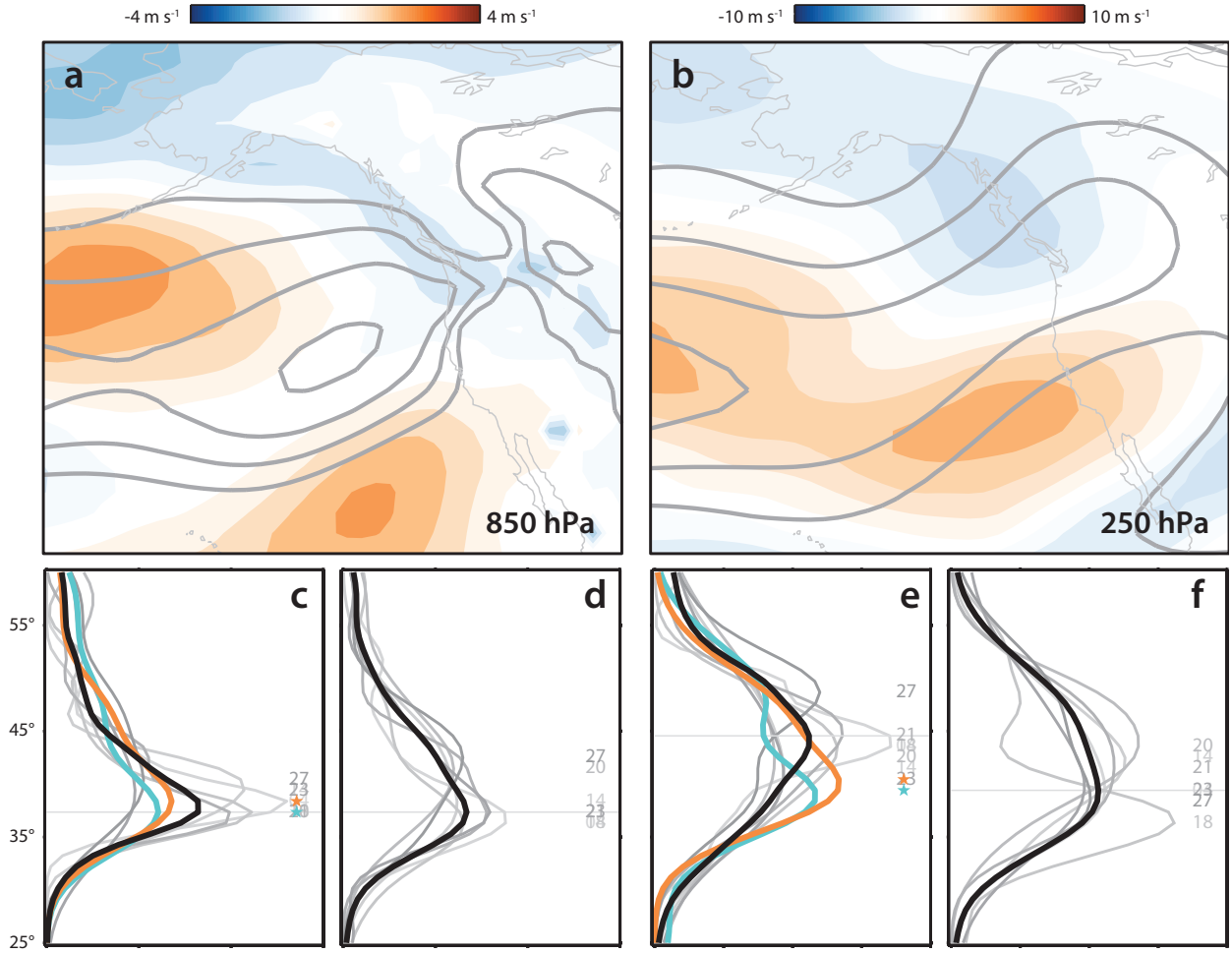

Figure 5.10: (a,b) Difference in the multi-model composite zonal winds at 850- and 250-hPa (shading, RCP 8.5 - historical). For reference, the multi-model zonal wind composite for the historical period is shown in contour (at 850 hPa: intervals of 3 m s^{-1} starting from 3 m s^{-1}, and at 250 hPa: intervals of 10 m s^{-1} starting from 10 m s^{-1}). Probability density functions showing the latitudinal peak in zonal wind anomalies at (c,d) 850 hPa and at (e,f) 250 hPa for (c,e) historical simulations and (d,f) RCP 8.5 projections for the seven selected models (grey lines). The multi-model average is shown in black. For reference, the latitudinal peak in MERRA (blue) and ERA-Interim (orange) are shown in (a,c). The peak of the PDF distribution for each model is marked by the numerical identifier (from Table 5.1).

the meridional wind baseline in projections.

Beginning with a broad overview of the response of the zonal winds to warming, a multi-model composite analysis of the difference between RCP 8.5 projections and historical simulations (shading in Fig. 5.10a) shows a weakening of the 850 hPa zonal wind speed in the jet exit region and a broadening of the jet maximum compared to the historical mean position (contour). A similar pattern is seen in the response of the upper-level jet, where there is an eastward extension of the jet maximum over the central North Pacific and an increase equatorward of the jet core in the eastern North Pacific (Fig. 5.10b). These results are consistent with findings in *Neelin et al.* (2013), who show an eastward extension of the climatological wintertime jet with CMIP5 projections.

We next focus on the variability in the latitude of the jet maximum at 850- and 250-hPa for each dataset (Figs. 5.10c-f). The latitudinal distribution of the zonal winds is shown as probability density functions over all models (grey), compared to the multi-model mean (black). The distributions of MERRA (blue) and ERA-Interim (orange) are shown in the historical panels for comparison. The multi-model average in RCP 8.5 shows a widening of the latitudinal range of peak wind, consistent with the broadening of the lower-level jet maximum seen in Fig. 5.10a. While there is increased variability in the latitudinal position of peak lower-level wind corresponding to AR events between the models in RCP 8.5 compared to historical simulations, there is little change in the mean latitude between the two climates (horizontal grey lines in Fig. 5.10c and Fig. 5.10d). Similar to the results for 850 hPa, Fig. 5.10e and Fig. 5.10f show an increase in the meridional variability of the upper-level jet associated with ARs. Our results are consistent with the pattern of increased meridional variability in the mid-latitude jet identified in *Barnes and Polvani* (2013). We suggest that the pattern of frequency change between the two climates (seen in Fig. 5.7), where we show a broadening of the distribution, is a consequence of a meridionally variable mean state. This is explored in more detail in section 5.4.2.

5.4.2 Dynamical response and decomposition of the moisture flux

In order to investigate the spatial response of *MF* in projections from previous subsection, we approximate the change in *MF* as (*Trenberth and Guillemot*, 1995; *Seager et al.*, 2010):

$$\delta MF \approx g^{-1} \left| \int_{p_s}^{p_t} \left(\overline{\mathbf{V}}\, \delta\overline{q} + \delta\overline{\mathbf{V}}\, \overline{q} + \delta \left(\overline{\mathbf{V}'q'} \right) \right) \mathrm{d}p \right|, \tag{5.6}$$

where,

$$\delta\left(\,\cdot\,\right) = \left(\,\cdot\,\right)_{RCP8.5} - \left(\,\cdot\,\right)_{historical}, \tag{5.7}$$

and where overbars represent averages over all landfalling dates and primes indicate daily anomalies. In Eq. 5.6, the first term describes the thermodynamic response, the second term describes the dynamic response and the third term describes the transient eddy response of *MF* to warming. In Fig. 5.11, we show the thermodynamic response minus the dynamic response in shading, and the transient eddy response in black contours for the selected models. Positive values indicate regions where the thermodynamic component dominates and negative values indicate regions where the dynamic component dominates. The late century RCP 8.5 composite *MF* for landfalling dates is shown in grey contours for each panel. The multi-model ensemble mean is shown in the lower right of the figure.

Much of the change in *MF* is dominated by the thermodynamic response to warming (warm colors in Fig. 5.11), consistent with findings in *Lavers et al.* (2013) and *Warner et al.* (2015). However, in the region dominated by frequency increases in Fig. 5.7, the change in *MF* is largely due to dynamic and transient responses to warming (cool colors and black contours in Fig. 5.11, respectively). The co-location of these two regions supports our conclusions in the previous section that equatorward increases in the lower-level zonal wind play a role in the change in AR distribution in Fig. 5.11. Within the context of the broadening of the frequency distribution from Fig. 5.7 and the variable upper-level jet from Fig. 5.8, we suggest that, while small, the dynamical atmospheric response to warming may

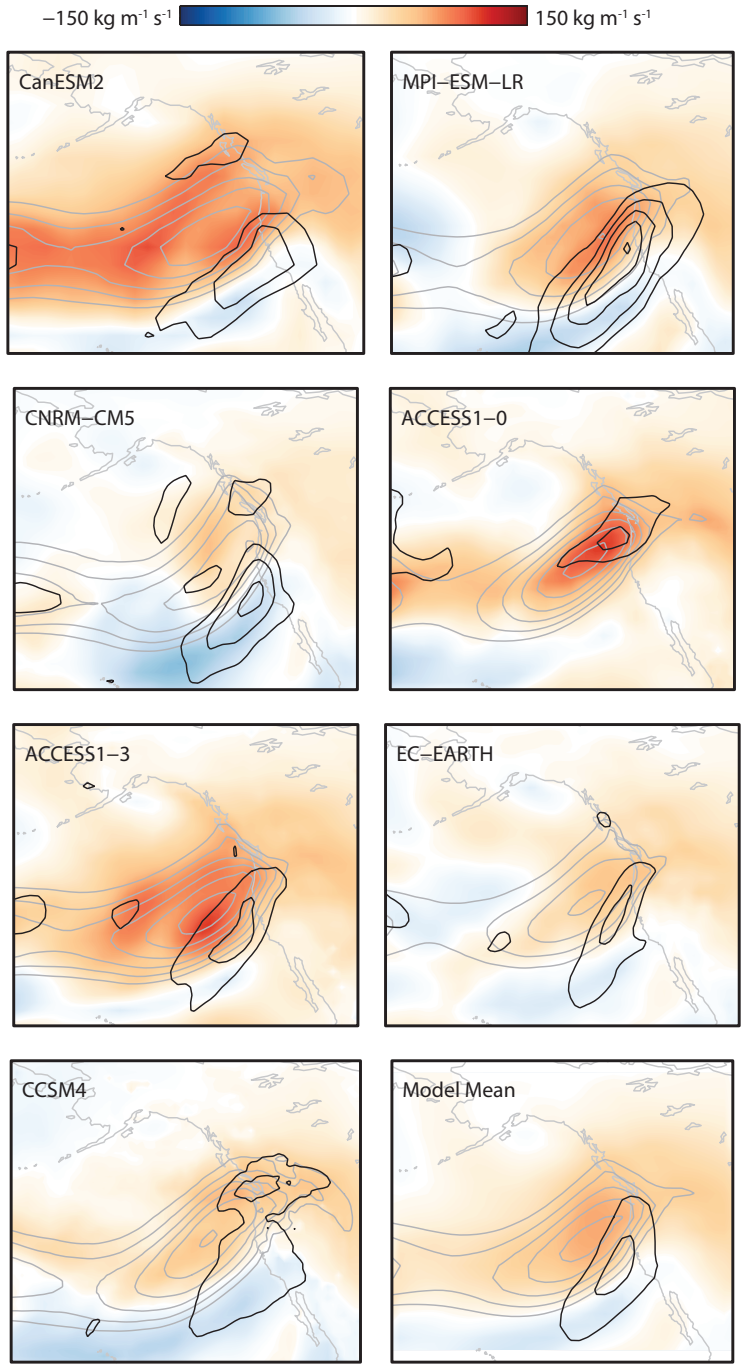

Figure 5.11: The thermodynamic response of MF to warming minus the dynamic response of MF to warming (kg m^{-2} s^{-1}) in shading for each of the selected models (lowest resolution, top left to highest resolution, bottom right). The multi-model mean difference is in the bottom right. The transient eddy response is shown in black contours (intervals of 10 kg m^{-2} s^{-1} starting from 15 kg m^{-2} s^{-1}) and the late century RCP 8.5 composite *MF* for landfalling dates is shown in grey contours (intervals of 50 kg m^{-2} s^{-1} starting from 200 kg m^{-2} s^{-1}).

be important to understanding the response of AR behavior, particularly in determining the latitudinal distribution of landfalling events.

5.5 Conclusions

We present a comprehensive evaluation of CMIP5 model performance in resolving landfalling ARs over the North Pacific basin. While the majority of models evaluated correctly resolved the spatial structure of landfalling ARs, their performance in identifying landfalling dates and in resolving interannual variability in terms of number, amplitude and median latitude varied greatly. Through an evaluation of these characteristics relative to reanalysis, we identify a subset of high performing models for analysis of the response of ARs to warming: CanESM2, MPI-ESM-LR, CNRM-CM5, ACCESS1-0, ACCESS1-3, EC-EARTH and CCSM4.

We extend our investigation to the response of AR behavior to projections under the RCP 8.5 scenario in the 7 high performing models. Comparison of the historical distribution of AR frequency to RCP 8.5 projections shows a broadening of the distribution, particularly apparent equatorward of peak historical frequency. Further investigation of the response of *MF* to warming shows a robust increase in atmospheric moisture, but a decrease in the lower-level zonal winds. Composite analysis shows a broadening of both the 850- and 250-hPa zonal winds equatorward of the historical jet maxima and a slight weakening in the jet exit region, apparent in the multi-model composite of 850 hPa zonal winds. Spatial decomposition of the response of *MF* shows that the thermodynamic response dominates in the peak region of AR frequency, consistent with increases in the atmospheric moisture content. However, we also find that the dynamical response dominates equatorward of the peak in the multi-model composite of *MF* in RCP 8.5.

Our results in section 5.4 support many of the findings in *Dettinger* (2011); *Warner et al.* (2015) about changes in AR landfalling behavior in future climate projections. However, the increased variability of the upper-level jet and broadening of the region of peak AR frequency calls for further analysis into the dynamical response to warming in order to fully characterize potential changes in ARs in late century projections.

Acknowledgments

We thank Wenchang Yang, Graham Simpkins and the three anonymous reviewers for their helpful comments on the manuscript. This research was supported by NSF Grant AGS-1206120 and NSF Grant DGE-1321846. All data used in this research is described in *Rienecker et al.* (2011) and *Dee et al.* (2011).

Chapter 6

Conclusions

The overarching motivation behind this research project was to investigate the large-scale dynamical characteristics of landfalling ARs in the North Pacific. Much of the research prior to this dissertation focused on the synoptic properties and precipitation patterns related to landfalling events. While case-studies and limited duration observational campaigns have laid the foundation to much of our knowledge of these features and their precipitation impacts upon landfall, the large variability associated with these events are poorly understood. Knowledge of the mechanisms modulating AR behavior may inform water management and risk preparedness strategies through improvements in the forecast of landfalling events, particularly in the case of hydrologically significant ARs that may have large socio-economic impacts for populations along the coastline. Advances in characterizing how these significant events change over time will go a long way towards warning and preparedness planning in the region.

6.1 Summary of Results

In Chapter 2, I describe the need for and a comparison of current approaches to AR identification using an instantaneous snapshot of an AR making landfall in March 2005. Use of MF shows clear separation of an AR from the tropical reservoir of moisture, which makes its use in identification schemes preferable to PW alone. The percentile-based thresholding method for MF is investigated and shows no discernible trends over the 36 year period available through reanalysis.

In Chapters 3 and 4, I investigate the landfalling characteristics of present day ARs. The climatological characteristics of landfalling ARs are presented in Chapter 3. The landfalling

latitude of ARs shifts equatorward over the course of the winter season (November through March). The total number of identified AR dates is largest under El Niño conditions and the fewest are found during La Niña conditions. In agreement with previous research, we find that the largest number of AR dates occur during the last three phases of the MJO (phases 6 - 8). To investigate the effect of Rossby wave breaking on AR intensity and development, we focus on a subset of ARs. The strongest ARs are associated with well developed anticyclonic Rossby wave breaking over the eastern North Pacific. This work was among the first to directly associate ARs as distinct features to large-scale dynamics.

In Chapter 4, I focus on the duration of landfalling events and the characteristics of persistent events compared to the climatology of all AR events using a unique dataset in which AR conditions are clustered into spatially and temporally consistent features. This dataset is compared to existing records in the literature and captures up to 98% of recorded events (give a buffer of $\pm$ 2 days). Comparison of the average duration of AR conditions over the eastern North Pacific shows an increase in duration in a persistent subset of 62 events isolated for analysis. Consistent with research connecting persistent events with hydrologically significant impacts on land (e.g. *Ralph et al.*, 2013), we find an overall increase in both intense and average preciptiation. Comparison of persistent landfalling events to the climatology of all landfalling events, we find a possible association with the MJO (phases 3, 6, 7 and 8). However, there are only small differences between the two datasets for ENSO, the PNA and the NAM. Composite analysis of the difference between persistent events and all events shows a deepening of the Aleutian low in association with increased moisture and moisture transport. In association with lower-level characteristics, persistent events are related to well-developed anticyclonic Rossby wave breaking over western North America. Weather regime analysis of daily Z700 anomalies shows AR events are dominated by a PNA-like pattern.

in Chapter 5, I present a comprehensive evaluation of the ability of 28 different CMIP5 models to simulate North Pacific ARs. The intraseasonal and interannual variability of

historical simulations from each model were compared to two different reanalysis datasets (MERRA and ERA-Interim). Agreement between the two reanalysis datasets was excellent, with only a slight differences in the total number of AR dates identified. Model performance was variable and was generally consistent with differences in spatial resolution. A subset of high performing models were isolated and the response of landfalling ARs at the end of the 21^{st} century to warming in RCP 8.5 projections was investigated. The robust increase in atmospheric moisture transport was found to be dominated by a thermodynamic response to warming over much of the region, however, dynamic responses were also found equatorward of the peak AR frequency. While limited to available models, this work has significance for our understanding of the potential response of precipitation patterns associated with landfalling AR events.

6.2 Current and future work

6.2.1 Interaction between moisture transport and large-scale dynamics

The research outlined in this dissertation is limited to observational analysis. While questions on the interactive relationship between large-scale dynamics and moisture transport remain un-addressed within this framework, a modeling study holds promise and is the topic of current work. For this project, we focus on the development of three well-known landfalling events that are among the longest lasting in the dataset used in Chapter 4: 10 - 13 Nov 1990, 31 - 03 Dec 1996/1997 and 16 - 21 Oct 2003. These landfalling events are characteristic of our results in Chapters 3 and 4; composites show perturbations of the upper-level dynamical fields (200 hPa zonal wind and PV) and anticyclonic overturning of PV contours (Fig. 6.1). The motivation of this work is to quantify the interactive relationship between intense moisture transport and upper-level characteristics. Specifically, we are interested in the role this relationship plays in the propagation speed and potential impact of ARs at landfall.

To investigate these three cases, we use the Advanced Research Weather Research and Forecasting (ARW-WRF) model, version 3.7.1 (*Skamarock et al.*, 2005). We use one-way

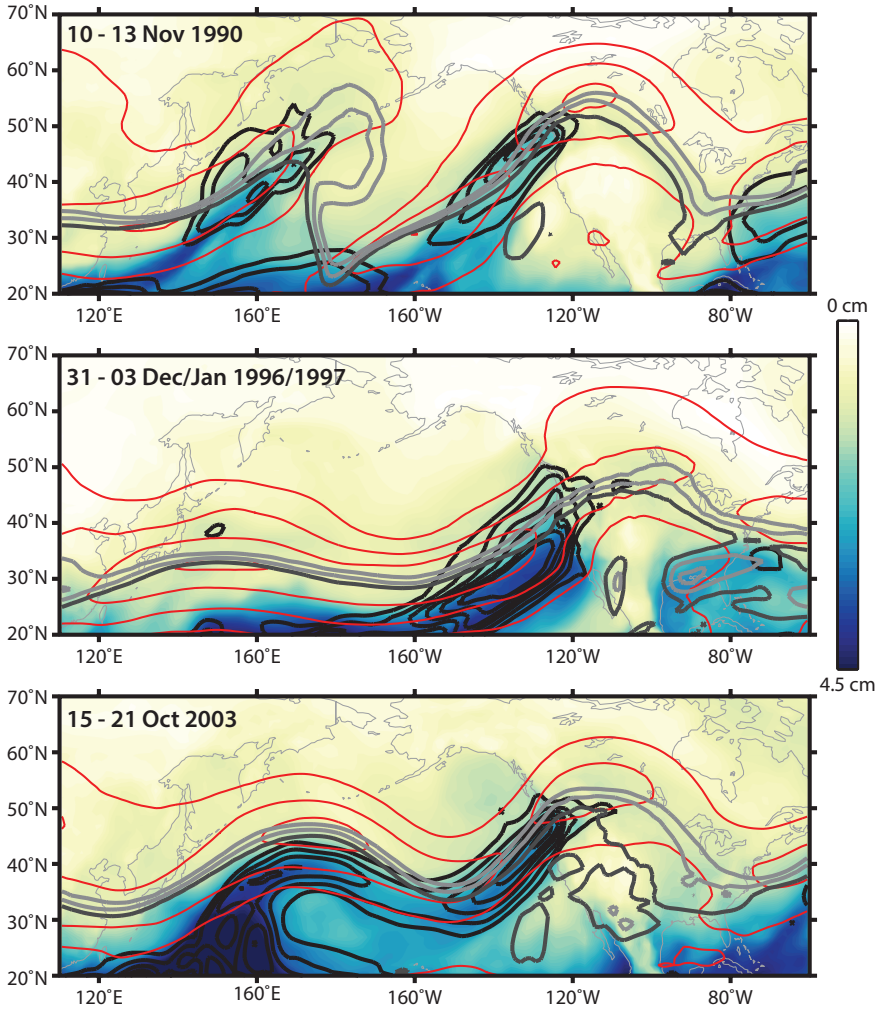

Figure 6.1: Composite of the three events; integrated moisture (shaded), the magnitude of moisture transport (black contour, from 350 kg m^{-1} s^{-1}), 200 hPa zonal wind speed (red contour, from 20 m s^{-1}) and 200 hPa PV (thick black and grey contour, from 2 PVU).

nesting with two domains, a 30-km grid size parent grid and a 10-km grid size nested grid (Fig. 6.2). The simulations are initialized using ERA-Interim reanalysis (*Dee et al.*, 2011), at 0.75° x 0.75° resolution on 6-hrly intervals, and NOAA Optimum Interpolation Sea Surface Temperature (*Reynolds et al.*, 2007), at 0.25° x 0.25° resolution on daily intervals. The model is configured using the WRF Single-Moment 5-class microphysics scheme (*Hong et al.*, 2004), the Mellor-Yamada Nakanishi and Niino Level 2.5 PBL boundary layer scheme (*Nakanishi and Niino*, 2006), the Kain-Fritsch cumulus parameterization scheme (*Kain*, 2004), the Rapid Radiative Transfer Model (RRTM) longwave radiation physics scheme (*Mlawer et al.*,

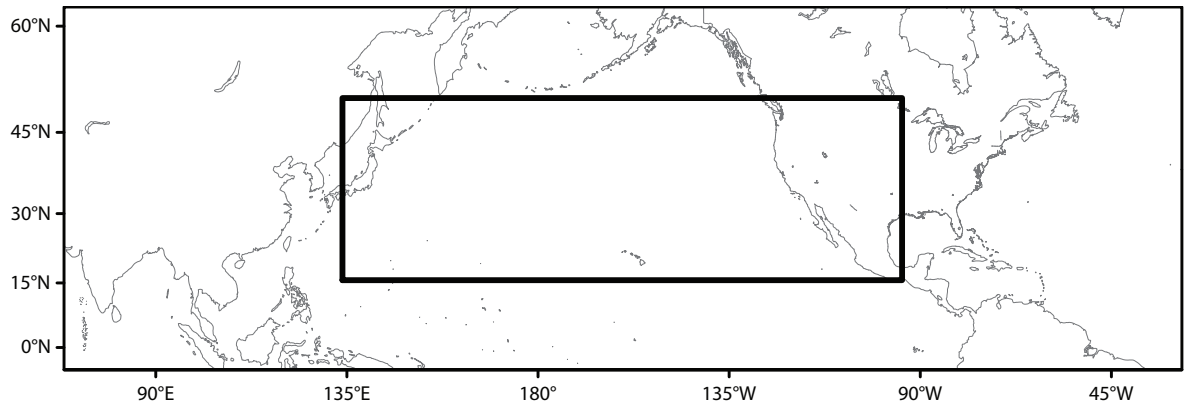

Figure 6.2: WRF model domain with nested grid outlined in black.

1997), the Dudhia shortwave radiation physics scheme (*Dudhia*, 1989), the revised MM5 surface layer scheme (*Jiménez et al.*, 2012), and the unified Noah land surface model (*Chen and Dudhia*, 2001). We allow for four days of model spin-up, during the first 49-hrs of which, we apply grid analysis nudging of the wind-field above the boundary layer in the parent domain. For each of our cases, we run the model for the 8 days prior to and 3 days following landfall in order to look at the development of the event prior to landfall.

Preliminary control simulations show excellent agreement between the development of lower-level moisture transport in ERA-Interim and WRF (Fig. 6.3). Comparison of the two panels in Fig. 6.3 shows approximate similarities in both the intensity and location of the magnitude of moisture flux of the landfalling AR in the eastern North Pacific. Moreover, use of WRF may contribute additional information not immediately apparent in reanalysis. Structures that are only hinted at in the coarser resolution reanalysis, such as the smaller extension poleward of moisture flux around 175°E are found in both panels, but the structure is most apparent in teh control simulation. As the simulations performed in WRF are at much finer scales than what is found in reanalysis, it is possible that these small scale processes may affect the development of ARs. A comprehensive comparison of our simulations to observations is yet to be undertaken.

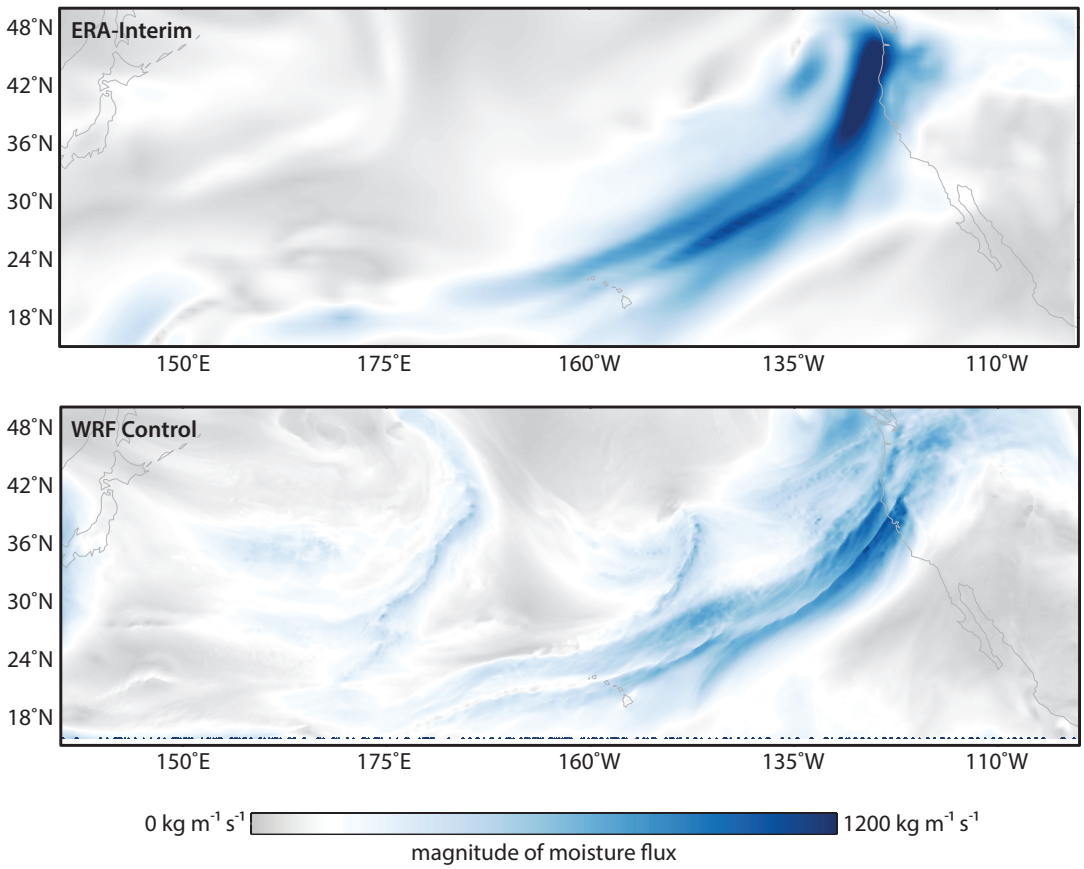

Figure 6.3: Comparison of 00:00 UTC 01 January 1997 in (a) ERA-Interim and (b) WRF.

6.2.2 Extension of investigation over other basins

The focus of much of the research on ARs has been on the North Pacific (e.g. *Ralph et al.*, 2004, 2005; *Neiman et al.*, 2008a; *Dettinger et al.*, 2011; *Ralph et al.*, 2011; *Dettinger*, 2013; *Warner et al.*, 2012; *Rutz et al.*, 2014; *Payne and Magnusdottir*, 2014). There is growing interest in AR activity over the North Atlantic in relation to precipitation over Europe, specifically over United Kingdom and the Iberian peninsula (e.g. *Lavers et al.*, 2012; *Lavers and Villarini*, 2013; *Ramos et al.*, 2015; *Stohl et al.*, 2008). Despite the focus over these two regions, ARs are globally occurring and may have impacts over other regions, such as the western coastline of India and Southeast Asia (e.g. Figs. 3c and 8a in *Guan and Waliser*, 2015) and the western coastline of South America (e.g. *Viale and Nunez*, 2011; *Garreaud*, 2013). Particularly over India and Southeast Asia, little has been done to quantify

the contribution of ARs to regional precipitation patterns. Over this region, it would be interesting to investigate the interaction of ARs with tropical moisture and the monsoon system dynamics.

Bibliography

Abatzoglou, J. T., and G. Magnusdottir (2006), Planetary wave breaking and nonlinear reflection: Seasonal cycle and interannual variability, *Journal of Climate*, *19*, 6139 – 6152, doi:http://dx.doi.org/10.1175/JCLI3968.1.

Anstey, J. A., P. Davini, L. J. Gray, T. J. Woollings, N. Butchart, C. Cagnazzo, B. Christiansen, S. C. Hardiman, S. M. Osprey, and S. Yang (2013), Multi-model analysis of northern hemisphere winter blocking: Model biases and the role of resolution, *Journal of Geophysical Research: Atmospheres*, *118*, 3956 – 3971, doi:10.1002/jgrd.50231.

Bao, J.-W., S. A. Michelson, P. J. Neiman, F. M. Ralph, and J. M. Wilczak (2006), Interpretation of enhanced integrated water vapor bands associated with extratropical cyclones: Their formation and connection to tropical moisture, *Monthly Weather Review*, *134*(4), 1063 – 1080, doi:http://dx.doi.org/10.1175/MWR3123.1.

Barnes, E. A., and L. Polvani (2013), Response of the midlatitude jets, and of their variability, to increased greenhouse gases in the cmip5 models, *Journal of Climate*, *26*, 7117 – 7135, doi:http://dx.doi.org/10.1175/JCLI-D-12-00536.1.

Berg, N., and A. Hall (2015), Increased interannual precipitation extremes over california under climate change, *Journal of Climate*, *28*(16), 6324 – 6334, doi:http://dx.doi.org/10.1175/JCLI-D-14-00624.1.

Browning, K. A. (1990), Organization of cloud and precipitation in extratropical cyclones, in *Extratropical Cyclones: The Erik Palmén Memorial Volume*, edited by C. W. Newton and E. O. Holopainen, American Meteorological Society.

Carlson, T. N. (1991), *Mid-Latitude Weather Systems*, HarperCollins Academic.

Carrera, M. L., R. W. Higgins, and V. E. Kousky (2004), Downstream weather impacts associated with atmospheric blocking over the northeast pacific, *Journal of Climate*, *17*(24), 48234839, doi:http://dx.doi.org/10.1175/JCLI-3237.1.

Cayan, D. R. (1996), Interannual climate variability and snowpack in the western united states, *Journal of Climate*, *9*(5), 928948, doi:http://dx.doi.org/10.1175/1520-0442(1996)009⟨0928:ICVASI⟩2.0.CO;2.

Cayan, D. R., and K. T. Redmond (1994), Enso influences on atmospheric circulation and precipitation in the western united states, in *Tenth Annual Pacific Climate (PACLIM) Workshop*, pp. 2 – 26.

Cayan, D. R., K. T. Redmond, and L. G. Riddle (1999), Enso and hydrologic extremes in the western united states*, *Journal of Climate*, *12*(9), 2881 – 2893, doi:http://dx.doi.org/10.1175/1520-0442(1999)012⟨2881:EAHEIT⟩2.0.CO;2.

Chang, E. K., Y. Guo, and X. Xia (2012), Cmip5 multimodel ensemble projection of storm track change under global warming, *Journal of Geophysical Research: Atmospheres*, *117*(D23118), doi:10.1029/2012JD018578.

Chang, E. K. M., and Y. Fu (2002), Interdecadal variations in northern hemisphere winter storm track intensity, *Journal of Climate*, *15*(6), 642 – 658, doi:http://dx.doi.org/10.1175/1520-0442(2002)015⟨0642:IVINHW⟩2.0.CO;2.

Chen, F., and J. Dudhia (2001), Coupling an advanced land surfacehydrology model with the penn statencar mm5 modeling system. part i: Model implementation and sensitivity, *Monthly Weather Review*, *129*(4), 569 – 585, doi:http://dx.doi.org/10.1175/1520-0493(2001)129⟨0569:CAALSH⟩2.0.CO;2.

Dacre, H. F., P. A. Clark, O. Martinez-Alvarado, M. A. Stringer, and D. A. Lavers (2015), How do atmospheric rivers form?, *Bulletin of the American Meteorological Society*, *96*(8), 1243 – 1255, doi:http://dx.doi.org/10.1175/BAMS-D-14-00031.1.

Dee, D. P., S. M. Uppala, A. J. Simmons, P. Berrisford, P. Poli, S. Kobayashi, U. Andrae, M. A. Balmaseda, G. Balsamo, P. Bauer, P. Bechtold, A. C. M. Beljaars, L. V. de Berg, J. Bidlot, N. Bormann, C. Delsol, R. Dragani, M. Fuentes, A. J. Geer, L. Haimberger, S. B. Healy, H. Hersbach, E. V. Holm, L. Isaksen, P. Kallberg, M. Kohler, M. Matricardi, A. P. McNally, B. M. Monge-Sanz, J.-J. Morcrette., B.-K. Park, C. Peubey, P. de Rosnay, C. Tavolato, J.-N. Thepaut, and F. Vitart (2011), The era-interim reanalysis: Configuration and performance of the data assimilation system, *Quarterly Journal of the Royal Meteorological Society*, *137*(656), 553 – 597, doi:10.1002/qj.828.

Dettinger, M., F. M. Ralph, and D. Lavers (2015), Setting the stage for a global science of atmospheric rivers, *Earth and Space Science News*, *96*, doi::10.1029/2015EO038675.

Dettinger, M. D. (2004), Fifty-two years of "pineapple-express" storms across the west coast of north america, *US Geological Survey, Scripps Institution of Oceanography for the California Energy Commission, PIER Project Rep. CEC-500-2005-004, 20 pp.[Available online at http://www. energy. ca. gov/2005publications/CEC-500-2005-004/CEC-500-2005-004. PDF.]*.

Dettinger, M. D. (2011), Climate change, atmospheric rivers, and floods in california a multimodel analysis of storm frequency and magnitude changes, *Journal of the American Water Resources Association*, *47*(3), 514 – 523, doi:10.1111/j.1752-1688.2011.00546.x.

Dettinger, M. D. (2013), Atmospheric rivers as drought busters on the u.s. west coast, *Journal of Hydrometeorology*, *14*(6), 1721 – 1732, doi:http://dx.doi.org/10.1175/JHM-D-13-02.1.

Dettinger, M. D., D. R. Cayan, H. F. Diaz, and D. M. Meko (1998), Northsouth precipitation patterns in western north america on interannual-to-decadal timescales, *Journal of Climate*, *11*(12), 3095 – 3111, doi:http://dx.doi.org/10.1175/1520-0442(1998)011⟨3095:NSPPIW⟩2.0.CO;2.

Dettinger, M. D., F. M. Ralph, T. Das, P. J. Neiman, and D. R. Cayan (2011), Atmospheric rivers, floods and the water resources of california, *Water*, *3*(2), 445 – 478, doi:10.3390/w3020445.

Dudhia, J. (1989), Numerical study of convection observed during the winter monsoon experiment using a mesoscale two-dimensional model, *Journal of the Atmospheric Sciences*, *46*(20), 30773107, doi:http://dx.doi.org/10.1175/1520-0469(1989)046⟨3077:NSOCOD⟩2.0.CO;2.

Eckhardt, S., A. Stohl, H. Wernli, P. James, C. Forster, and N. Spichtinger (2004), A 15-year climatology of warm conveyor belts, *Journal of Climate*, *17*(1), 218 – 237, doi:http://dx.doi.org/10.1175/1520-0442(2004)017⟨0218:AYCOWC⟩2.0.CO;2.

Ely, L. L., Y. Enzel, and D. R. Cayan (1994), Anomalous north pacific atmospheric circulation and large winter floods in the southwestern united states, *Journal of Climate*, *7*(6), 977987, doi:http://dx.doi.org/10.1175/1520-0442(1994)007⟨0977:ANPACA⟩2.0.CO;2.

Galewsky, J., and A. Sobel (2005), Moist dynamics and orographic precipitation in northern and central california during the new years flood of 1997, *Monthly Weather Review*, *133*(6), 15941612, doi:http://dx.doi.org/10.1175/MWR2943.1.

Garreaud, R. (2013), Warm winter storms in central chile, *Journal of Hydrometeorology*, *14*(5), 15151534, doi:http://dx.doi.org/10.1175/JHM-D-12-0135.1.

Gleckler, P., K. Taylor, and C. Doutriaux (2008), Performance metrics for climate models, *Journal of Geophysical Research*, *113*(D06104), doi:10.1029/2007JD008972.

Guan, B., and D. E. Waliser (2015), Detection of atmospheric rivers; evaluation and application of an algorithm for global studies, *Journal of Geophysical Research: Atmospheres*, *120*(12), 514 – 535, doi:10.1002/2015JD024257.

Guan, B., N. P. Molotch, D. E. Waliser, E. J. Fetzer, and P. J. Neiman (2010), Extreme snowfall events linked to atmospheric rivers and surface air temperature via satellite measurements, *Geophysical Research Letters*, *37*(L20401), doi:10.1029/2010GL044696.

Guan, B., D. E. Waliser, N. P. Molotch, E. J. Fetzer, and P. J. Neiman (2012), Does the maddenjulian oscillation influence wintertime atmospheric rivers and snowpack in the sierra nevada?, *Monthly Weather Review*, *140*(2), 325 – 342, doi:http://dx.doi.org/10.1175/MWR-D-11-00087.1.

Guan, B., N. P. Molotch, D. E. Waliser, E. J. Fetzer, and P. J. Neiman (2013), The 2010/2011 snow season in california's sierra nevada: Role of atmospheric rivers and modes of large-scale variability, *Water Resource Research*, *49*, 6731 6743, doi:10.1002/wrcr.20537.

Hagos, S., L. R. Leung, Q. Yang, C. Zhao, and J. Lu (2015), Resolution and dynamical core dependence of atmospheric river frequency in global model simulations, *Journal of Climate*, *28*(7), 2764 – 2776, doi:http://dx.doi.org/10.1175/JCLI-D-14-00567.1.

Held, I. M., and B. J. Soden (2006), Robust responses of the hydrological cycle to global warming, *Journal of Climate*, *19*(21), 5686 – 5699, doi:http://dx.doi.org/10.1175/JCLI3990.1.

Higgins, R. W., J.-K. E. Schemm, W. Shi, and A. Leetmaa (2000), Extreme precipitation events in the western united states related to tropical forcing, *Journal of Climate*, *13*(4), 793 – 820, doi:http://dx.doi.org/10.1175/1520-0442(2000)013⟨0793:EPEITW⟩2.0.CO;2.

Higgins, R. W., V. B. S. Silva, W. Shi, and J. Larson (2007), Relationships between climate variability and fluctuations in daily precipitation over the united states, *Journal of Climate*, *20*(14), 35613579, doi:http://dx.doi.org/10.1175/JCLI4196.1.

Hong, S.-Y., J. Dudhia, and S.-H. Chen (2004), A revised approach to ice microphysical processes for the bulk parameterization of clouds and precipitation, *Monthly Weather Review*, *132*(1), 103 – 120, doi:http://dx.doi.org/10.1175/1520-0493(2004)132⟨0103:ARATIM⟩2.0.CO;2.

Hoskins, B. J., and P. J. Valdes (1990), On the existence of storm-tracks, *Journal of the Atmospheric Sciences*, *47*(15), 1854 – 1864, doi:http://dx.doi.org/10.1175/1520-0469(1990)047⟨1854:OTEOST⟩2.0.CO;2.

Jiang, T., and Y. Deng (2011), Downstream modulation of north pacific atmospheric river activity by east asian cold surges, *Geophysical Research Letters*, *38*, doi:10.1029/2011GL049462.

Jiang, T., K. J. Evans, Y. Deng, and X. Dong (2014), Intermediate frequency atmospheric disturbances: A dynamical bridge connecting western u. s. extreme precipitation with east asian cold surges, *Journal of Geophysical Research: Atmospheres*, *119*, 3723 – 3735, doi:10.1002/2013JD021209.

Jiménez, P. A., J. Dudhia, J. F. González-Rouco, J. Navarro, J. P. Montávez, and E. García-Bustamante (2012), A revised scheme for the wrf surface layer formulation, *Monthly Weather Review*, *140*(3), 898918, doi:http://dx.doi.org/10.1175/MWR-D-11-00056.1.

Jones, C. (2000), Occurrence of extreme precipitation events in california and relationships with the maddenjulian oscillation, *Journal of Climate*, *13*(20), 3576 – 3587, doi:http://dx.doi.org/10.1175/1520-0442(2000)013⟨3576:OOEPEI⟩2.0.CO;2.

Kain, J. S. (2004), The kain-fritsch convective parameterization: An update, *Journal of Applied Meteorology*, *43*(1), 170181, doi:http://dx.doi.org/10.1175/1520-0450(2004)043⟨0170:TKCPAU⟩2.0.CO;2.

Kimoto, M., and M. Ghil (1993), Multiple flow regimes in the northern hemisphere winter. part ii: Sectorial regimes and preferred transitions, *Journal of the Atmospheric Sciences*, *50*(16), 26452673, doi:http://dx.doi.org/10.1175/1520-0469(1993)050⟨2645:MFRITN⟩2.0.CO;2.

Knippertz, P., and H. Wernli (2010), A lagrangian climatology of tropical moisture exports to the northern hemispheric extratropics, *Journal of Climate*, *23*(4), 987 – 1003, doi: http://dx.doi.org/10.1175/2009JCLI3333.1.

Knippertz, P., H. Wernli, and G. Gl$\acute{}$aser (2013), A global climatology of tropical moisture exports, *Journal of Climate*, *26*(10), 3031 – 3045, doi:http://dx.doi.org/10.1175/JCLI-D-12-00401.1.

Lavers, D. A., and G. Villarini (2013), The nexus between atmospheric rivers and extreme preciptiation accross europe, *Geophysical Research Letters*, *40*(12), 32593264, doi:10.1002/grl.50636.

Lavers, D. A., G. Villarini, R. P. Allan, E. F. Wood, and A. J. Wade (2012), The detection of atmospheric rivers in atmospheric reanalyses and their links to british winter floods and the large-scale climatic circulation, *Journal of Geophysical Research: Atmospheres*, *117*(D20106), doi:10.1029/2012JD018027.

Lavers, D. A., R. P. Allan, G. Villarini, B. Lloyd-Hughes, D. J. Brayshaw, and A. J. Wade (2013), Future changes in atmospheric rivers and their implications for winter flooding in britain, *Environmental Research Letters*, *13*(3), doi:http://dx.doi.org/10.1088/1748-9326/8/3/034010.

Lavers, D. A., F. M. Ralph, D. E. Waliser, A. Gershunov, and M. D. Dettinger (2015), Climate change intensification of horizontal water vapor transport in cmip5, *Geophysical Research Letters*, *42*(13), 5617 – 5625, doi:10.1002/2015GL064672.

Legras, B., and M. Ghil (1985), Persistent anomalies, blocking and variations in atmospheric predictability, *Journal of the Atmospheric Sciences*, *42*(5), 433471, doi:http://dx.doi.org/10.1175/1520-0469(1985)042⟨0433:PABAVI⟩2.0.CO;2.

Leung, L. R., and Y. Qian (2009), Atmospheric rivers induced heavy precipitation and flooding in the western u.s. simulated by the wrf regional climate model, *Geophysical Research Letters*, *36*(L03820), doi:10.1029/2008GL036445.

Liu, C., and E. A. Barnes (2015), Extreme moisture transport into the arctic linked to rossby wave breaking, *Journal of Geophysical Research: Atmospheres*, *120*(9), 3774 – 3788, doi:10.1002/2014JD022796.

Lynott, R. E., and O. P. Cramer (1966), Detailed analysis of the 1962 columbus day windswind in oregon and washington, *Monthly Weather Review*, *94*(2), 105 – 117, doi:http://dx.doi.org/10.1175/1520-0493(1966)094⟨0105:DAOTCD⟩2.3.CO;2.

Madden, R. A., and P. R. Julian (1972), Description of global-scale circulation cells in the tropics with a 4050 day period, *Journal of the Atmospheric Sciences*, *29*(6), 1109–1123, doi:http://dx.doi.org/10.1175/1520-0469(1972)029⟨1109:DOGSCC⟩2.0.CO;2.

Madonna, E., H. Wernli, H. Joos, and O. Martius (2014), Warm conveyor belts in the era-interim dataset (19792010). part i: Climatology and potential vorticity evolution, *Journal of Climate*, *27*(1), 3 – 26, doi:http://dx.doi.org/10.1175/JCLI-D-12-00720.1.

McAfee, S. A., and J. L. Russell (2008), Northern annular mode impact on spring climate in the western united states, *Geophysical Research Letters*, *35*(17), doi:10.1029/2008GL034828.

McIntyre, M. E., and T. N. Palmer (1983), Breaking planetary waves in the stratosphere, *Nature*, *305*, 593 – 600, doi:10.1038/305593a0.

Meehl, G. A., et al. (2007), Global climate projections, in *Climate Change 2007: The Physical Science Basis: Contributions of Working Group I to the Fourth Assessment Report of the Intergovernmental Panel on Climate Change*, edited by S. Solomon et al., pp. 747 – 845, Cambridge University Press.

Michelangeli, P.-A., R. Vautard, and B. Legras (1995), Weather regimes: Recurrence and quasi stationarity, *Journal of the Atmospheric Sciences*, *52*(8), 12371256, doi:http://dx.doi.org/10.1175/1520-0469(1995)052⟨1237:WRRAQS⟩2.0.CO;2.

Mitchell, T. P., and W. Blier (1997), The variability of wintertime precipitation in the region of california, *Journal of Climate*, *10*(9), 2261 – 2276, doi:http://dx.doi.org/10.1175/1520-0442(1997)010⟨2261:TVOWPI⟩2.0.CO;2.

Mlawer, E. J., S. J. Taubman, P. D. Brown, M. J. Iacono, and S. A. Clough (1997), Radiative transfer for inhomogeneous atmospheres: Rrtm, a validated correlated-k model for the longwave, *Journal of Geophysical Research: Atmospheres*, *102*(D14), 16,663 – 16,682, doi:10.1029/97JD00237.

Mo, K. C., and R. W. Higgins (1998a), Tropical convection and precipitation regimes in the western united states, *Journal of Climate*, *11*(9), 2404 – 2423, doi:http://dx.doi.org/10.1175/1520-0442(1998)011⟨2404:TCAPRI⟩2.0.CO;2.

Mo, K. C., and R. W. Higgins (1998b), Tropical influences on california precipitation, *Journal of Climate*, *11*(3), 412 – 430, doi:http://dx.doi.org/10.1175/1520-0442(1998)011⟨0412:TIOCP⟩2.0.CO;2.

Moore, B. J., P. J. Neiman, F. M. Ralph, and F. E. Barthold (2012), Physical processes associated with heavy flooding rainfall in nashville, tennessee, and vicinity during 12 may 2010: The role of an atmospheric river and mesoscale convective systems*, *Monthly Weather Review*, *140*(2), 358378, doi:http://dx.doi.org/10.1175/MWR-D-11-00126.1.

Nakanishi, M., and H. Niino (2006), An improved melloryamada level-3 model: Its numerical stability and application to a regional prediction of advection fog, *Boundary-Layer Meteorology*, *119*(2), 397 – 407, doi:10.1007/s10546-005-9030-8.

Nayak, M. A., G. Villarini, and D. A. Lavers (2014), On the skill of numerical weather prediction models to forecast atmospheric rivers over the central united states, *Geophysical Research Letters*, *41*(12), 4354 – 4362, doi:10.1002/2014GL060299.

Neelin, J. D., B. Langenbrunner, J. E. Meyerson, A. Hall, and N. Berg (2013), California winter precipitation change under global warming in the coupled model intercomparison

project phase 5 ensemble, *Journal of Climate*, *26*(17), 6238 – 6256, doi:http://dx.doi.org/10.1175/JCLI-D-12-00514.1.

Neiman, P. J., F. M. Ralph, G. A. Wick, J. D. Lundquist, and M. D. Dettinger (2008a), Meteorological characteristics and overland precipitation impacts of atmospheric rivers affecting the west coast of north america based on eight years of ssm/i satellite observations, *Journal of Hydrometeorology*, *9*(1), 22 – 47, doi:http://dx.doi.org/10.1175/2007JHM855.1.

Neiman, P. J., F. M. Ralph, G. A. Wick, Y.-H. Kuo, T.-K. Wee, Z. Ma, G. H. Taylor, and M. D. Dettinger (2008b), Diagnosis of an intense atmospheric river impacting the pacific northwest: Storm summary and offshore vertical structure observed with cosmic satellite retrievals, *Monthly Weather Review*, *136*(11), 4398 – 4420, doi:http://dx.doi.org/10.1175/2008MWR2550.1.

Neiman, P. J., A. B. White, F. M. Ralph, D. J. Gottas, and S. I. Gutman (2009), A water vapor flux tool for precipitation forecasting, *Proceedings of the Institution of Civil Engineers - Water Management*, *162*(2), 83 – 94, doi:10.1680/wama.2009.162.2.83.

Neiman, P. J., L. J. Schick, F. M. Ralph, M. Hughes, and G. A. Wick (2011), Flooding in western washington: The connection to atmospheric rivers*, *Journal of Hydrometeorology*, *12*(6), 1337 – 1358, doi:http://dx.doi.org/10.1175/2011JHM1358.1.

Neiman, P. J., F. M. Ralph, B. J. Moore, M. Hughes, K. M. Mahoney, J. M. Cordeira, and M. D. Dettinger (2013), The landfall and inland penetration of a flood-producing atmospheric river in arizona. part i: Observed synoptic-scale, orographic, and hydrometeorological characteristics, *Journal of Hydrometeorology*, *14*(2), 460 – 484, doi:http://dx.doi.org/10.1175/JHM-D-12-0101.1.

Newell, R. E., and Y. Zhu (1994), Tropospheric rivers: A one-year record and a possible application to ice core data, *Geophysical Research Letters*, *21*(2), 113 – 116, doi:10.1029/93GL03113.

Newell, R. E., N. E. Newell, Y. Zhu, and C. Scott (1992), Tropospheric rivers? a pilot study, *Geophysical Research Letters*, *19*(24), 2401 – 2404, doi:10.1029/92GL02916.

Newman, M., G. N. Kiladis, K. M. Weickmann, F. M. Ralph, and P. D. Sardeshmukh (2012), Relative contributions of synoptic and low-frequency eddies to time-mean atmospheric moisture transport, including the role of atmospheric rivers, *Journal of Climate*, *25*(21), 7341 – 7361, doi:http://dx.doi.org/10.1175/JCLI-D-11-00665.1.

O'Gorman, P. A. (2015), Precipitation extremes under climate change, *Current Climate Change Reports*, *1*(2), 49 – 59, doi:10.1007/s40641-015-0009-3.

OWSC (), January 2009 flooding.

Pandey, G. R., D. R. Cayan, and K. P. Georgakakos (1999), Precipitation structure in the sierra nevada of california during winter, *Journal of Geophysical Research: Atmospheres*, *104*(D10), 12,019 – 12,030, doi:10.1029/1999JD900103.

Payne, A. E., and G. Magnusdottir (2014), Dynamics of landfalling atmospheric rivers over the north pacific in 30 years of merra reanalysis, *Journal of Climate*, *27*(18), 7133 – 7150, doi:http://dx.doi.org/10.1175/JCLI-D-14-00034.1.

Payne, A. E., and G. Magnusdottir (2015), An evaluation of atmospheric rivers over the north pacific in cmip5 and their response to warming under rcp 8.5, *Journal of Geophysical Research: Atmospheres*, *120*(21), 11,173 – 11,190, doi:10.1002/2015JD023586.

Pfahl, S., E. Madonna, M. Boettcher, H. Joos, and H. Wernli (2014), Warm conveyor belts in the era-interim dataset (19792010). part ii: Moisture origin and relevance for precipitation, *Journal of Climate*, *27*(1), 27 – 40, doi:http://dx.doi.org/10.1175/JCLI-D-13-00223.1.

Pierce, D. W., D. R. Cayan, T. Das, E. P. Maurer, N. L. Miller, Y. Bao, M. Kanamitsu, K. Yoshimura, M. A. Snyder, L. C. Sloan, G. Franco, and M. Tyree (2013), The key role of heavy precipitation events in climate model disagreements of future annual preciptiation changes in california, *Journal of Climate*, *26*, 5879 – 5896, doi:http://dx.doi.org/10.1175/JCLI-D-12-00766.1.

Ralph, F., P. J. Neiman, G. A. Wick, S. I. Gutman, M. D. Dettinger, D. R. Cayan, and A. B. White (2006), Flooding on california's russian river: Role of atmospheric rivers, *Geophysical Research Letters*, *33*(L13801), doi:10.1029/2006GL026689.

Ralph, F. M., and M. D. Dettinger (2011), Storms, floods and the science of atmospheric rivers, *EOS, Transactions American Geophysical Union*, *92*(32), 265 – 266, doi:10.1029/2011EO320001.

Ralph, F. M., and M. D. Dettinger (2012), Historical and national perspectives on extreme west coast precipitation associated with atmospheric rivers during december 2010, *Bulletin of the American Meteorological Society*, *93*(6), 783 – 790, doi:http://dx.doi.org/10.1175/BAMS-D-11-00188.1.

Ralph, F. M., P. J. Neiman, D. E. Kingsmill, P. O. G. Persson, A. B. White, E. T. Strem, E. D. Andrews, and R. C. Antweiler (2003), The impact of a prominent rain shadow on flooding in california's santa cruz mountains: A caljet case study and sensitivity to the enso cycle, *Journal of Hydrometeorology*, *4*(6), 1243 – 1264, doi:http://dx.doi.org/10.1175/1525-7541(2003)004⟨1243:TIOAPR⟩2.0.CO;2.

Ralph, F. M., P. J. Neiman, and G. A. Wick (2004), Satellite and caljet aircraft observations of atmospheric rivers over the eastern north pacific ocean during the winter of 1997/98, *Monthly Weather Review*, *132*(7), 1721 – 1745, doi:http://dx.doi.org/10.1175/1520-0493(2004)132⟨1721:SACAOO⟩2.0.CO;2.

Ralph, F. M., P. J. Neiman, and R. Rotunno (2005), Dropsonde observations in low-level jets over the northeastern pacific ocean from caljet-1998 and pacjet-2001: Mean vertical-profile and atmospheric-river characteristics, *Monthly Weather Review*, *133*(4), 889 – 910, doi:http://dx.doi.org/10.1175/MWR2896.1.

Ralph, F. M., E. Sukovich, D. Reynolds, M. Dettinger, S. Weagle, W. Clark, and P. J. Neiman (2010), Assessment of extreme quantitative precipitation forecasts and development of regional extreme event thresholds using data from hmt-2006 and coop observers, *Journal of Hydrometeorology*, *11*(6), 1286 – 1304, doi:http://dx.doi.org/10.1175/2010JHM1232.1.

Ralph, F. M., P. J. Neiman, G. N. Kiladis, K. Weickmann, and D. W. Reynolds (2011), A multiscale observational case study of a pacific atmospheric river exhibiting tropicalextra-tropical connections and a mesoscale frontal wave, *Monthly Weather Review*, *139*(4), 1169 – 1189, doi:http://dx.doi.org/10.1175/2010MWR3596.1.

Ralph, F. M., T. Coleman, P. J. Neiman, R. J. Zamora, and M. D. Dettinger (2013), Observed impacts of duration and seasonality of atmospheric-river landfalls on soil moisture and runoff in coastal northern california, *Journal of Hydrometeorology*, *14*(2), 443 – 459, doi: http://dx.doi.org/10.1175/JHM-D-12-076.1.

Ramos, A. M., N. Cortesi, and R. M. Trigo (2014), Circulation weather types and spatial variability of daily precipitation in the iberian peninsula, *Frontiers in Earth Science*, *2*(25), doi:10.3389/feart.2014.00025.

Ramos, A. M., R. M. Trigo, M. L. R. Liberato, and R. Tomé (2015), Daily precipitation extreme events in the iberian peninsula and its association with atmospheric rivers, *Journal of Hydrometeorology*, *16*, 579 – 597, doi:10.1175/JHM-D-14-0103.1.

Reeves, H. D., Y.-L. Lin, and R. Rotunno (2008), Dynamic forcing and mesoscale variability of heavy precipitation events over the sierra nevada mountains, *Monthly Weather Review*, *136*(1), doi:http://dx.doi.org/10.1175/2007MWR2164.1.

Reinhold, B. B., and R. T. Pierrehumbert (1982), Dynamics of weather regimes: Quasi-stationary waves and blocking, *Monthly Weather Review*, *110*(9), 11051145, doi:http:// dx.doi.org/10.1175/1520-0493(1982)110⟨1105:DOWRQS⟩2.0.CO;2.

Reynolds, R. W., T. M. Smith, C. Liu, D. B. Chelton, K. S. Casey, and M. G. Schlax (2007), Daily high-resolution-blended analyses for sea surface temperature, *Journal of Climate*, *20*(22), 54735496, doi:http://dx.doi.org/10.1175/2007JCLI1824.1.

Rienecker, M. M., M. J. Suarez, R. Gelaro, R. Todling, J. Bacmeister, E. Liu, M. G. Bosilovich, S. D. Schubert, L. Takacs, G.-K. Kim, S. Bloom, J. Chen, D. Collins, A. Conaty, A. da Silva, W. Gu, J. Joiner, R. D. Koster, R. Lucchesi, A. Molod, T. Owens, S. Pawson, P. Pegion, C. R. Redder, R. Reichle, F. R. Robertson, A. G. Ruddick, M. Sienkiewicz, and J. Woollen (2011), Merra: Nasas modern-era retrospective analysis for research and applications, *Journal of Climate*, *24*(14), 3624 – 3648, doi: http://dx.doi.org/10.1175/JCLI-D-11-00015.1.

Rivera, E. R., F. Dominguez, and C. L. Castro (2014), Atmospheric rivers and cool season extreme precipitation events in the verde river basin of arizona, *Journal of Hydrometeorology*, *15*(2), 813 – 829, doi:http://dx.doi.org/10.1175/JHM-D-12-0189.1.

Rivière, G. (2010), Role of rossby wave breaking in the west pacific teleconnection, *Geophysical Research Letters*, *37*(L11802), doi:10.1029/2010GL043309.

Robertson, A. W., and M. Ghil (1999), Large-scale weather regimes and local climate over the western united states, *Journal of Climate*, *12*(6), 17961813, doi:http://dx.doi.org/10.1175/1520-0442(1999)012⟨1796:LSWRAL⟩2.0.CO;2.

Ropelewski, C. F., and M. S. Halpert (1987), Global and regional scale precipitation patterns associated with the el niño/southern oscillation, *Monthly Weather Review*, *115*(8), 1606 – 1626, doi:http://dx.doi.org/10.1175/1520-0493(1987)115⟨1606:GARSPP⟩2.0.CO;2.

Russo, T. A., A. T. Fisher, and D. M. Winslow (2013), Regional and local increases in storm intensity in the san francisco bay area, usa, between 1980 and 2010, *Journal of Geophysical Research: Atmospheres*, *118*, 3392 – 3401, doi:10.1002/jgrd.50225.

Rutz, J. J., and W. J. Steenburgh (2012), Quantifying the role of atmospheric rivers in the interior western united states, *Atmospheric Science Letters*, *13*(4), 257 – 261, doi:10.1002/asl.392.

Rutz, J. J., W. J. Steenburgh, and F. M. Ralph (2014), Climatological characteristics of atmospheric rivers and their inland penetration over the western united states, *Monthly Weather Review*, *142*(2), 905 –921, doi:http://dx.doi.org/10.1175/MWR-D-13-00168.1.

Ryoo, J.-M., Y. Kaspi, D. W. Waugh, G. N. Kiladis, D. E. Waliser, E. J. Fetzer, and J. Kim (2013), Impact of rossby wave breaking on u.s. west coast winter precipitation during enso events, *Journal of Climate*, *26*(17), 6360 – 6382, doi:http://dx.doi.org/10.1175/JCLI-D-12-00297.1.

Ryoo, J.-M., D. E. Waliser, D. W. Waugh, S. Wong, E. J. Fetzer, and I. Fung (2015), Classification of atmospheric river events on the u.s. west coast using a trajectory model, *Journal of Geophysical Research: Atmospheres*, *120*, 3007 – 3028, doi:10.1002/2014JD022023.

Seager, R., N. Naik, and G. A. Vecchi (2010), Thermodynamic and dynamic mechanisms for large-scale changes in the hydrological cycle in response to global warming*, *Journal of Climate*, *23*(17), 4651 – 4668, doi:http://dx.doi.org/10.1175/2010JCLI3655.1.

Skamarock, W. C., J. B. Klemp, J. Dudhia, D. O. Gill, D. M. Barker, W. Wang, and J. G. Powers (2005), A description of the advanced research wrf version 2, *Tech. rep.*, NCAR.

Smith, B. L., S. E. Yuter, P. J. Neiman, , and D. E. Kingsmill (2010), Water vapor fluxes and orographic precipitation over northern california associated with a landfalling atmospheric river, *Monthly Weather Review*, *138*(1), 74 – 100, doi:http://dx.doi.org/10.1175/2009MWR2939.1.

Smyth, P., K. Ide, and M. Ghil (1999), Multiple regimes in northern hemisphere height fields via mixture model clustering*, *Journal of the Atmospheric Sciences*, *56*(21), 37043723, doi:http://dx.doi.org/10.1175/1520-0469(1999)056⟨3704:MRINHH⟩2.0.CO;2.

Sodemann, H., and A. Stohl (2013), Moisture origin and meridional transport in atmospheric rivers and their association with multiple cyclones*, *Monthly Weather Review*, *141*(8), 2850 – 2868, doi:http://dx.doi.org/10.1175/MWR-D-12-00256.1.

Stohl, A., C. Forster, and H. Sodemann (2008), Remote sources of water vapor forming precipitation on the norwegian west coast at 60°na tale of hurricanes and an atmospheric river, *Journal of Geophysical Research: Atmospheres*, *113*(D05102), doi:10.1029/2007JD009006.

Strong, C., and G. Magnusdottir (2008a), Tropospheric rossby wave breaking and the nao/nam, *Journal of the Atmospheric Sciences*, *65*(9), 2861 – 2876, doi:http://dx.doi.org/10.1175/2008JAS2632.1.

Strong, C., and G. Magnusdottir (2008b), How rossby wave breaking over the pacific forces the north atlantic oscillation, *Geophysical Research Letters*, *35*(10), 1 – 5, doi:10.1029/2008GL033578.

Taylor, K. E. (2001), Summarizing multiple aspects of model performance in a single diagram, *Journal of Geophysical Research*, *106*(D7), 7183 – 7192, doi:10.1029/2000JD900719.

Taylor, K. E., R. J. Stouffer, and G. A. Meehl (2012), An overview of cmip5 and the experiment design, *Bulletin of the American Meteorological Society*, *93*(4), 485 – 498, doi:http://dx.doi.org/10.1175/BAMS-D-11-00094.1.

Trenberth, K. E., and C. J. Guillemot (1995), Evaluation of the global atmospheric moisture budget as seen from analyses, *Journal of Climate*, *8*(9), 2255 – 2272, doi:http://dx.doi.org/10.1175/1520-0442(1995)008⟨2255:EOTGAM⟩2.0.CO;2.

Viale, M., and M. N. Nunez (2011), Climatology of winter orographic precipitation over the subtropical central andes and associated synoptic and regional characteristics, *Journal of Hydrometeorology*, *12*(4), 481507, doi:http://dx.doi.org/10.1175/2010JHM1284.1.

Warner, M. D., C. F. Mass, and E. P. S. Jr. (2012), Wintertime extreme precipitation events along the pacific northwest coast: Climatology and synoptic evolution, *Monthly Weather Review*, *140*(7), 2021 – 2043, doi:http://dx.doi.org/10.1175/MWR-D-11-00197.1.

Warner, M. E., C. F. Mass, and E. P. S. Jr. (2015), Changes in winter atmospheric rivers along the north american west coast in cmip5 climate models, *Journal of Hydrometeorology*, *16*(1), 118 – 128, doi:http://dx.doi.org/10.1175/JHM-D-14-0080.1.

Wheeler, M. C., and H. H. Hendon (2004), An all-season real-time multivariate mjo index: Development of an index for monitoring and prediction, *Monthly Weather Review*, *132*(8), 1917 – 1932, doi:http://dx.doi.org/10.1175/1520-0493(2004)132⟨1917:AARMMI⟩2.0.CO;2.

Wick, G. A., P. J. Neiman, F. M. Ralph, and T. M. Hamill (2013a), Evaluation of forecasts of the water vapor signature of atmospheric rivers in operational numerical weather prediction models, *Weather and Forecasting*, *28*(6), 1337 – 1352, doi:http://dx.doi.org/10.1175/WAF-D-13-00025.1.

Wick, G. A., P. J. Neiman, and F. M. Ralph (2013b), Description and validation of an automated objective technique for identification and characterization of the integrated water vapor signature of atmospheric rivers, *Geoscience and Remote Sensing, IEEE Transactions*, *51*(4), 2166 – 2176, doi:10.1109/TGRS.2012.2211024.

Williams, A. P., R. Seager, J. T. Abatzoglou, B. I. Cook, J. E. Smerdon, and E. R. Cook (2015), Contribution of anthropogenic warming to california drought during 2012 - 2014, *Geophysical Research Letters*, *42*, 6819 – 6828, doi:10.1002/2015GL064924.

Wolter, K., and M. S. Timlin (1998), Measuring the strength of enso events: How does 1997/98 rank?, *Weather*, *53*(9), 315 – 324, doi:10.1002/j.1477-8696.1998.tb06408.x.

Yin, J. H. (2005), A consistent poleward shift of the storm tracks in simulations of 21st century climate, *Geophysical Research Letters*, *32*(L18701), doi:10.1029/2005GL023684.

Yiou, P., R. Vautard, P. Naveau, and C. Cassou (2007), Inconsistency between atmospheric dynamics and temperatures during the exceptional 2006/2007 fall/winter and recent warming in europe, *Geophysical Research Letters*, *34*(L21808), doi:10.1029/2007GL031981.

Zhu, Y., and R. E. Newell (1998), A proposed algorithm for moisture fluxes from atmospheric rivers, *Monthly Weather Review*, *126*(3), 725 – 735, doi:http://dx.doi.org/10.1175/1520-0493(1998)126⟨0725:APAFMF⟩2.0.CO;2.